A NONLINEAR TRANSIENT APPROACH FOR MORTON SYNCHRONOUS ROTORDYNAMIC INSTABILITY AND CATCHER BEARING LIFE PREDICTIONS

A Dissertation

by

JUNG GU LEE

May 2012

Major Subject: Mechanical Engineering

A NONLINEAR TRANSIENT APPROACH FOR MORTON

SYNCHRONOUS ROTORDYNAMIC INSTABILITY AND

CATCHER BEARING LIFE PREDICTIONS

A Dissertation

by

JUNG GU LEE

Submitted to the Office of Graduate Studies of
Texas A&M University
in partial fulfillment of the requirements for the degree of

DOCTOR OF PHILOSOPHY

Approved by:

Chair of Committee,	Alan B Palazzolo
Committee Members,	Moo-Hyun Kim
	Steve Suh
	Won-jong Kim
Head of Department,	Jerald A. Caton

May 2012

Major Subject: Mechanical Engineering

ABSTRACT

A Nonlinear Transient Approach for Morton Synchronous Rotordynamic Instability and

Catcher Bearing Life Predictions. (May 2012)

Jung Gu Lee,

B.S.; M.S., Soongsil University, South Korea

Chair of Advisory Committee: Dr. Alan B. Palazzolo

This dissertation deals with three research topics; i) the catcher bearings life prediction method, ii) the Morton effect, and iii) the two dimensional modified Reynolds equation.

Firstly, catcher bearings (CB) are an essential component for rotating machine with active magnetic bearings (AMBs) suspensions. The CB's role is to protect the magnetic bearing and other close clearance component in the event of an AMB failure. The contact load, the Hertzian stress, and the sub/surface shear stress between rotor, races, and balls are calculated, using a nonlinear ball bearing model with thermal growth, during the rotor drop event. Fatigue life of the CB in terms of the number of drop occurrences prior to failure is calculated by applying the Rainflow Counting Algorithm to the sub/surface shear stress-time history. Numerical simulations including high fidelity bearing models and a Timoshenko beam finite element rotor model show that CB life is dramatically reduced when high-speed backward whirl occurs.

Secondly, the theoretical models and simulation results about the synchronous thermal instability phenomenon known as Morton Effect is presented in this dissertation.

A transient analysis of the rotor supported by tilting pad journal bearing is performed to obtain asymmetric temperature distribution of the journal by solving variable viscosity Reynolds equation, energy equation, heat conduction equation, and equations of motion for rotor. The tilting pad bearing is fully nonlinear model. In addition, thermal mode approach and staggered integration scheme are utilized in order to reduce computation time. The simulation results indicate that the temperature of the journal varies sinusoidally along the circumferential direction and linearly across the diameter, and the vibration envelope increased and decreased, which considers as a limit cycle that is stable oscillation of the envelope of the amplitude of synchronous vibration.

Thirdly, the Reynolds equation plays an important role to predict pressure distribution in the fluid film for the fluid film bearing analysis. One of the assumptions on the Reynolds equation is that the viscosity is independent of pressure. This assumption is still valid for most fluid film bearing applications, in which the maximum pressure is less than 1 GPa. In elastohydrodynamic lubrication (EHL) which the lubricant is subjected to extremely high pressure, however, the pressure independent viscosity assumption should be reconsidered. With considering pressure-dependent viscosity, the 2D modified Reynolds equation is derived in this study. The solutions of 2D modified Reynolds equation is compared with that of the classical Reynolds equation for the plain journal bearing and ball bearing cases. The pressure distribution obtained from modified equation is slightly higher pressures than the classical Reynolds equations.

DEDICATION

To my dear Mummy and Daddy

ACKNOWLEDGMENTS

I would like to appreciate Dr. Palazzolo for his immeasurable considerations and concerns during my graduate study in the Vibration Control Electromechanical Lab at Texas A&M University. I also would like to thank Dr. Steve Suh, Dr. Wong-jong Kim, and Dr. Moo-Hyun Kim for serving on my advisory committee. I am grateful to Dr.Jin-Oh Kim, Dr.Hoseon Yoo and Dr.Gunbok Lee for their assistances.

Thank also to many friends who shared office with me, and many Korean friends. I wish to thank my family members for their moral support.

TABLE OF CONTENTS

Page

LIST OF FIGURES

LIST OF TABLES

NOMENCLATURE

$[B_T]$ — Convection Conduction Matrix

$[C]$ — Damping Matrix

C_R — Rotor Damping Matrix

C_b — Bearing Clearance

C_p — Pad Clearance

C_s — Support Damping

c_p — Specific Heat

D — Cumulative Damage

d — Diameter

E — Young's Modulus

e_d — Unbalance Eccentric Distance due to Thermal Deflection

$\{F\}$ — External Force Vector

$\{F_T\}$ — Global Thermal Dissipation Force Vector

F_B — Nonlinear Bearing Force

F_n — Normal Contact Force

F_T — Contact Load due to Thermal Expansion

F_{ex} — External Force

F_{im} — Imbalance Force

F_x^t x-Component of Thermal Imbalance Force

F_y^t y-Component of Thermal Imbalance Force

F_t Tangential Force

f_1 Factor Depending on Bearing Geometry and Relative Bearing Load

$[G]$ Gyroscopic Matrix

G_R Gyroscopic matrix

H_r Power Loss

h Fluid Film Thickness

I The Second Moment of Area

I_p Polar Moments of Inertia

$[K]$ Stiffness Matrix

K_R Rotor Stiffness Matrix

K_c Contact Force Coefficient

K_s Support Stiffness

k Conduction Coefficient

k_H Hertzian Contact Stiffness

L_d Distance between Bearing Center and Overhung Mass

l_i Distance Inner Race under External Force

l_e Distance Inner Race under External Force

l_{oi} Distance between Ball Center and Inner Race

l_{oe} Distance between Ball Center and Outer Race

$[M]$ Mass Matrix

M_R Rotor Mass Matrix

m Mass

N Number of Cycles

n Number of Applied Cycles

P Pressure

$\{Q\}$ Contact Force Vector

Q_i Contact Force of Inner Race Using the Modified Hertzian Formula

Q_e Contact Force of Inner Race Using the Modified Hertzian Formula

Q_x x-Component of Flow Rate

Q_y y-Component of Flow Rate

q Flux

q_e Deflection due to Imbalance

q_t Deflection due to Thermal Bow

R_x x-Direction Curvature

R_y y-Direction Curvature

r Radius

$[T]$ Transformation Matrix

$\{T\}$	Temperature Vector
T	Temperature
T_l	Torque due to Thermal Load and External Force
T_0	Ambient Temperature
T_s	Shaft Temperature
t	Time
$\{u\}$	Displacement Vector of Inner Races
u_r	Displacement of Inner Race
$\{v\}$	Displacement Vector of a Ball Center
V_i	Velocity of Inner Race
V_r	Velocity of rotor
V_{rel}	Tangential Relative Velocity between Inner Race and rotor
w_r	Displacement of Outer Race
x, y	Cartesian Coordinates
z	Cross Film Direction

Greek

α	Contact Angle
β	Bow Angle
γ	Contact Angle between Rotor and CB

δ Tilt Angle

ε Thermal Expansion

ξ Thermal Expansion Coefficient

η, ζ Natural Coordinates

μ Viscosity

μ_d Kinetic Coefficient

μ_s Static Friction Coefficient

v Poisson's Ratio

ρ Density

σ_{max} Maximum Hertzian Contact Stress

τ_o Subsurface Shear Stress

τ_{eff} Equivalent Shear Stress

$\tau_{surface}$ Surface Shear Stress

ω Shaft Speed

CHAPTER I

INTRODUCTION

1.1 Overview

A variety of bearings such as conventional rolling element bearings, fluid film bearings, and magnetic bearings are used in rotating machinery to support the rotating element, provide damping and control the locations of critical speed. The conventional rolling element bearings have some advantages in terms of maintenance and cost compared with fluid film bearings and magnetic bearings. However, the damping of the conventional rolling bearings is very low which limits their ability to suppress resonance and maintain vibration stability. In contrast, fluid film bearings provide a relative higher damping and lower sound level. Due to cross coupled stiffness force, however, instability phenomenon may occur in plain journal bearing, lemon type bearing, fixed bearing applications. Tilt pad journal bearings, which belong to the fluid film bearing family, are used in rotating machinery to prevent instability since they provide nearly zero cross coupled stiffness as compared to other types of fluid film bearings. The rolling element bearings and fluid film bearings are required in some lubrication systems, however, the lubricant necessarily generates power loss. Using electromagnetic forces provides levitation of the shaft in high rotating speed without any use of lubrication systems or mechanical power loss. Nowadays active magnetic bearings

_____

This dissertation follows the style and format of the ASME Journal of Tribology.

(AMB) can be applied for various products such as (i) machine tools to be operated at high speed, (ii) vacuum applications and pumps, (iii) flywheel system, and (iv) turbo-machinery.

A rolling-element auxiliary or catcher bearing (CB) is necessary to protect MB stators and stationary components along shaft in the event of AMB failure or high transient loads. Under normal operation of MBs, the rotor maintains a positive clearance with CBs, which is less than a clearance with MBs. If the AMB failure occurs, the rotor touches down onto inner race of CBs, and the impact force increases bearing load while the friction force sharply accelerates the inner race speed generating heat loss at the mechanical contacts. The high impact force, internal loads and high temperature significantly reduce the fatigue life of CBs. A rotor drop model and nonlinear ball bearing model including thermal effect are developed in order to calculate the fatigue life of CBs in terms of the number of drop events, The Rainflow counting algorithm used in random load circumstance to predict fatigue life is applied to CB model. It is important to note that there has been no credible approach for predicting catcher bearing life until the present.

The rotordynamics literature has many papers on non-synchronous instability due to forces described by cross coupled dynamic coefficients. Recently another type of instability phenomenon was reported in rotor bearing systems with a large overhung mass. According to the limited references, this instability, which is known as the Morton effect, is due to an asymmetric temperature distribution around the circumference of the journal (length of shaft within the bearing). The Morton Effect occurs when the journal

is executing a synchronous orbit around its steady state equilibrium position (operating point). This orbit causes one portion of the journal surface to become a "hot spot", while a diametrically opposite section of the journal surface to become a "cold spot". This temperature difference leads to a temperature gradient developed across the journal. , Thermal bending will occur if the temperature gradient and the magnitude of the unbalance which already exists in the system are adequate. Under these conditions the bent shaft may cause an increase in imbalance and ensuing vibration, which may cause an increase in the lubricant temperature. The increased temperature gradient will then initiate more thermal bending. These actions describe a positive feedback mechanism which will drive the system unstable. In order to simulate the Morton Effect, a generalized Reynolds equation considering temperature-dependent viscosity, a 2-D energy equation, a heat conduction equation, and the mechanical equations of motion of the vibrating rotor are solved using the FEM. The solution of Reynolds provides pressures in the fluid film, and fluid velocities for inserting into the energy equation, which in turn provides the temperature and viscosity distribution throughout fluid film. Utilizing the temperature distribution in the fluid film, the temperature distribution of the journal is calculated and the bend angle and thermal imbalance induced by the thermal gradient of the journal are determined. The developed code for the Morton Effect provides the journal across-the-diameter temperature difference and orbit size versus time.

The basic equation for fluid motion in the fluid film bearing is known as the Reynolds equation. This equation was first derived in a remarkable paper by Reynolds.

The classical Reynolds equation is derived by combining the fluid dynamics momentum and continuity equations. The following assumptions are imposed:

a. Body, forces and fluid inertia are negligible

b. Pressure distribution through the thickness is constant

c. Curvatures of the two surfaces are large compared to the film thickness

d. Newtonian fluid

e. No slip boundary condition at the solid fluid interface

f. Flow is laminar.

g. Mass density is independent of pressure and temperature.

The assumption that the viscosity is constant is accurate only at low pressures. In elastohydrodynamic lubrication (EHL) cases which are subjected to extremely high pressures, this assumption no longer holds. It is necessary to modify Reynolds equation with considering pressure-dependent viscosity to predict more accurate fluid velocities, forces and pressures in the EHL fluid film.

1.2 Literature Review

1.2.1 Fatigue Life Prediction of an AMB Catcher Bearing

Active magnetic bearings (AMBs) are increasingly being used in industrial machines such as compressor, turbines, and generators since they cause only minor friction losses, are lubrication free, and can be operated adaptively to optimize

machinery reliability and performance. Although advanced control algorithms provide high AMB reliability, CBs are still needed for power failure and bearing overload events [1-3].

Some publications provide simulation results for rotordynamic system response following a drop event onto catcher bearings. Most researchers, like Ishii and Kirk [4], have modeled the CB as a linear spring, damper and have sought to optimize the CB performance based on that model. Fumagalli et al. [5] and Fumagalli [6] studied the effect of air gap, friction coefficient, and CB damping on the impact dynamics and also conducted rotor drop tests. Cole et al. [7] studied the effects of bearing width, and inner race speed on the rotordynamic response. Sun et al.[8, 9] proposed a nonlinear ball bearing model with thermal growth, providing a more accurate component model for the CB. Although not directly addressing catcher bearings, Taktak [10] et al. determined that the friction coefficient decreases as the sliding interface temperature increases and that the shear stress due to sliding also decreased. Although not directly addressing catcher bearings, Böhmer et al.[11] conducted experiments to determine the influence of heat generation in the contact zone and found that: i) heat generated in the contact zone increased contact pressure, the size of contact zone, and the amount of sliding , and ii) fatigue strength for rolling contact fatigue decreased as the temperature increases. Some standards, such as API[12] specify an acceptable minimum number of drop occurrences, yet there is very few publications that address life prediction of CB's, in terms of the number of drop occurrences before failure. API specifies that *"The auxiliary bearing system shall be designed to survive at least two de-levitations from maximum continuous*

speed to zero speed with the normal aerodynamic braking and nominal process induced thrust load." Sun[13] determines the fatigue life of ball bearing - catcher bearings, however a Lundberg-Palmgren formula is employed, which is strictly valid only for steady continuous loading, whereas a CB drop event is not steady and may involve erratic transient motion and forces. In comparison, the rainflow approach presented here is valid for random loading and includes effects of shear stress due to rub between the rotor and inner race, which is neglected in [13].

1.2.2 Accurate Prediction of the Morton Effect

A vibration induced hot spot in radial fluid film bearings can cause synchronous (same frequency as shaft spin frequency) continually increasing vibrations that result in a limit cycle. The phenomenon is known as the Morton effect. Theoretical investigations by Keogh and Morton[14] and experimental study[15] by deJongh and Morton indicate that rotors supported by fluid film bearings exhibit a nonuniform temperature distribution around the bearing journal circumference. This thermal effect results in rotor bending, which can, in combination with an overhung mass such as couplings and overhung impellers, significantly increase rotor unbalance and thus synchronous rotor vibration. Under certain conditions, it can lead to synchronous rotor instability. Many researchers have studied the Morton Effect since Keogh and Morton first found the mechanism of synchronous instability due to thermal gradient across the journal diameter. Gomiciaga and Keogh [16] theoretically calculated the thermal gradient of a journal in a plain journal bearing using CFD technique for a given forward or backward

whirl orbit. They found that the temperature difference across the journal diameter depends on the static eccentricity and orbit size, and that there is the phase lag between the high spot (outermost point on the journal surface) and the hot spot in a range of approximately 0 deg to 60 deg. Larsson[17-18] performed a stability analysis of the rotor system supported by tilting pad bearing with considering asymmetric heating in the journal in frequency domain by using Nyquist stability criterion of transfer function, which is related between asymmetric journal temperature and vibration responses. He calculated the temperature distribution of the journal using the published fluid film temperature distribution, whose assumptions were; i) infinite bearing width, ii) no cavitation in the fluid film, and iii) no heat transfer through pads or journal. Balbahadur and Kirk [19-20] proposed theoretical models for simulating the Morton Effect. Their approach is to simultaneously simulate the isoviscous Reynolds equation, a highly simplified energy equation, which includes heat transfer throughout the shaft and the bearing, and the rotordynamic (shaft) equations. Their use of a simpler model yields computation time that is relatively short. However, their approaches ignore the phase lag between the high spot and the hot spot, and assume that these spots are coincident. Their instability criterions based on instability threshold unbalance values that were obtained by comparing their simulation results with available experimental results, instead of using a frequency or time domain. Murphy and Lorenz's approach [21] assumes that the shaft surface temperatures equals the lubricant's mid-film temperature, and may be reliably calculated by treating the vibrating journal orbit as a sequence of steady state operating points, for the purpose of obtaining the fluid film temperature. Their approach

does not solve the transient energy and shaft heat conduction equations and assumes the hot spot and high spot are coincident and that the journal's cross diameter temperature difference is proportional to the orbit size. Reference [16] indicates that linear relationship between temperature difference and orbit size may not be a very accurate assumption. The relationship between orbit size and temperature difference is in general nonlinear.

1.2.3 A 2D Reynolds Equation Including Pressure-Dependent Viscosity

The basic equation of fluid-film lubrication, the Reynolds equation, can be derived from the reduced form of the Navier-Stokes and continuity equations. This equation was first derived in a remarkable paper by Reynolds [22]. The Reynolds equations assumptions include: i) the fluid is a Newtonian fluid, ii) the inertia and body force terms are negligible compared with the pressure and viscous terms, iii) there is a negligible variation of pressure across the fluid, and iv) the viscosity is constant. However, numerous experimental results showed that viscosity depends on the temperature and pressure[23-29]. Barus[30] proposed the isothermal-viscosity-pressure dependence of lubricant by introducing pressure-viscosity coefficient which depends only on temperature, but not on pressure. Barus' formula is extensively used, it is not generally applicable and is valid as a reasonable approximation only in a moderate-pressure range. Roelands[31] proposed a general temperature-pressure-dependent viscosity equation. However, it is valid for moderate temperature range. Even though it is assumed that viscosity does not depends on the temperature and pressure, the solution of Reynolds

equation provides a pretty accurate pressure distribution. In elastohydrodynamic lubrication, EHL, in which the fluid film is subjected to extremely high pressure, the assumption that the viscosity is independent of the pressure no longer holds. Pressure dependence of viscosity is very significant and the viscosity can increase by several orders of magnitude due to pressure increase. Rajagopal and Szeri[32] derived a 1-D pressure-dependent Reynolds equation and compared its solutions with that of classical Reynolds equation. The 1D modified Reynolds equation results in slightly higher pressures, but at significantly higher viscosities, than the classical Reynolds equations.

1.3 Contributions

This presented research contains the following unique contributions;

(1) A stress based methodology to predict the number of catcher bearing drop occurrences to failure

(2) A computationally efficient, transient, numerical integration based approach for determining synchronous limit cycles that results from synchronous whirl induced asymmetric heating, a.k.a. the Morton effect.

(3) Algorithm for 2D Reynold's equation solution of pressures in a journal bearing, including effects of pressure-dependent viscosity.

CHAPTER II

CATCHER BEARING LIFE PREDICTION USING A RAINFLOW

COUNTING APPROACH

2.1 Overview

The conventional bearing life prediction method based on the LP formula is not valid for random load case such as rotor drop cases. To accurately predict fatigue life of the CB, a rainflow counting approach is applied in this chapter.

In the section 2.2, thermal growth during rotor drop event is considered using heat transfer network, and nonlinear ball bearing model is utilized to calculate the Hertzian contact force and stress for an each ball. In addition, Timoshenko beam model is used for FE rotor model, and rotor drop model is presented in this chapter.

Fatigue damage models are described in the section 2.3. The mathematical models for sub/surface shear stress and load and shear stress distribution are introduced. The fatigue life prediction method is developed based on Miner's rule, Rainflow counting method, and S-N curve for AISI 51200, which is the most commonly used in the rolling bearing elements.

Using the developed model, a variety of numerical simulation are conducted to investigate the effects of CB fatigue life such as support effect, friction coefficient, air gap between rotor and inner race, initial rotor drop speed, and side loads from the MBs . The simulation results are listed in the section 2.4.

2.2 Simulation Models

2.2.1 Thermal Ball Bearing Model

The rolling element bearing has a variety of heat sources, however, two major ones are considered during the rotor drop event: the rotor/inner race friction due to mechanical rub and the bearing drag torque. Power loss due to mechanical rub between rotor and inner race is expressed as

$$H_r = F_t \cdot V_{rel} \tag{2.1}$$

where F_t is tangential force action and V_{rel} is the tangential relative velocity between the inner race and the rotor at the contact interface. The bearing drag torque which depends on bearing type, external load, lubricant and operating speed is calculated by an empirical formula [33]. A bearing thermal model is developed assuming a uniform, radial direction heat flux, similar to Jorgensen and Shin [34]. Figure 2.1 shows the thermal nodes in the bearing components and equivalent heat transfer network. Thermal resistances corresponding for each component are defined in Table 2.1 [8].

The power conservation equation has the following form at each temperature node:

$$mC_p \frac{dT}{dt} = q_i - q_o \tag{2.2}$$

where the parameter m is a lumped thermal mass, C_p is the specific heat, and q_i and q_o are the heat flux in and out of the system. The thermal system temperatures are calculated, then the free thermal expansions of the outer race, inner race and ball are obtained from:

$$\text{outer race: } \varepsilon_e = \frac{\xi_e}{3}\frac{(1+\nu_e)r_e}{r_e+r_h}\left[\Delta T_{Le}(2r_e+r_h)+\Delta T_h(2r_h+r_e)\right] \tag{2.3}$$

$$\text{inner race: } \varepsilon_i = \frac{\xi_i}{3}(1+\nu_i)r_i\left[\Delta T_s+\Delta T_{Li}\right] \tag{2.4}$$

$$\text{ball: } \varepsilon_b = \xi_b r_b \Delta T_b \tag{2.5}$$

where ξ, ν, and r are the thermal expansion coefficient, the Poisson's ratio, and radius of the respective bearing components, respectively. Subscript *b, e, h, i,* and *s* represent ball, outer race, housing, inner race, and shaft, respectively. The contact load due to thermal expansion is expressed by

$$F_T = k_H \varepsilon^{1.5} \tag{2.6}$$

where k is the Hertzian contact stiffness, $\varepsilon = \varepsilon_b + (\varepsilon_i - \varepsilon_e)\cos\alpha$, and α is the contact angle between the ball and the inner race. A modified Palmgren formula including the effect of the thermal load is given by [35] as

$$T_l = f_1(F_{ex}+F_t)d_m \tag{2.7}$$

where f_1 is a factor depending upon bearing geometry and relative bearing load, F_{ex} is the external force acting on the bearing, and d_m is the mean of the inner and outer diameters.

2.2.2 Nonlinear Ball Bearing Model

The nonlinear ball bearing model excludes tilt deflections and is similar to that in [8]. Bearing components deflect in the x, y, and z direction shown in Figure 2.2 in response to the external force $\{F\}$. The r-z plane passes through the center of a ball at an angle φ referenced to the x axis. The inner race cross section at a ball location is loaded by the contact force vector $\{Q\}$ at the groove center p, which has a displacement vector $\{u\}$, where $\{Q\}^T = \{Q_r \ Q_z\}$ and $\{u\}^T = \{u_r \ u_z\}$. The vectors for different reference points are related by a transformation matrix $[T]$:

$$\{u\} = [T]\{X\}, \{Q\} = [T]\{f\} \tag{2.8}$$

where

$$T = \begin{bmatrix} \cos\phi & \sin\phi & 0 \\ 0 & 0 & 1 \end{bmatrix} \quad \{x\}^T = [x\,y\,z] \tag{2.9}$$

and the vector $\{f\}$ represents an equivalent force vector at the reference coordinate. The dynamic equations of motion for the inner race are given by

$$m_i\{\ddot{X}\} = \{F\} + \sum_{j=1}^{n} T_j^T \{Q\}_j \tag{2.10}$$

where n is the number of balls and m_i is the mass of inner race. The contact force vector $\{Q\}$ contributed by a ball is expressed as

$$\{Q\} = \begin{Bmatrix} Q_r \\ Q_z \end{Bmatrix} = \begin{Bmatrix} -Q_i\cos\alpha_i \\ -Q_i\sin\alpha_i \end{Bmatrix} \tag{2.11}$$

where Q_i is a contact force component and α is the contact angle between a ball and the inner race. Let the vector $\{v\}$ be the displacement of a ball center. Then the equations of
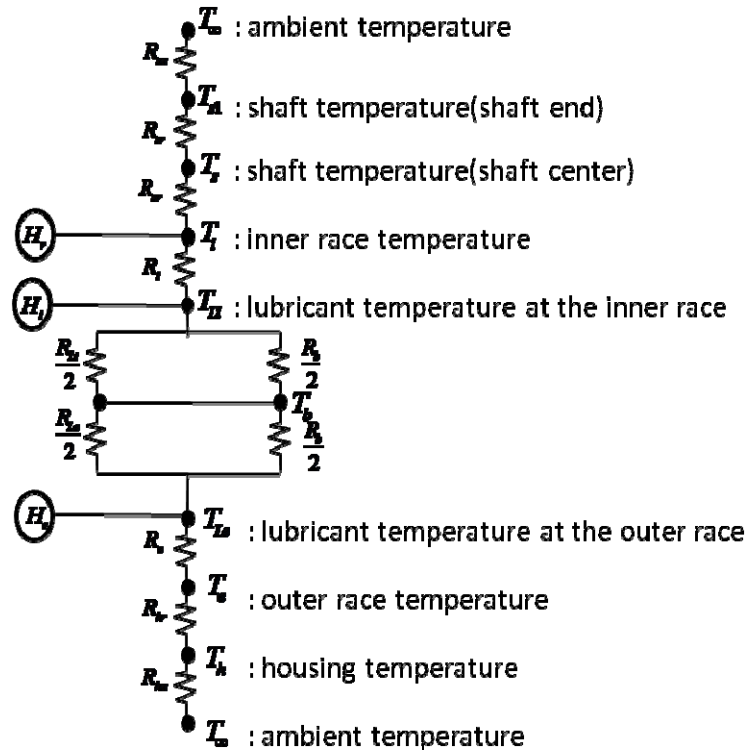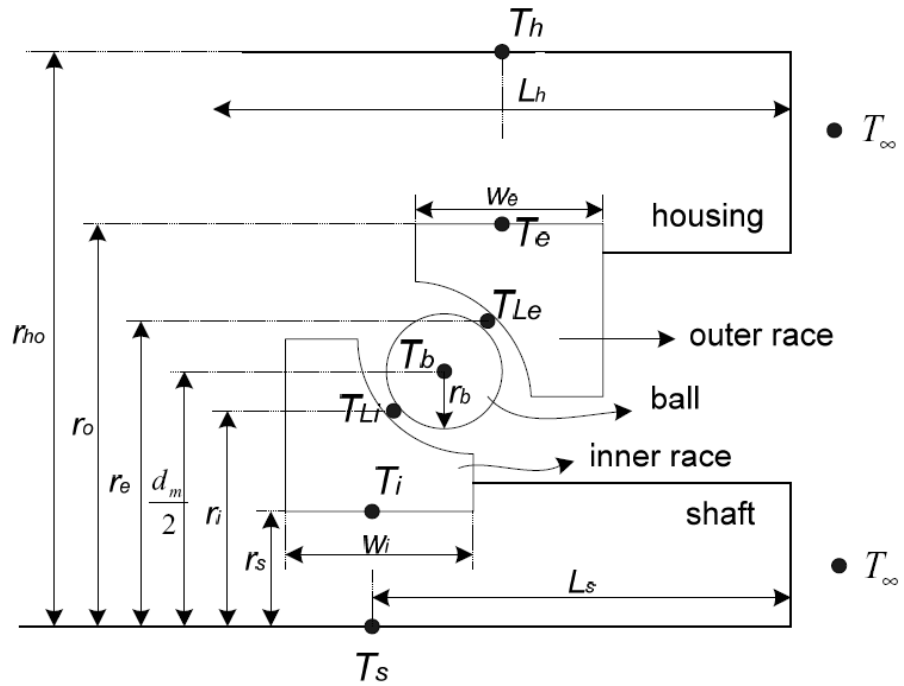
Fig. 2.1 Thermal Node and Heat Transfer Network

Table 2.1 Thermal Resistance [8]

Ball/Lubricant	Inner Race/Shaft
$R_{Li} = \dfrac{r_b}{k_l(2\pi r_i W_i - \pi n r_b^2)}$	$R_i = \dfrac{\ln(r_i / r_s)}{2\pi k_i W_i}$
$R_{Le} = \dfrac{r_b}{k_l(2\pi r_e W_e - \pi n r_b^2)}$	$R_{sr} = \dfrac{1}{\pi k_s W_i}$
$R_b = \dfrac{1}{n\pi k_b}$	$R_{sa} = \dfrac{L_s}{\pi k_s r_s^2} + \dfrac{1}{\pi h_s r_s^2}$
Housing	**Outer Race**
$R_{hr} = \dfrac{\ln(r_h / r_o)}{2\pi k_h L_h} + \dfrac{1}{2\pi r_h h_h L_h}$	
$R_{ha} = \dfrac{L_h}{2\pi k_h (r_h^2 - r_o^2)} + \dfrac{1}{\pi h_h (r_h^2 - r_o^2)}$	$R_e = \dfrac{\ln(r_o / r_e)}{2\pi k_e W_e}$

(a)   (b)
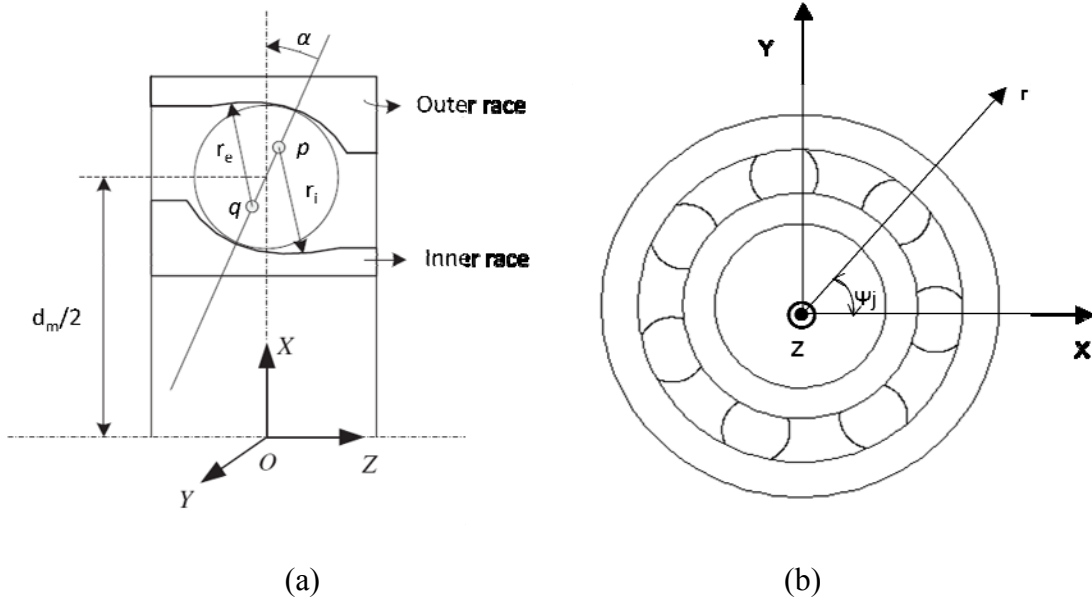
Fig. 2.2 Bearing Geometry

motion for an individual ball including centrifugal force F_c becomes

$$m_b \begin{bmatrix} \ddot{v}_r \\ \ddot{v}_z \end{bmatrix} = \begin{bmatrix} Q_i \cos \alpha_i - Q_e \cos \alpha_e + F_c \\ Q_i \sin \alpha_i - Q_e \sin \alpha_e \end{bmatrix} \qquad (2.12)$$

where the subscripts i, e represents the inner and outer races, respectively and m_b is the mass of a ball. The outer race is inserted into the bearing housing which is supported by stiffness K_s and damping C_s and is constrained along the axial direction as shown in Figure 2.3. The equations of motion for the combined outer race and housing become

$$(m_e + m_h) \begin{bmatrix} \ddot{x}_e \\ \ddot{y}_e \end{bmatrix} = \begin{bmatrix} \sum_{j=1}^{n} [Q_e \cos \alpha_e]_j \cos \phi_j \\ \sum_{j=1}^{n} [Q_e \cos \alpha_e]_j \sin \phi_j \end{bmatrix} - C_s \begin{bmatrix} \dot{x}_e \\ \dot{y}_e \end{bmatrix} - K_s \begin{bmatrix} x_e \\ y_e \end{bmatrix} \qquad (2.13)$$

where m_e and m_h are the masses of the outer race and the housing, and x_e and y_e are the displacements of housing. Let w_r and u_r be the displacements of the outer and inner race groove centers (q and p respectively) in the radial direction, and then the displacements of the inner race groove center p and the ball center are geometrically related as shown in Figure 2.4. The lengths l_{oi}, l_{oe} represent the distance between the ball center and the groove centers under no external force, and the lengths l_i, l_e the distances under external forces. Using the geometric relation between the displacements of the groove centers and ball center, the following equations are obtained:

$$\tan \alpha_i = \frac{l_{oi} \sin \alpha_o + u_z - v_z}{l_{oi} \cos \alpha_o + u_r + \varepsilon_i - v_r} \qquad (2.14)$$

$$\tan \alpha_e = \frac{l_{oe} \sin \alpha_o + v_z}{l_{oe} \cos \alpha_o + v_r - \varepsilon_e - w_r} \qquad (2.15)$$

$$l_i = \varepsilon_b + \sqrt{(l_{oi}\cos\alpha_o + u_r + \varepsilon_i - v_r)^2 + (l_{oi}\sin\alpha_o + u_z - v_z)^2} \qquad (2.16)$$

$$l_e = \varepsilon_b + \sqrt{(l_{oe}\sin\alpha_o + v_r - \varepsilon_e - w_r)^2 + (l_{oe}\sin\alpha_o + v_z)^2} \qquad (2.17)$$

where the ε terms indicate the thermal expansions as defined in Eqs. (2.3)-(5). The relative deflections δ at the contacts are then

$$\delta_i = l_i - l_{oi} \qquad (2.18)$$

$$\delta_e = l_e - l_{oe} \qquad (2.19)$$
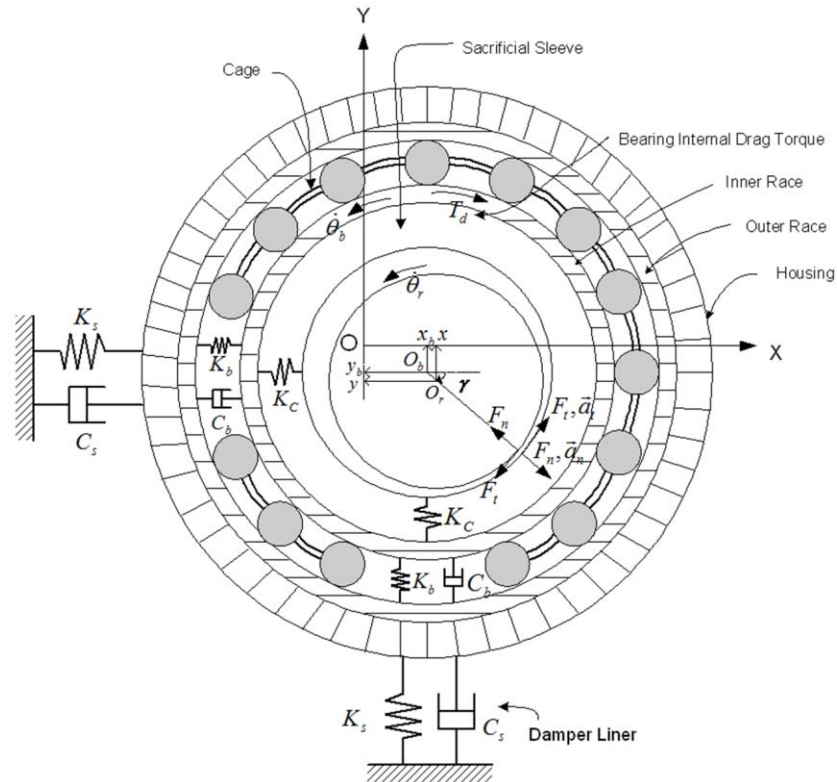
Fig. 2.3 Shaft and Catcher Bearing Model

The point contact forces are obtained from the modified Hertzian formula [8]

$$Q_i = k_i \delta_i^{3/2} (\frac{3}{2} \beta \dot{\delta}_i + 1) \qquad (2.20)$$

$$Q_e = k_e \delta_e^{3/2} (\frac{3}{2} \beta \dot{\delta}_e + 1) \qquad (2.21)$$

where β is linearly related to the coefficient of restitution of materials engaged in contact and ranges from 0.08 to 0.32 s/m for steel bronze[8]. The corresponding Hertzian point contact stress on the surface and at the center of the elliptical contact area is

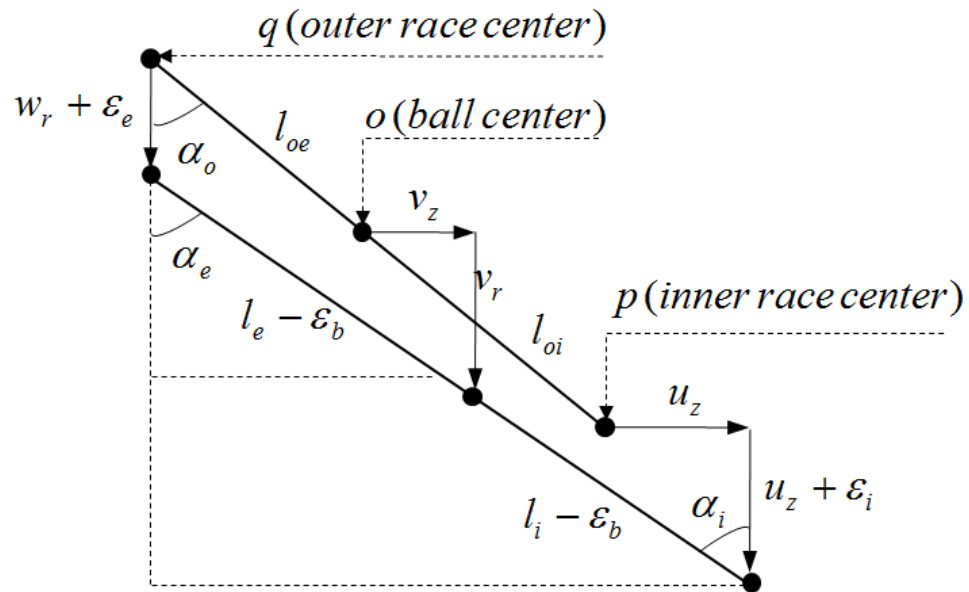$$\sigma_{max} = -\frac{3Q_{i,e}}{2\pi a_{i,e} b_{i,e}} \qquad (2.22)$$

Fig. 2.4 Displacements of the Ball, Inner Race, and Outer race

2.2.3 Flexible Rotor Model

The flexible rotor is modeled with Timoshenko beam elements including shear deformation. The equation of motion for a flexible rotor bearing system can be written as:

$$[M]\ddot{q} + [C + \Omega G]\dot{q} + [K]q = [F] \tag{2.23}$$

where M is the mass matrix, C is the damping matrix, G is the gyroscopic matrix, and K is the shaft stiffness matrix [36]. The vector q contains the nodal degrees of freedom, F is the load vector including the imbalance force and the nonlinear catcher bearing forces, and Ω is the angular velocity of the rotor. Each beam node has four degrees of freedom, two translations and two rotations. Equation (2.23) is written in modal coordinates as:

$$\Phi^T[M]\Phi\,\ddot{p} + \Phi^T[C + \Omega G]\Phi\,\dot{p} + \Phi^T[K]\Phi\,p = \Phi^T[F] \tag{2.24}$$

where Φ is the modal matrix of the undamped, normal modes for the rotor and p is a vector of modal coordinates.

2.2.4 Rotor Drop Simulation Model

Figure 2.3 shows the rotor drop and deep groove ball bearing, catcher bearing model. The frame of reference $O(X,Y)$ is fixed to the stationary machinery frame. The geometric centers of the rotor and bearing inner race are O_r and O_b, respectively. (x_r, y_r) is the location of O_r and (x_b, y_b) is the location of O_b in the fixed frame of reference. The contact angle between the rotor and CB is

$$\gamma = \tan^{-1}\left(\frac{y_r - y_b}{x_r - x_b}\right) \tag{2.25}$$

The contact force coefficient K_c which depends on the material property and geometry of the rotor and inner race is a factor in the nonlinear modified Hertzian contact force between the rotor and inner race. Palmgren[37] introduced the contact force coefficient for line contact

$$K_c = \left[\frac{0.39^{10/9}}{l} \left(\frac{4(1 - v_1^2)}{E_1} + \frac{4(1 - v_2^2)}{E_2} \right) \right]^{-1}$$

(2.26)

The normal force at the contact point between the spinning rotor and inner race is:

$$F_n = \begin{cases} K_c \delta^n \left(1 + \frac{3}{2} \beta \dot{\delta} \right) & e_r > c_r \\ 0 & e_r \leq c_r \end{cases}$$

(2.27)

where n is 10/9 for line contact and e_r is the distance between the rotor and inner race and is defined as follow

$$e_r = \sqrt{(x_r - x_i)^2 + (y_r - y_i)^2}$$

(2.28)

For sliding contact between the rotor and inner race, the friction force (tangential force) is calculated by multiplying the friction coefficient by the normal force.

$$F_t = \mu_d F_n$$

(2.29)

where μ_d is the kinetic coefficient of friction. The tangential velocities of the inner race and rotor at the contact point are calculated in order to identify rolling and sliding conditions

$$V_r = \dot{\theta}_r R_r - \dot{X}_r \sin\gamma - \dot{Y}_r \cos\gamma$$

(2.30)

$$V_i = \dot{\theta}_i R_i - \dot{X}_i \sin\gamma + \dot{Y}_i \cos\gamma$$

(2.31)

A rolling condition is applied when the tangential velocity of the rotor is the same as that of inner race. This means that there is no slip at the contact point, and the friction force F_t is a static frictional force, which satisfies

$$|F_t| \le \mu_s F_n \tag{2.32}$$

where μ_s is the static friction coefficient. The sign of the slip force is determined by the sign of the relative velocity, i.e.

$$F_t = sign\ (V_r - V_i)\ \mu_d\ F_n \tag{2.33}$$

The tangential friction forces for a rolling contact condition are obtained from the rotor and inner race, angular equilibrium equations by solving the following equations for the F_t

$$I_p \ddot{\theta}_r = -(F_{t1} + F_{t2}) \cdot R_r \tag{2.34}$$

$$I_{pb1} \ddot{\theta}_{i1} = F_{t1} R_{b1} - T_{d1} \tag{2.35}$$

$$I_{pb2} \ddot{\theta}_{i2} = F_{t2} R_{b2} - T_{d2} \tag{2.36}$$

where I_p, I_{pb} are the polar moments of inertia of the rotor and inner race, respectively. The subscripts 1 and 2 indicate catcher bearings 1 and 2.

2.3 Fatigue Damage

2.3.1 Shear Stress Acting on the Catcher Bearing

The failure of rolling bearings in surface fatigue caused by the concentrated contact force applied perpendicular to the surface, initiates at a location below the stressed surface. To determine the magnitude of the subsurface shear stress, Palmgren and Lundberg showed that the amplitude of the subsurface shear stress is related to the Hertzian stress and ellipse ratio. The detailed derivation is explained in Ref.[33]. The subsurface shear stress τ_0 is calculated from

$$\frac{2\tau_o}{\sigma_{max}} = \frac{\sqrt{(2t-1)}}{t(t+1)} \tag{2.37}$$

where t is an auxiliary parameter determined by elliptic contact region as shown Figure 2.5, and σ_{max} is defined in (2.22).

$$\frac{b}{a} = \sqrt{(t^2-1)(2t-1)} \tag{2.38}$$

The semimajor a and semiminor b axes of the projected elliptical area are calculated by Hertzian contact theory [33].

Harris [33] shows that the surface shear stress is very small compared with the normal stress in most rolling bearing applications, however, surface shear stress is very important for predicting fatigue life of a rolling element bearing. The surface shear stress is given by [33] as
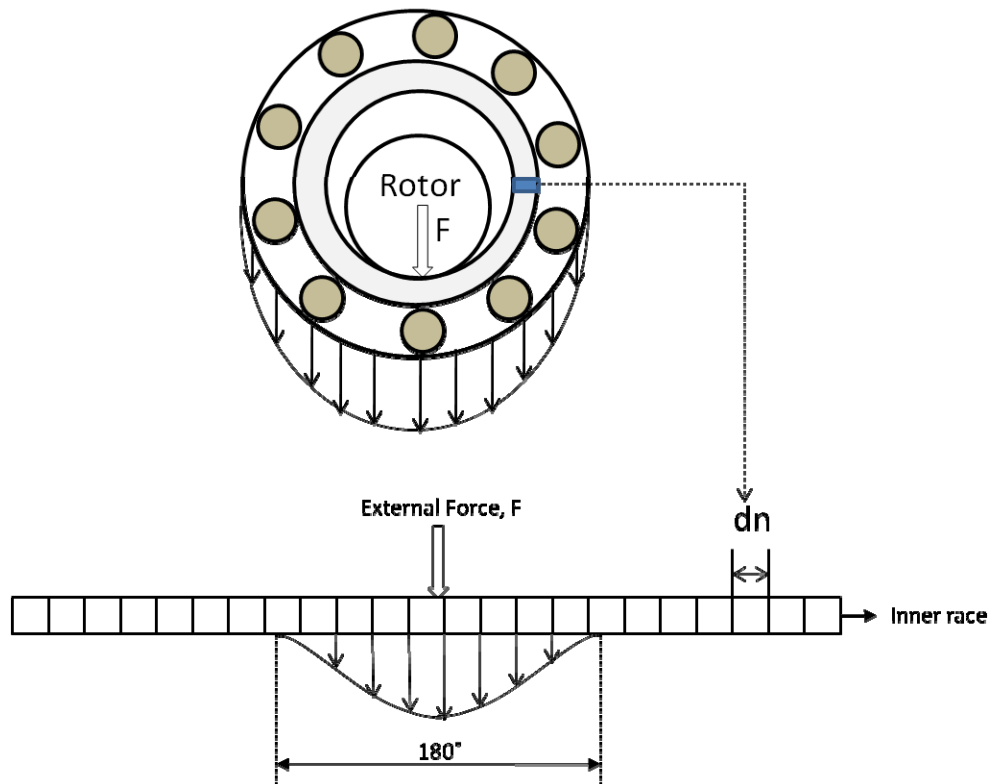
$$\tau_{surface} = \mu\sigma \tag{2.39}$$

where μ is the friction coefficient between ball and races and σ is the normal stress. The

friction coefficient is typically from 0 to 0.3. In this paper, the friction coefficient
between the ball and races is set equal to 0.2 [33].
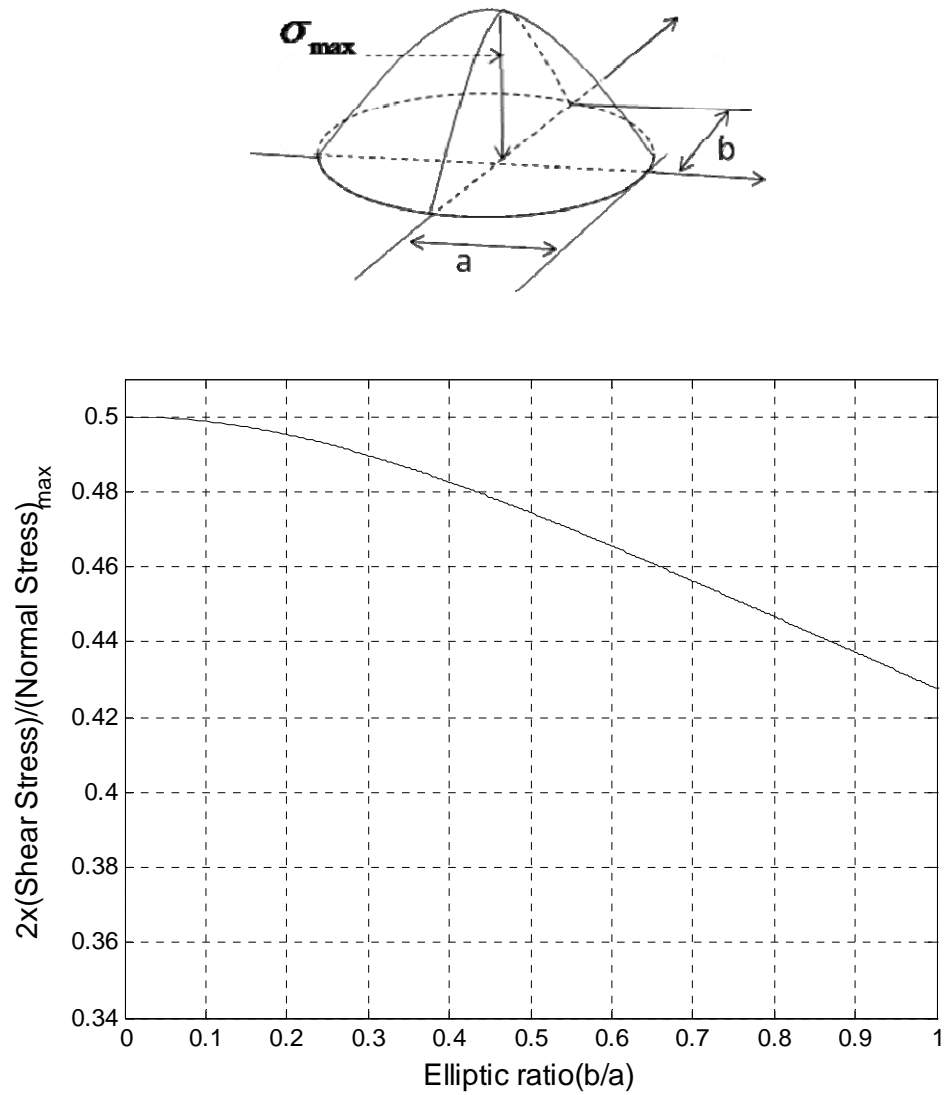
Fig. 2.5 Sub-surface Shear Stress Ratio τ_0 / σ_{max} vs. Ellipse Axis Ratio [33]

Fig. 2.6 Load Distribution in the Inner Race

2.3.2 Load and Stress Distribution in the Races

The load distribution along the inner race varies with contact point between the rotor and inner race as illustrated in Figure 2.6. For the case that the radial rotor contact external force acts on the inner race of the bearing, an equivalent load distribution is expressed by

$$F(\theta) = k(\theta) \ F_{ex} \tag{2.40}$$

where $k(\theta)$ is the load distribution factor defined by [38]

$$k(\theta) = \frac{\left(1 - \left(1 + 0.5\frac{e}{\delta_0}\right)(1 - \cos\theta)\right)^{3/2}}{\frac{z}{2\pi}\int_{-\theta}^{\theta}\left(1 - \left(1 + 0.5\frac{e}{\delta_0}\right)(1 - \cos\theta^*)\right)^{3/2}\cos\theta^*d\theta^*} \qquad (2.41)$$

where z, and e are the number of balls and internal radial clearance of the bearing. The term δ_0 is the relative displacement of the ball and race centers due to σ_{max} as defined by Eq. (2.22). The load distribution factor is affected by the relative internal radial clearance e/δ_0, however, the internal radial clearance is set to zero, which is a good approximation when the bearing is subjected to a radial load. Under the assumption that *e=0* the equivalent radial load is distributed from –pi/2 to pi/2, referenced to the contact point as shown in Figure 2.6. The sub-surface and surface shear stress are calculated at any point along the race utilizing the equivalent radial load distribution and Eq. (2.37) and Eq. (2.39).

2.3.3 Rainflow Cycle Counting Method

Parts of the CB are subjected to time varying stresses during the rotor drop occurrences. The Rainflow Cycle Counting Method [39], which was proposed by Dowling and Socie in 1982, is employed to predict the fatigue life of the CB which results from these stresses. The Rainflow method is used to identify stress cycles, that is, the stress range and mean stress for each cycle. Appendix A shows the procedure for the cycle counting method. Cumulative damage *D* and number of cycles *N* to failure are

determined using a histogram of cycle ranges and Miner's rule. Miner's rule is expressed

as follows. Failure is expected to occur if

$$D = \frac{n_1}{N_1} + \frac{n_2}{N_2} + \frac{n_3}{N_3} + ... = \sum_i \frac{n_i}{N_i} \geq 1 \qquad (2.42)$$

where n_i is the number of applied cycles and N_i is the number of cycles to failure at a

certain stress amplitude τ_i, respectively. In this study, the critical cumulative damage

value of D is chosen to be 1 in Eq.(2.42) and the fatigue life is expressed as;

$$Life = \frac{1}{\sum_i n_i / N_i} \qquad (2.43)$$

2.3.4 The S-N Curve

N.Raje and F.Sadeghi[40] showed that rolling fatigue is similar to torsional fatigue

by applying the S-N curve for torsional fatigue to calculate bearing fatigue life. The S-N

curve including thermal effects shown in Figure 2.7 is represented by

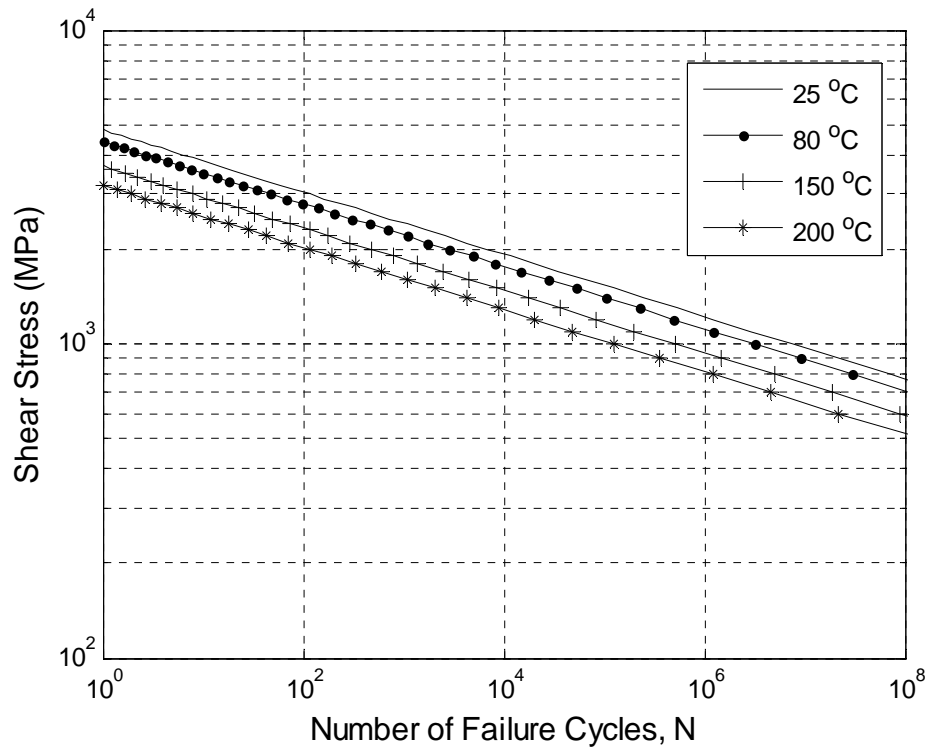$$N_f = \left(\frac{2a}{\tau_{eff}} \right)^B \qquad (2.44)$$

where

$$2a = -\hat{C}_1 T + \hat{C}_2 \qquad (2.45)$$

$$\tau_{eff} = \tau_{friction} + \tau_{normal} \qquad (2.46)$$

and $\hat{C}_1$, $\hat{C}_2$ are constants and B is positive and is the slope of the torsional S-N curve.

These parameters are listed in Table 2.2 for bearing steel AISI-52100. From reference

[33], τ_{normal} and $\tau_{friction}$ correspond with τ_o in Eq. (2.37) and $\tau_{surface}$ in Eq. (2.39).

Fig. 2.7 The S-N Curve [40]

**Table 2.2 S-N Curve Parameters for AISI-52100**

B	10.10			
$\hat{C}_1 \ (GPa/°C)$	0.01			
$\hat{C}_2 (GPa)$	5.20			
Temperature (^oC)	25	80	150	200
$a \ (GPa)$	2.47	2.20	1.84	1.60

Table 2.3 Example Rotor and Bearing data

Rotor		Bearing	
Mass of the Rotor	97.3 kg	Bore Diameter	80.0 *mm*
Polar Moment of Inertia	0.39 *kg m²*	Outer Diameter	125.0 *mm*
Transverse Moment of Inertia	2.82 *kg m²*	Bearing Width	22.0 *mm*
Air Gap	300 μm	Pitch Diameter	110.0 *mm*
Inner Diameter of Sleeve	60.6 *mm*	Ball Diameter	19.05 *mm*
		Number of Balls	10
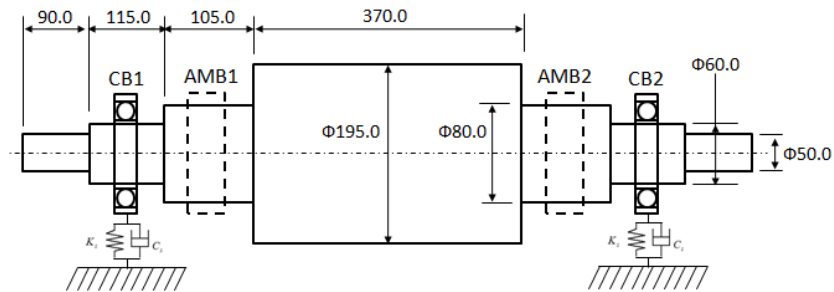
(a)
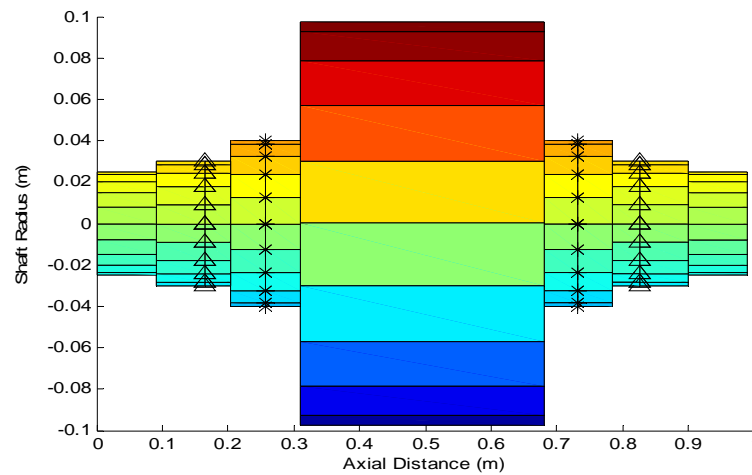
(b)

Fig. 2.8 Rotor Model; (a) Dimensions Diagram (in mm) and (b) Finite Element Model for Example System [41]

2.4 Simulation Results and Discussion

The example system consists of two CBs, and a horizontal rotor, which is depicted along with its FEM model in Figure 2.8. The FEM rotor has 11 elements. The rotor and bearing specifications are listed in Table 2.3. The model also includes flexible damped supports for the catcher bearings, which is typical for industrial applications. The stiffness and damping of these supports are 50,000,000 *N/m* and 5000 *Ns/m*, respectively. Transient responses are obtained by utilizing Newmark Beta based numerical integration, with a time step of 1e-4s. The following parameters are varied to investigate their effect on fatigue life: (a) bearing support stiffness and damping, (b) friction coefficient, (c) side load due to an applied magnetic bearing, (d) air gap, and (e) rotor speed. The simulation cases are summarized in the Table 2.4. The duration of the numerical integration is determined by how long reverse whirl is sustained, and a 1 second duration is adequate for a reverse whirl free drop event.

The contact point locations and load levels between the rotor, races, and balls randomly change after the rotor drop. Therefore the fatigue life varies around the circumferences of the races. Although there exists an infinite number of possible contact points along the race the model evaluates life at a finite number of points. A total of n equally spaced "test" points are located along the circumference of the inner race as shown in Figure 2.6. Note that the stresses and damage at any test point may be affected by a rotor/race contact force at some other location due to the effective load effect as illustrated in Figure 2.6 and described in Eqs (2.39)-(40). The life is evaluated at each of the test points utilizing the rainflow counting method and Miner's rule.

A study was conducted to determine an appropriate number of test points. For this case the rotor speed=20,000 rpm, $\mu_s = 0.3$, $\mu_d = 0.3$ air gap=0.3 mm and there is no side load. This case is included solely to illustrate the general response features and not for life evaluation, so its simulation duration is only 1 second. Figure 2.9 shows an orbit plot and shear stress distribution with the number of test points n=100. The red solid circle indicates the unloaded clearance circle. The shear stress time history at a test point and shear stress distribution at an instant in time are shown in the Figure 2.9 (c) and (d), respectively. The number of cycles at each stress level, and each test point, are counted using the Rainflow counting algorithm. The fatigue life at each test point is then calculated from Eq. (2.43). The fatigue life is selected as that of the test point that has the maximum damage. The simulation results indicates that the damage and the fatigue life vary between test points, and the bearing life approaches a constant value as the number of test point increases as shown in Figure 2.10. All of the following results were obtained utilizing 100 test points. Backward whirl motion occurs during rotor drop, induces high contact forces between the rotor and inner race, and may causes significant damage to the catcher bearing until the backward whirl motion diminishes. For the nominal case, the backward whirl motion diminishes after about 12s. Figure 2.10 (c) indicates that the number of drop occurrence to failure sharply reduces while backward whirl motion is occurring.

Table 2.4 Simulation Cases

|	Nominal Case	Case # 1	Case #2	Case #3	Case #4	Case #5	Case #6
Support Stiffness (N/m)	5e7	10e7	5e7	5e7	5e7	5e7	5e7
Support Damping (N·s/m)	5,000	5,000	10,000	5,000	5,000	5,000	5,000
Sliding Friction Coefficient	0.3	0.3	0.3	0.1	0.3	0.3	0.3
Kinetic Friction Coefficient	0.4	0.4	0.4	0.2	0.4	0.4	0.4
Air Gap (mm)	0.3	0.3	0.3	0.3	0.5	0.3	0.3
Side Load (N)	0	0	0	0	0	500	0
Rotor Speed (rpm)	20,000	20,000	20,000	20,000	20,000	20,000	10,000
Initial Temperature (^{o}C)	30						
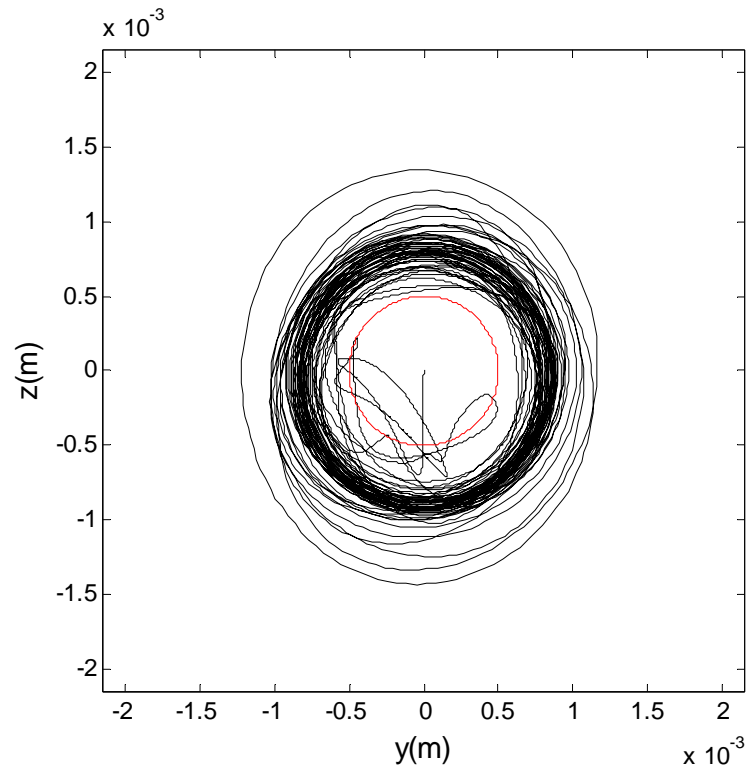
(a)
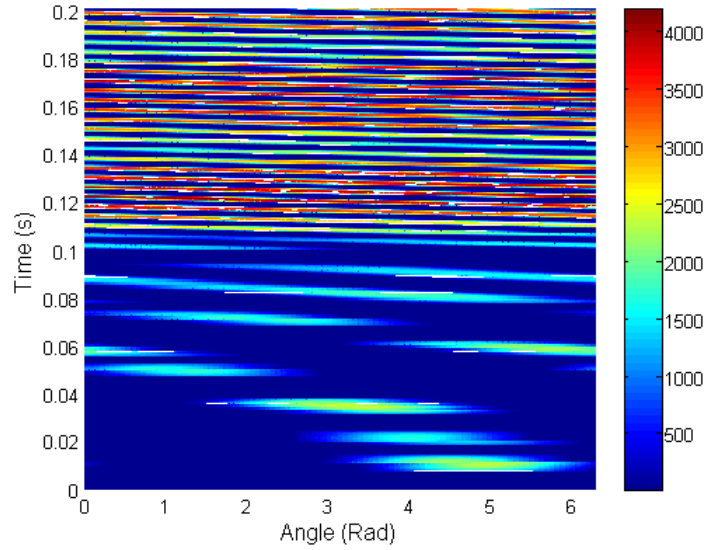
(b)

Fig. 2.9 Simulation Results of Nominal Case; (a) Orbit Plot,

(b) Shear Stress Distribution, (c) Shear Stress vs Time,

(d) Shear Stress vs Angle (e) Temperature vs Time, and (f) Rainflow Histogram
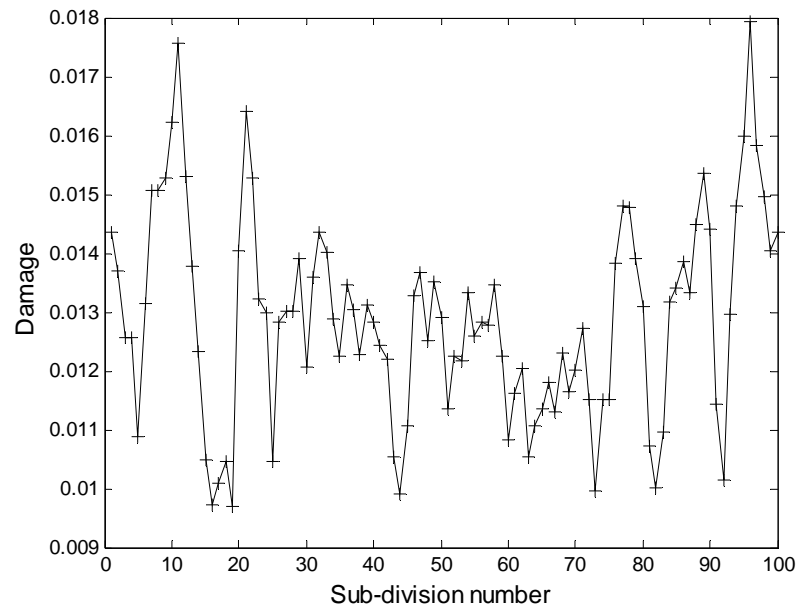
(c)

(d)
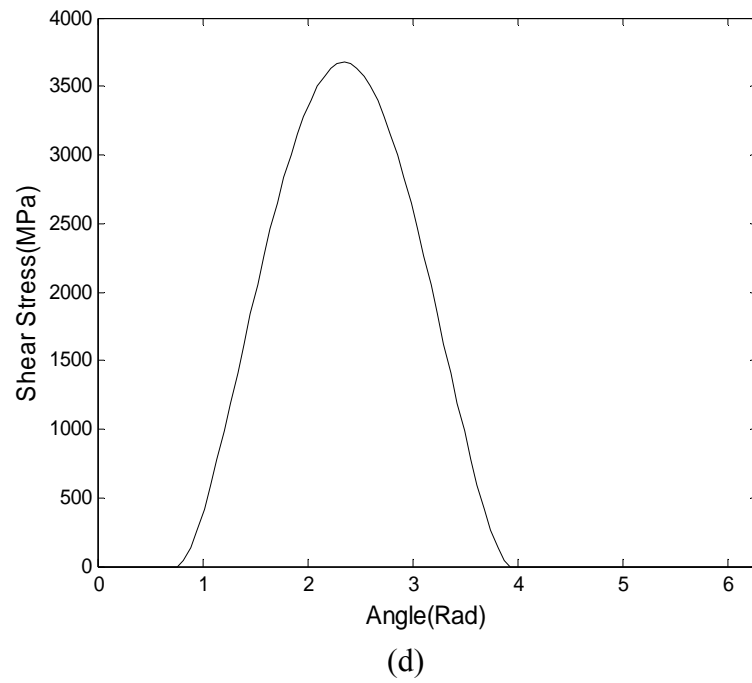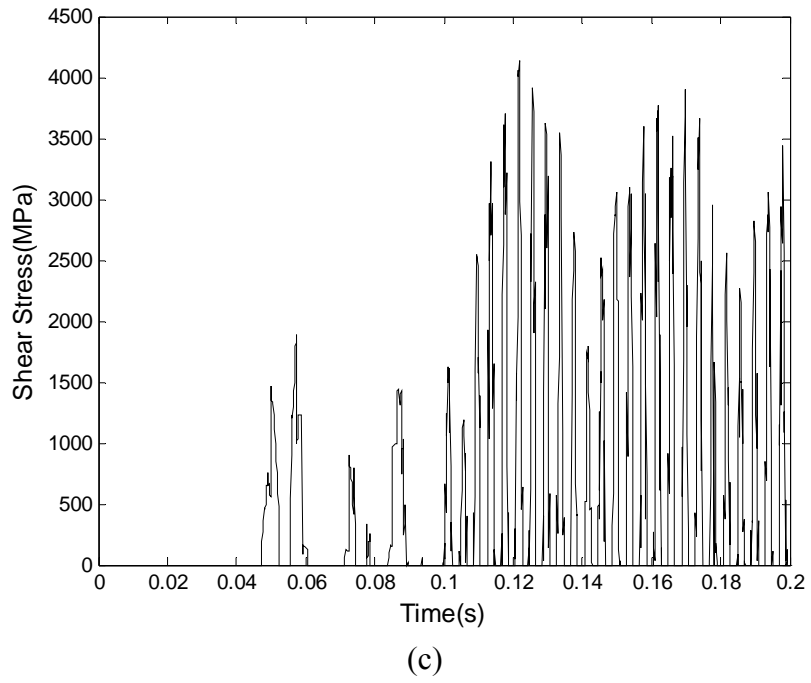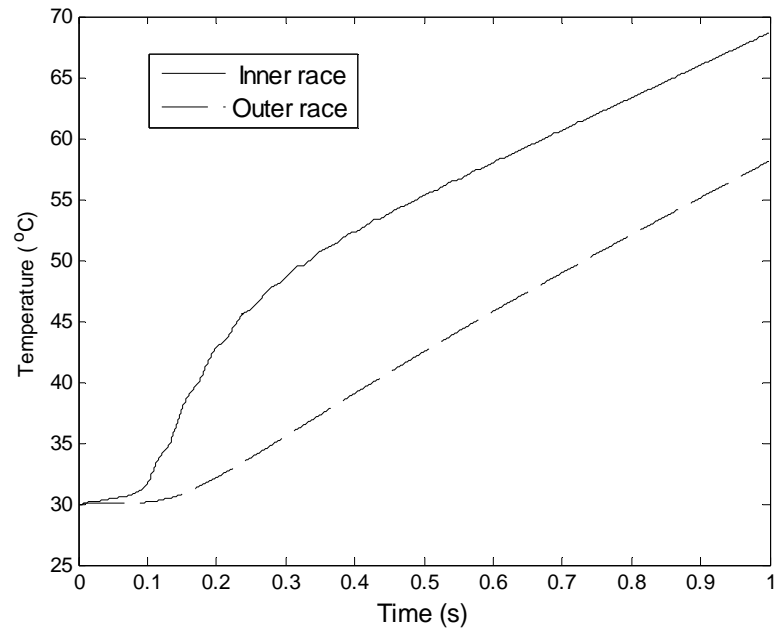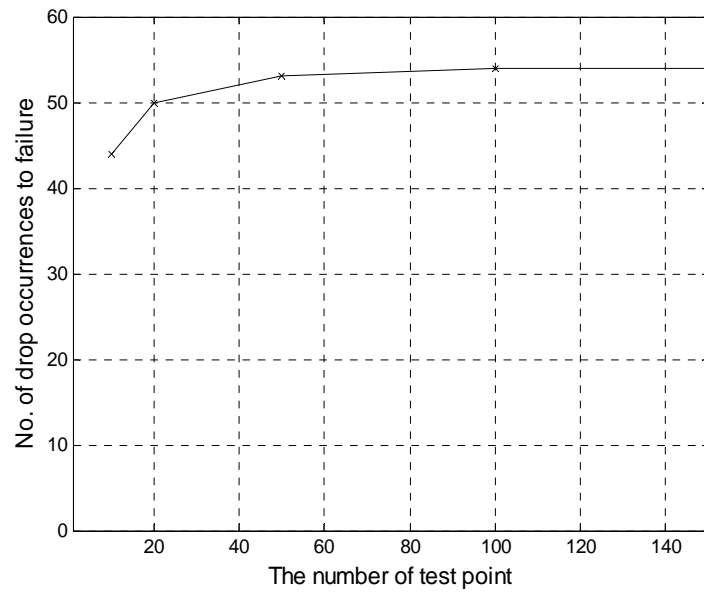
Fig. 2.9 Continued

(e)
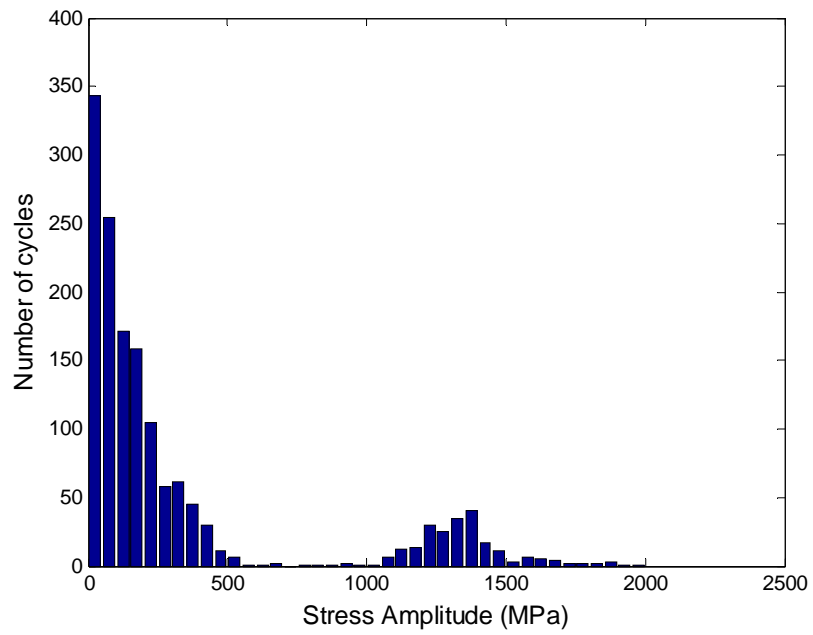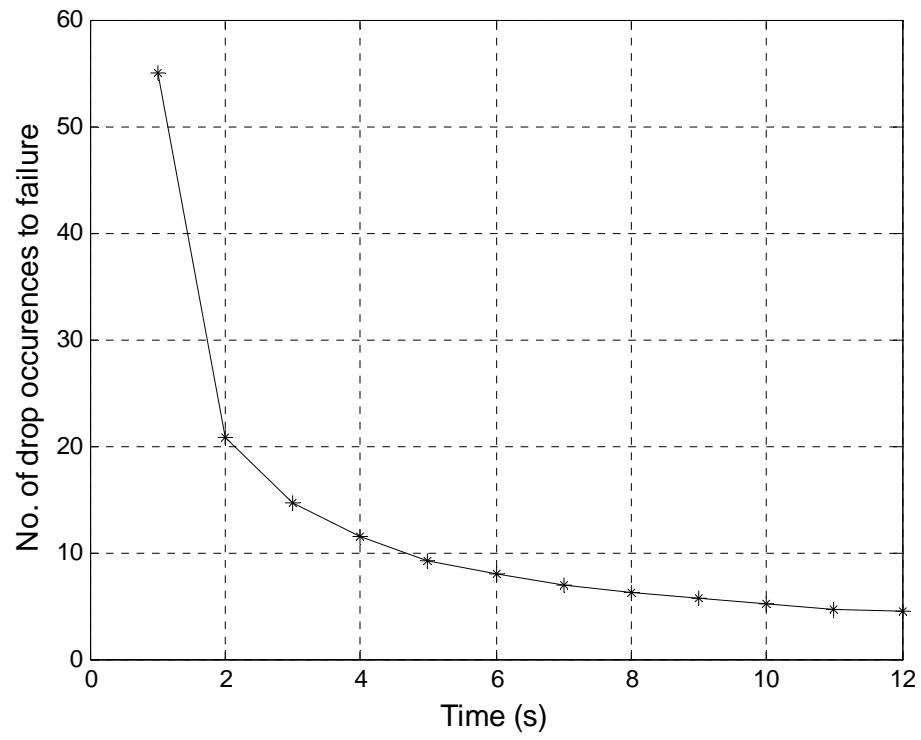

(f)

Fig. 2.9 Continued

(a)

(b)

Fig. 2.10 Cumulative Damage; (a) Damage vs Test Point Location for a Single

Rotor Drop Event, (b) No. of Drop Occurrences to Failure vs the Number of Test P

oints, and (c) No. of Drop Occurrences to Failure vs Time

(c)

Fig. 2.10 Continued

2.4.1 Support Effects

Comparisons of Figure 2.11 (a) vs. (b), Figure 2.12(a) vs (b) and Figure 2.13 (a) vs. (b) result in the following conclusions for the case of doubling the support stiffness. Figure 2.14 shows the Rainflow histogram of effective shear stresses defined by Eq. (2.46). Although the orbits are similar exhibiting a strong backward whirl motion, the cycles of peak stress amplitudes (>1.6GPa) are seen to significantly increase as shown in Figure 2.13's Rainflow Histogram, and the life prediction decreases from 4 for the nominal case to 2 for the higher stiffness case as shown in Table 2.5. In addition, the duration of backward whirl motion for the high stiffness case decreases by 66%. The reason is that the inner race speed is quickly decreased due to higher drag force induced by thermal load defined in Eq (2.9).

Comparisons of Figure 2.11 (a) vs. (c), Figure 2.12(a) vs (c) and Figure 2.13 (a) vs. (c) result in the following conclusions for the case of doubling the support damping. The orbits show a much weaker backward whirl motion which totally diminishes, the cycles of peak stress amplitudes (>1.0GPa) are seen to significantly decrease as shown in Figure 2.13's Rainflow Histogram, and the life prediction increases from 4 for the nominal case to 340 for the higher damping case as shown in Table 2.5.

2.4.2 Journal - Inner Race Contact Friction Effect

Table 2.4 - Case 3 considers a drop in static friction by a factor of 3 and in kinetic friction by a factor of 2. This causes the inner race to accelerate much slower as shown in Figure 2.14. Comparisons of Figure 2.11 (a) vs. (d), Figure 2.12(a) vs (d) and Figure

2.13 (a) vs. (d) result in the following conclusions for the case of reduced friction. The orbits show an elimination of backward whirl, the cycles of peak stress amplitudes (>1.0GPa) are negligible as shown in Figure 2.13's Rainflow Histogram, and the life prediction increases from 4 for the nominal case to 82,000 for the reduced friction case as shown in Table 2.5.

Table 2.5 Life Prediction Summary

|	Nominal Case	Case #1	Case #2	Case #3	Case #4	Case #5	Case #6
Temperature of Inner Race (^oC)	131	197	49	43	164	45	56
Temperature of Outer Race (^oC)	130	196	44	33	163	37	52
No. of Drop Occurrences to Failure	4	2	340	82,000	2	8,200	30
Time to Backward Whirl Motion Cessation (sec)	12	8	1	1	9	1	4

2.4.3 Catcher Bearing Air Gap Size Effect

Comparisons of Figure 2.11 (a) vs. (e), Figure 2.12 (a) vs (e) and Figure 2.13 (a) vs. (e) result in the following conclusions for the case of increasing the air gap by 66%. The orbits show a strong backward whirl motion and a large increase in peak motion, the cycles of peak stress amplitudes above 1.5GPa slightly increase as shown in Figure 2.13 's Rain-flow Histogram, and the life prediction decreases from 4 for the nominal case to 2 for the larger clearance case as shown in Table 2.5. Like case (a), the duration of back ward whirl motion decreases by 75% due to higher thermal load.

2.4.4 Applied Side Load Effect

Comparisons of Figure 2.11 (a) vs. (f), Figure 2.12(a) vs (f) and Figure 2.13 (a) vs. (f) result in the following conclusions for the case of applying a 500N side load at each magnetic bearing. This type of event may occur e.g. during controller tuning if control is accidentally lost due to instability at high speed, so that magnetic bearing power is still available to apply the side loads for mitigating the vibrations of the rotor on the catcher bearings. The orbits show an elimination of backward whirl, the peak contact force decreases by a factor of 6, the cycles of peak stress amplitudes (>1.0GPa) are negligible as shown in Figure 2.13's Rainflow Histogram, and the life prediction increases from 4 for the nominal case to 8200 for the applied side load case as shown in Table 2.5.
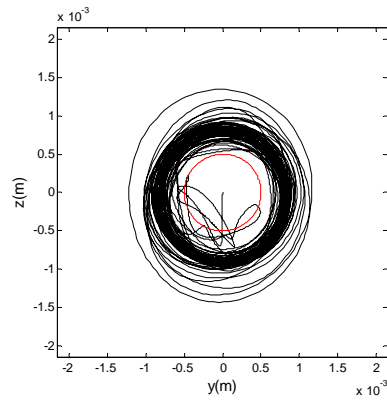
(a) Nominal case   (b) Case #1
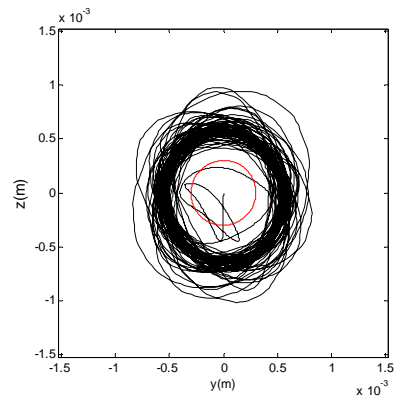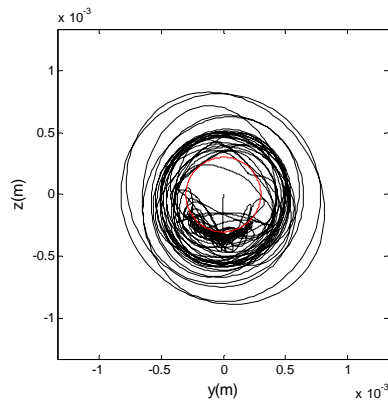
(c) Case #2   (d) Case #3
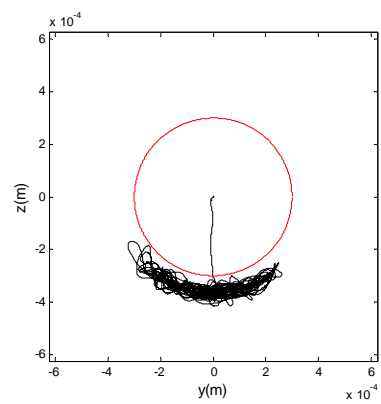
(e) Case #4   (f) Case #5

Fig. 2.11 Orbit Plot for Each Simulation Cases
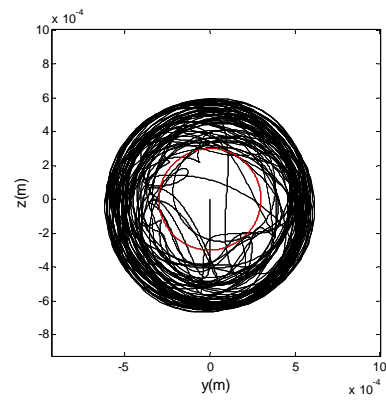
(g) Case #6

Fig. 2.11 Continued
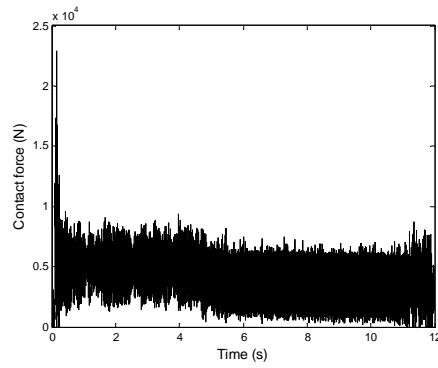
(a) Nominal case
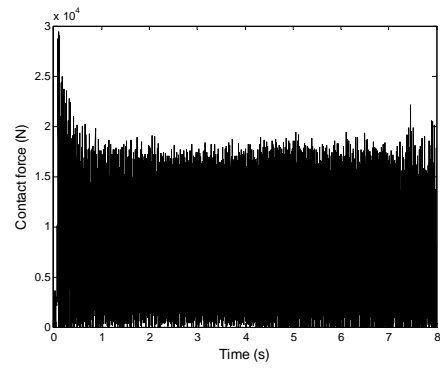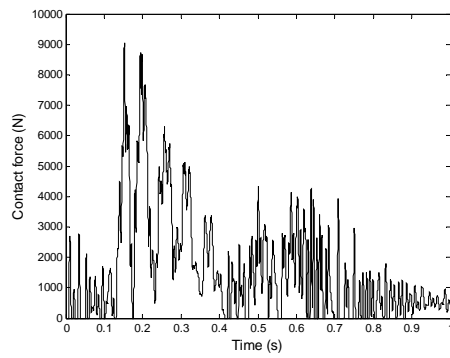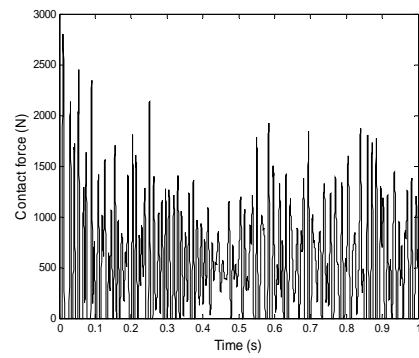
(b) Case #1
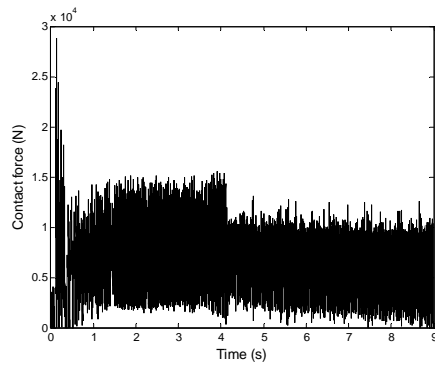
(c) Case #2
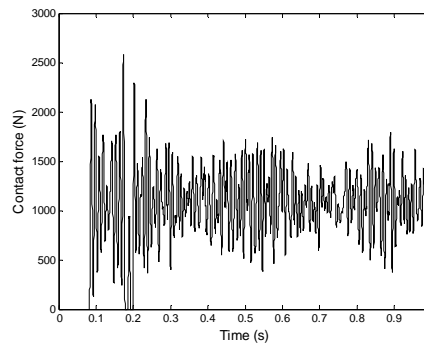
(d) Case #3

(e) Case #4

(f) Case #5

Fig. 2.12 Contact Force vs Time
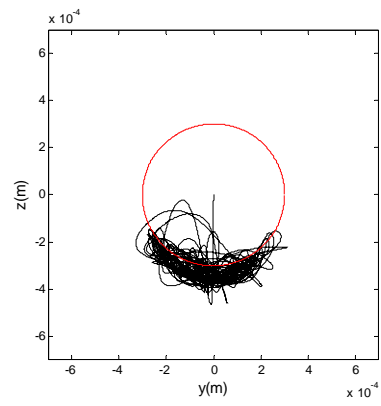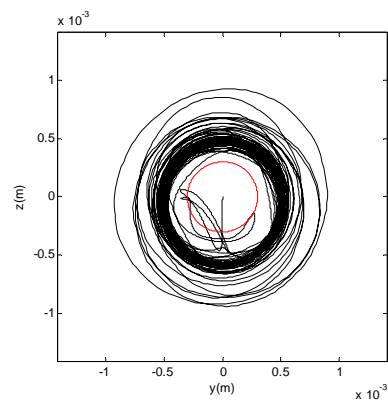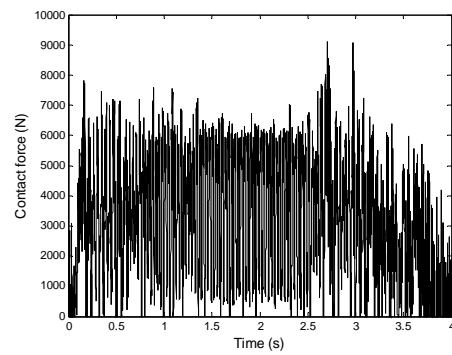
(g) Case #6

Fig. 2.12 Continued
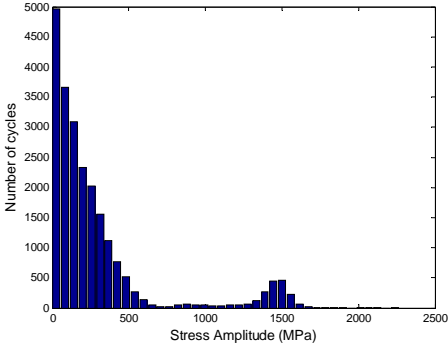
(a) Nominal case
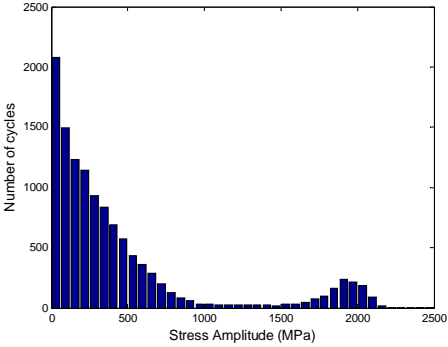
(b) Case #1
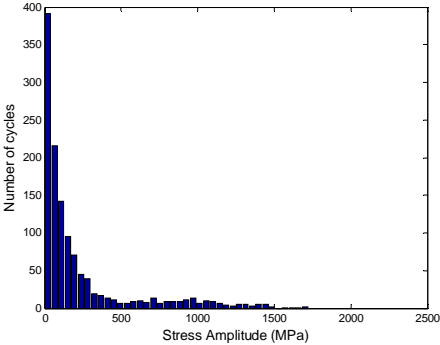
(c) Case #2
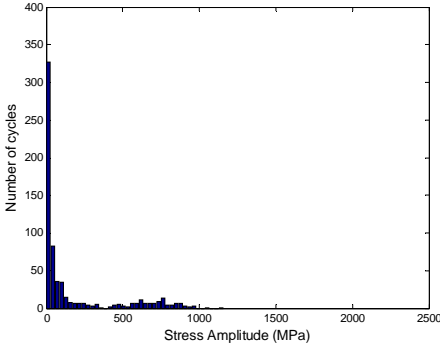
(d) Case #3
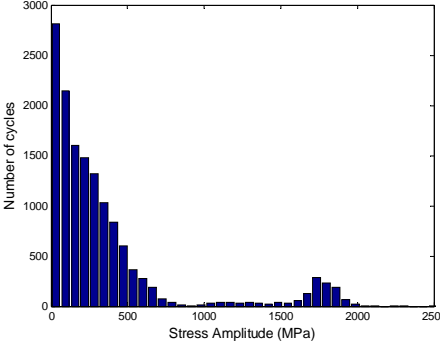
(f) Case #5
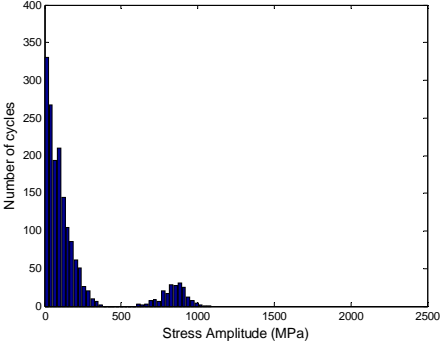
(g) Case #6

Fig. 2.13 Shear Stress Amplitude Rainflow Histogram
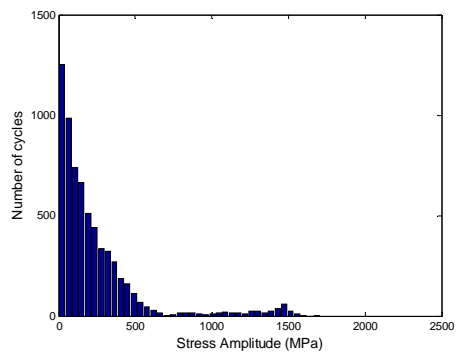
(e) Case #4

Fig. 2.13 Continued
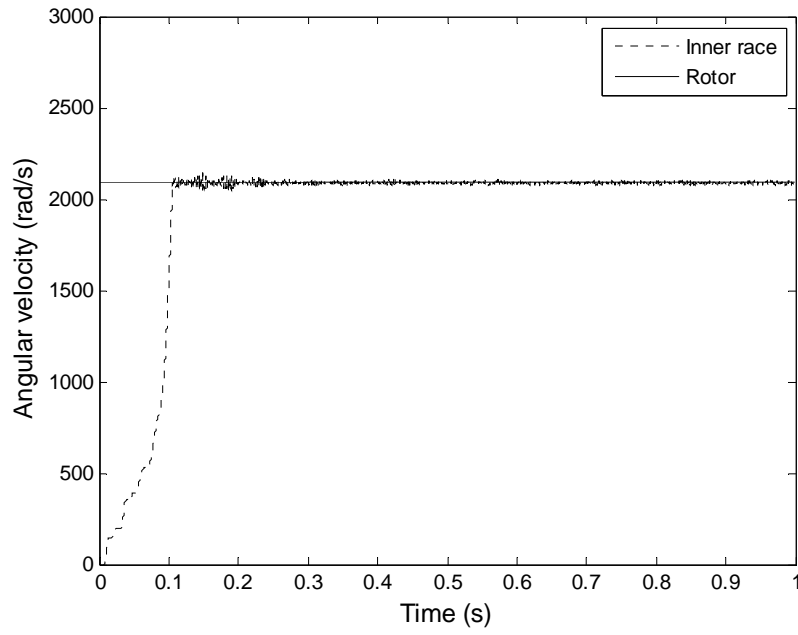
(a)
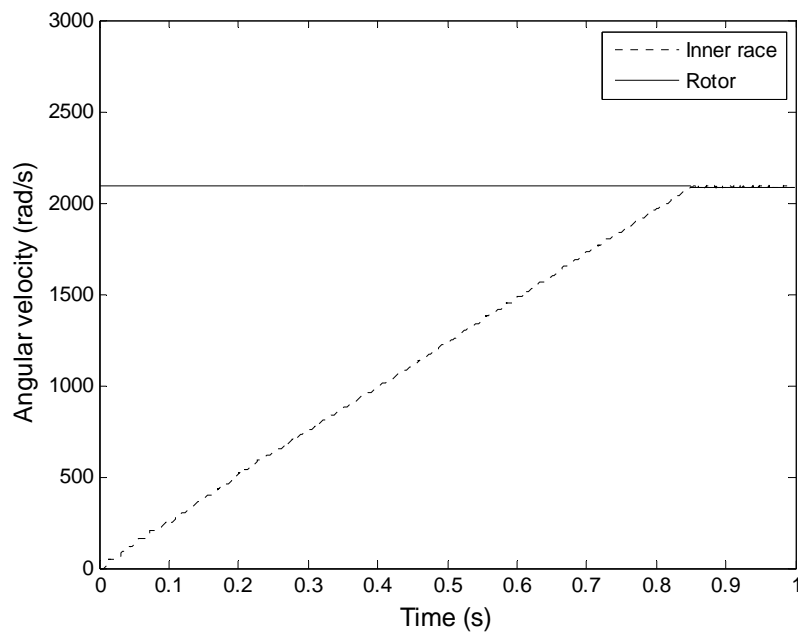
(b)

Fig. 2.14 Angular Velocities of Inner Race and Rotor: (a) $\mu_s = 0.3$, $\mu_d = 0.4$,

(b) $\mu_s = 0.1$, $\mu_d = 0.2$

2.4.5 Rotor Drop Speed (rpm) Effect

Comparisons of Figure 2.11 (a) vs. (g), Figure 2.12(a) vs (g) and Figure 2.13 (a) vs. (g) result in the following conclusions for the case of decreasing the drop speed by 50%. The orbits show a weak backward whirl motion, the peak contact force decreases by 40%, the cycles of stress amplitudes through the whole range significantly decrease as shown in Figure 2.13's Rainflow Histogram, and the life prediction increases from 4 for the nominal case to 30 for the lower speed case as shown in Table 2.5. The 8X significant increase in the no. of drop occurrence to failure by is due to the shorter duration of backward whirl motion and lower temperature increase in the CB. As the rotor speed increases, the temperature sharply heats up and life of CB decreased shown in Figure 2.15.
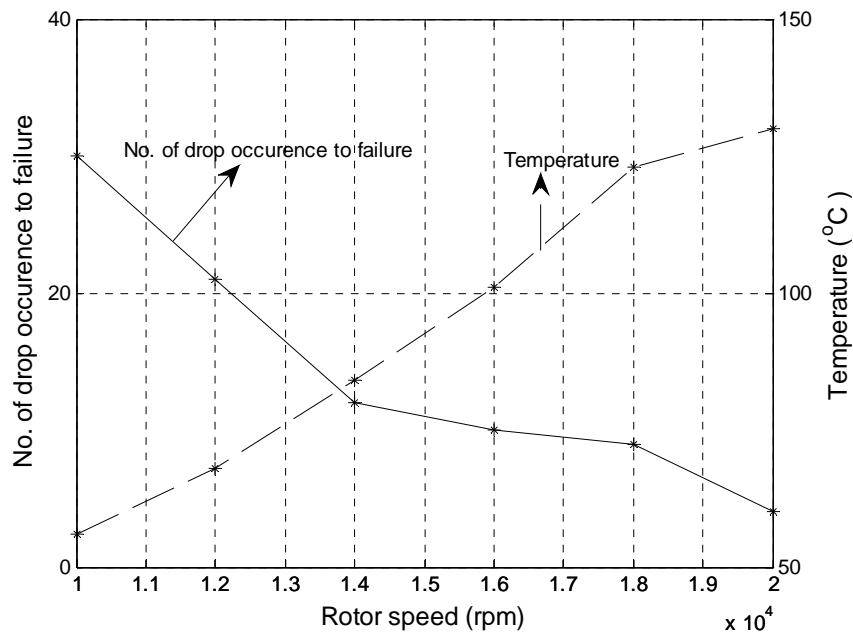
Fig. 2.15 Number of Drop Occurrence to Failure and Peak Temperature

vs Rotor Speed

CHAPTER III

THE MORTON EFFECT

3.1 Overview

The synchronous thermal instability known as to Morton Effect which is due to asymmetric temperature distribution of journal is presented in this chapter.

In the section 3.2, the mathematical model for tilting pad journal bearing is presented, and governing equation for pressure, generalized Reynolds equation for pressure, is used. To verify the developed model, the synchronous dynamic coefficients are compared with references.

In the section 3.3 thru 3.6, the energy equation is introduced to calculate temperature distribution in the fluid film. For countering and minimizing the numerical oscillations and for insuring a converged solution void of numerical oscillations, the upwind scheme is employed. The temperature distribution in the fluid film from the developed models is compared with the references. The heat conduction equation of the journal is presented in the section 3.4. The flexible FE rotor model including imbalance due to asymmetric temperature distribution of the journal is described in the section 3.5. In order to reduce the computation time, the thermal mode approach and staggering method is proposed in the section 3.6.

In the last section 3.7, the generalized Reynolds, energy, EOM of rotor, and heat conduction equation are simultaneously solved for the Morton Effect. The simulation results for plain and tilting pad journal bearing cases are compared with references.

3.2 Theoretical Model

3.2.1 Tilting Pad Journal Bearing

The tilting pad in shown in Figure 3.1 consists of five pads. Unlike the plain journal bearing geometry, the tilt pad journal bearing has two clearances; the bearing clearance C_b and the pad clearance C_p defined as

$$C_b = R_b - R_j$$
$$C_p = R_p - R_j \tag{3.1}$$
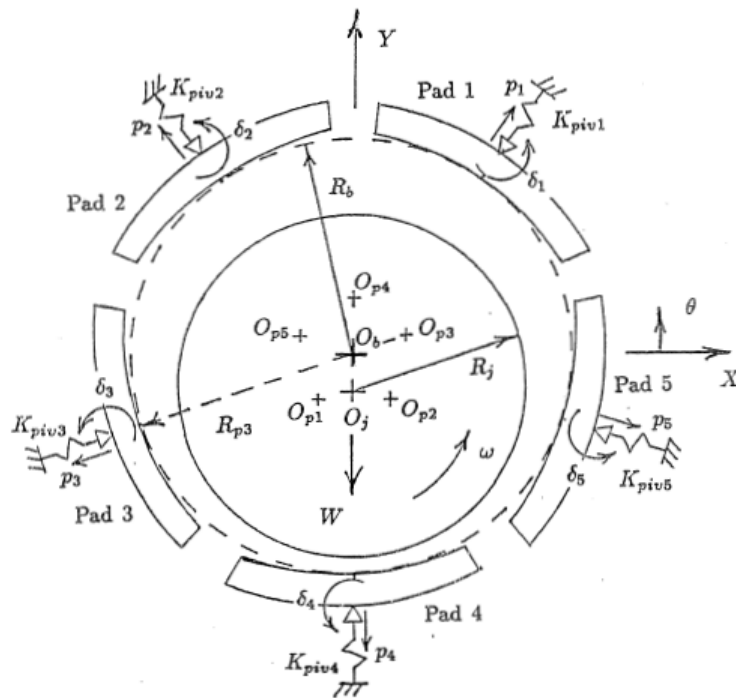
Fig. 3.1 Schematic of a Five Tilt Pad Bearing

Another parameter that is typical to tilt pad journal bearings and lobed bearings is the bearing preload m_b. This preload can be adjusted to achieve the required dynamic and static equilibrium characteristics. This preload can also be varied from one pad to another. The bearing preload is given as a function of the two clearances

$$m_b = 1 - \frac{C_b}{C_p} \tag{3.2}$$

Another parameter that can be adjusted to alter the bearing dynamic and static equilibrium characteristics is the pad offset. The pad offset is simply the location of the pivot with respect to the leading edge of the pad. For example, the offset is 0.5 if the pivot is at the center of the pad. Some researcher considered the pivot flexibility, but, in current research the pivot is assumed to be rigid.

The film thickness expression has to take into account the pad rotation, preload, and pivot offset. The fluid film thickness expression for the tilt pad bearing is expressed by

$$h = C_p - x\cos\theta - y\sin\theta - (C_p - C_b)\cos(\theta - \theta_p) - \delta R_j \sin(\theta - \theta_p) \tag{3.3}$$

Theta determines the location of the particular discretized element in the circumferential direction. A transient term in the Reynolds equation is the temporal derivative of the fluid film thickness given by

$$\frac{dh}{dt} = -\dot{x}\cos\theta - \dot{y}\sin\theta - \dot{\delta}R_j \sin(\theta - \theta_p) \tag{3.4}$$

3.2.2 Generalized Variable Viscosity Reynolds Equation

The governing equation for the fluid film to obtain pressures is the Reynolds equation. Since viscosity is a function of temperature, Reynolds equation has to be modified to accommodate this. While deriving the Reynolds equation the following assumptions are made

a. Body, forces and fluid inertia are negligible

b. Pressure distribution through the thickness is constant

c. Curvatures of the two surfaces are large compared to the film thickness

d. Newtonian fluid

e. No slip boundary condition at the solid fluid interface

f. Flow is laminar.

g. Mass density is independent of pressure and temperature.

The Reynolds equation is obtained from the 2D momentum equation and the continuity equations, which give pressure and velocity distribution. Integration of the momentum equation provides the velocity distribution in terms of pressure gradients and substitution of this velocity profile into the flow rate continuity equation, will give the Reynolds equation. The generalized variable viscosity Reynolds equation is expressed by

$$\nabla \bullet (C_1 \nabla p) + (\nabla C_2) \cdot (U_1 - U_2) + (\nabla h) \cdot U_1 + \frac{dh}{dt} = 0$$

$$C_1 = \int_0^h \int_0^z \frac{\zeta}{\mu} d\zeta \, dz - \frac{\int_0^h \frac{\zeta}{\mu} d\zeta}{\int_0^h \frac{1}{\mu} d\zeta} \int_0^h \int_o^z \frac{1}{\mu} d\zeta \, dz \qquad (3.5)$$

$$C_2 = \frac{\int_0^h \int_0^z \frac{1}{\mu} d\zeta \, dz}{\int_0^h \frac{1}{\mu} d\zeta}$$

The equations shown above work for a case where the upper and lower plates both are moving with respect to each other. For fluid film bearing, usually the upper plate represents the rotating shaft, while the lower plate represents the stationary bearing housing. Using these boundary conditions for the fluid film bearings, the variable viscosity Reynolds equation will reduce to

$$\nabla \bullet (C_1 \nabla p) + (\nabla C_2) \cdot (U) + \frac{dh}{dt} = 0 \qquad (3.6)$$

The variable viscosity Reynolds equation is used to solve for pressures when a thermohydrodynamic problem is considered. For a thermohydrodynamic problem viscosity is a function of temperature. For isoviscous problems, viscosity is constant throughout the fluid film, in which case the variable viscosity Reynolds equation becomes

$$\frac{\partial}{\partial x}\left(\frac{h^3}{12\mu}\frac{\partial p}{\partial x}\right) + \frac{\partial}{\partial z}\left(\frac{h^3}{12\mu}\frac{\partial p}{\partial z}\right) = U\frac{\partial h}{\partial x} \qquad (3.7)$$

Using the FEM method, we solved the variable viscosity Reynolds equations. Three node simplex triangular elements are used to discretize the fluid film. The

reference [42] clearly illustrated the derivation of the finite element formulation. The problem boundary is comprised of two regions, first, region over which pressure is prescribed and second, region over which flow/flux is prescribed. Only half the bearing length needs to be discretized because of symmetry of the bearing. At the centerline, no flux/flow condition is imposed. The Reynolds boundary condition for zero pressure in the cavitated region and zero normal, pressure gradient along the cavitation boundary is imposed on the numerical solution.

Reynolds equation is solved on each pad separately and simultaneously and later sum up. The force in the pad coordinate system can be evaluated as;

$$\begin{Bmatrix} F_r \\ F_t \end{Bmatrix} = 2\int_{\theta_1}^{\theta_2} \int_0^{L/2} P(\theta,Z)\begin{bmatrix} \sin\theta \\ \cos\theta \end{bmatrix} dZ\, d\theta \tag{3.8}$$

Subscripts r and t indicate the radial and tangential force acting on the pad respectively. θ is the circumferential coordinate on that particular pad. Similarly the sum of the moments on each pad about the pivot is evaluated;

$$M = 2\int_{\theta_1}^{\theta_2} \int_0^{L/2} \bar{r} \times P(\theta,Z)\begin{bmatrix} \sin\theta \\ \cos\theta \end{bmatrix} R_j dZ\, d\theta \tag{3.9}$$

where $\bar{r}$ is the distance between the location of θ and the pivot. The moments are needed for updating the pad tilt angles.

3.2.3 Determination of Linearized Dynamic Coefficients

For a given static load from weight, gear forces, hydraulic load, etc. the static equilibrium position is determined in order to provide a point about which the linearized

dynamic coefficients are next calculated. The requirement at the static equilibrium position is that, the resultant forces in the global coordinate directions should vanish. This can be shown as;

$$f_x = F_X - W \sin \alpha$$
$$f_y = F_Y - W \cos \alpha$$

(3.10)

A vector can be expanded using Taylor series in the following way;

$$F_{New} = F_{Cur} + \frac{\partial F}{\partial X} X_{Cur} (X_{New} - X_{Cur}) + \frac{\partial^2 F}{\partial X^2} X_{Cur} (X_{New} - X_{Cur})^2$$

(3.11)

The equations can be iteratively solved to find the updated journal positions until the equilibrium is achieved. This iterative scheme is also called 2D Newton Raphson scheme. The equations for the 2D Newton Raphson technique are

$$(X_{New} - X_{Cur}) \frac{\partial f_X}{\partial X}\bigg|_{X_{cur}, Y_{Cur}} + (Y_{New} - Y_{Cur}) \frac{\partial f_X}{\partial Y}\bigg|_{X_{cur}, Y_{Cur}} + f_X\big|_{X_{cur}, Y_{Cur}} = 0$$
$$(X_{New} - X_{Cur}) \frac{\partial f_Y}{\partial X}\bigg|_{X_{cur}, Y_{Cur}} + (Y_{New} - Y_{Cur}) \frac{\partial f_Y}{\partial X}\bigg|_{X_{cur}, Y_{Cur}} + f_Y\big|_{X_{cur}, Y_{Cur}} = 0$$

(3.12)

Given an initial guess, the simultaneous equations shown above are solved for the next equilibrium location. The partial derivatives are obtained by perturbing the journal location at the current equilibrium guess by a finite value data, in X and Y directions, and evaluating forces. In general, the finite perturbed values for displacement and tilt angle are selected by

$$\Delta X = \Delta Y = 0.01 \times C_b$$
$$\Delta \delta = 0.01 \times \delta_{allow}$$

(3.13)

where δ_{allow} is the allowable range of angles for each pad those do not cause an

interference between pad and journal. These partial derivatives in Eq.(3.12) are written

by

$$\frac{\partial f_X}{\partial X}\bigg|_{X_{cur},Y_{cur}} = \frac{F_X(X_{cur}+\Delta X,Y_{cur})-F_X(X_{cur}-\Delta X,Y_{cur})}{2\Delta X}$$

$$\frac{\partial f_X}{\partial Y}\bigg|_{X_{cur},Y_{cur}} = \frac{F_X(X_{cur},Y_{cur}+\Delta Y)-F_X(X_{cur},Y_{cur}-\Delta Y)}{2\Delta Y}$$

$$\frac{\partial f_Y}{\partial X}\bigg|_{X_{cur},Y_{cur}} = \frac{F_Y(X_{cur}+\Delta X,Y_{cur})-F_Y(X_{cur}-\Delta X,Y_{cur})}{2\Delta X}$$

$$\frac{\partial f_Y}{\partial X}\bigg|_{X_{cur},Y_{cur}} = \frac{F_Y(X_{cur},Y_{cur}+\Delta Y)-F_Y(X_{cur},Y_{cur}+\Delta Y)}{2\Delta Y}$$

(3.14)

The pad angles are adjusted to make the pad moments all zero at each iterative X and Y
position. This may be accomplished in one of the following ways

(a) Determine the allowable range of angles for each pad those do not cause an
interference between pad and journal. Increment the pad angle in fixed steps
through this range seeking the angle that causes the moment to have a zero
crossing. Repeat this for all pad angles.

(b) Same as (a) but utilized interval halving for angle search

(c) Same as (a) but utilized Newton Raphson for the angle search

The stiffness are defined by:

$$K_{XX}=-\frac{F_X(+\Delta X)-F_X(-\Delta X)}{2\Delta X},\ K_{XY}=-\frac{F_X(+\Delta Y)-F_X(-\Delta Y)}{2\Delta Y},\ K_{X\delta_j}=-\frac{F_X(+\Delta\delta_j)-F_X(-\Delta\delta_j)}{2\Delta\delta_j}$$

$$K_{YX}=-\frac{F_Y(+\Delta X)-F_Y(-\Delta X)}{2\Delta X},\ K_{YY}=-\frac{F_X(+\Delta Y)-F_X(-\Delta Y)}{2\Delta Y},\ K_{Y\delta_j}=-\frac{F_Y(+\Delta\delta_j)-F_Y(-\Delta\delta_j)}{2\Delta\delta_j}$$

$$K_{\delta_jX}=-\frac{M_j(+\Delta X)-M_j(-\Delta X)}{2\Delta X},\ K_{\delta_jY}=-\frac{M_j(+\Delta Y)-M_j(-\Delta Y)}{2\Delta Y},\ K_{\delta_j\delta_j}=-\frac{F_Y(+\Delta\delta_j)-F_Y(-\Delta\delta_j)}{2\Delta\delta_j}$$

(3.15)

The damping is computed in the same manner with the delta terms replaced by delta-dots (perturbation velocities). The finite perturbed velocities are selected by

$$\Delta \dot{X} = \Delta \dot{Y} = 0.01 \times \varpi \times C_b$$
$$\Delta \dot{\delta} = 0.01 \times \varpi \times \delta_{allow}$$

(3.16)

where ϖ is a spin speed *(rad/s)*.

The damping is defined by

$$C_{XX} = -\frac{F_X(+\Delta \dot{X}) - F_X(-\Delta \dot{X})}{2\Delta \dot{X}}, \quad C_{XY} = -\frac{F_X(+\Delta \dot{Y}) - F_X(-\Delta \dot{Y})}{2\Delta \dot{Y}}, \quad C_{X\delta_j} = -\frac{F_X(+\Delta \dot{\delta}_j) - F_X(-\Delta \dot{\delta}_j)}{2\Delta \dot{\delta}_j}$$

$$C_{YX} = -\frac{F_Y(+\Delta \dot{X}) - F_Y(-\Delta \dot{X})}{2\Delta \dot{X}}, \quad C_{YY} = -\frac{F_X(+\Delta \dot{Y}) - F_X(-\Delta \dot{Y})}{2\Delta \dot{Y}}, \quad C_{Y\delta_j} = -\frac{F_Y(+\Delta \dot{\delta}_j) - F_Y(-\Delta \dot{\delta}_j)}{2\Delta \dot{\delta}_j}$$

$$C_{\delta_j X} = -\frac{M_j(+\Delta \dot{X}) - M_j(-\Delta \dot{X})}{2\Delta \dot{X}}, \quad C_{\delta_j Y} = -\frac{M_j(+\Delta \dot{Y}) - M_j(-\Delta \dot{Y})}{2\Delta \dot{Y}}, \quad C_{\delta_j \delta_j} = -\frac{F_Y(+\Delta \dot{\delta}_j) - F_Y(-\Delta \dot{\delta}_j)}{2\Delta \dot{\delta}_j}$$

(3.17)

These stiffness and damping are non-frequency reduced values. These linearized dynamic coefficients in matrix are written by

$$K = \begin{bmatrix} K_{JJ} & K_{JP} \\ K_{PJ} & K_{PP} \end{bmatrix}, \quad C = \begin{bmatrix} C_{JJ} & C_{JP} \\ C_{PJ} & C_{PP} \end{bmatrix}$$

(3.18)

The calculated stiffness and damping are non-dimensional values defined by

$$K_{non} = \frac{C_p}{W} K_{dim}, \quad C_{non} = \frac{C_p \omega}{W} C_{dim}$$

3.2.4 Synchronously Reduced Dynamics Coefficients

API standard defined the linear dynamic coefficients as the synchronously reduced dynamic coefficients. This is the type of tilting pad journal bearing coefficient required in the unbalance response and stability analyses required by API 617. The synchronously reduced dynamic coefficients are defined by

$$C^*_{JJ} = \frac{1}{\nu} \cdot imag(Z_{JJ} - Z_{JP}Z^{-1}_{PP}Z_{PJ})$$

$$K^*_{JJ} = \frac{1}{\nu} \cdot real(Z_{JJ} - Z_{JP}Z^{-1}_{PP}Z_{PJ})$$

(3.19)

where

$$Z_{JJ} = i\nu C_{JJ} + K_{JJ}$$
$$Z_{JP} = i\nu C_{JP} + K_{JP}$$
$$Z_{PJ} = i\nu C_{PJ} + K_{PJ}$$
$$Z_{PP} = i\nu C_{PP} + K_{PP} - \nu^2 M_{PP}$$

where ν is the spin speed for synchronously reduced coefficients.

3.2.5 Verification

The present model is compared with reference[43]. Figure 3.2 shows the 5 pad tilt pad bearing and its geometry. According to pressure distribution shown in Figure 3.3, the pad 1,2 are unloaded. The obtained results are listed in Table 3.1 and 3.2. As seen from the results shown in the tables, a very good agreement was obtained. This confirms the validity of the current approach.
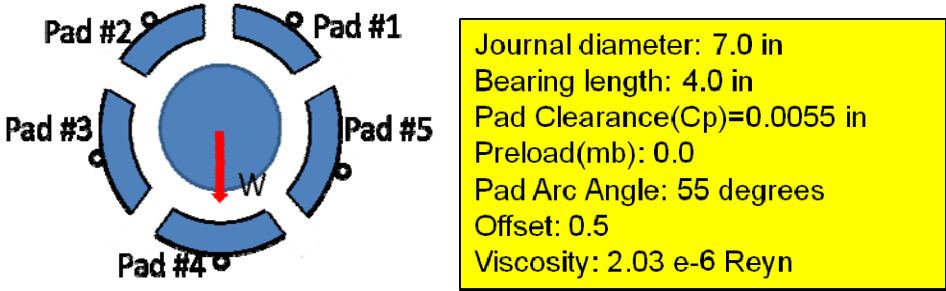
Fig. 3.2 Five Tilt Pad Bearing Geometry
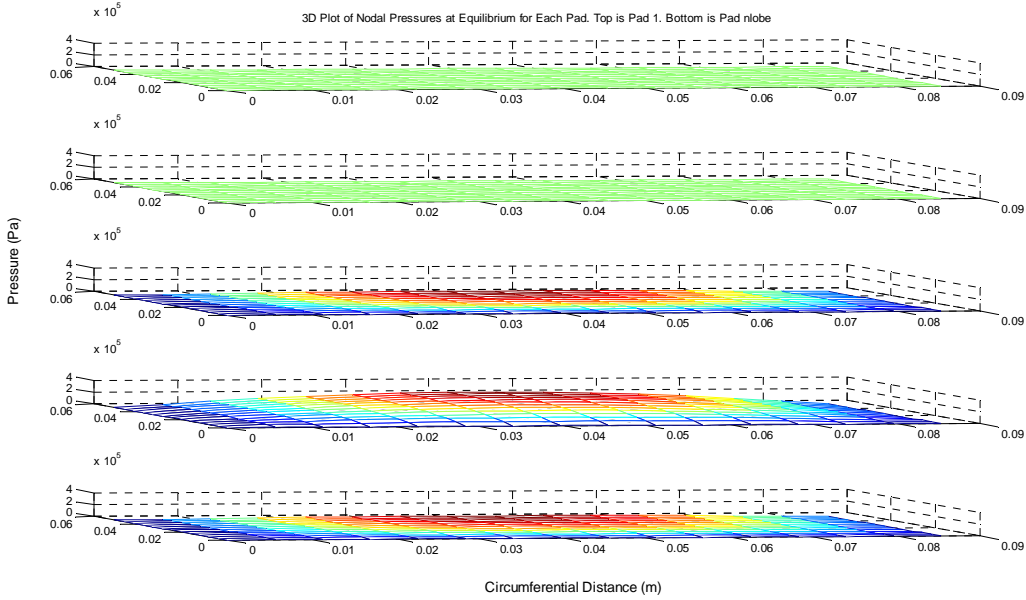
Fig. 3.3 Pressure Distribution at EP

Table 3.1 Full (non-dimensional) Dynamic Coefficients; (a) Stiffness and (b)

Damping

(a)

	X	Y	P1	P2	P3	P4	P5
X	1.46 [1.5]	1.81 [1.8]	0	0	-0.95 [-1.0]	0.36 [0.4]	0.99 [1.0]
Y	-4.12 [-4.1]	5.18 [5.2]	0	0	-0.35 [-0.4]	-3.90 [-3.9]	-0.27 [-0.3]
P1	0	0	0	0	0	0	0
P2	0	0	0	0	0	0	0
P3	0.03 [0.03]	-0.04 [-0.04]	0	0	0.04 [0.04]	0	0
P4	0.36 [0.4]	-0.03 [-0.03]	0	0	0	0.36 [0.36]	0
P5	-0.003 [0.003]	0.05 [0.05]	0	0	0	0	0.04 [0.04]

(b)

	X	Y	P1	P2	P3	P4	P5
X	3.88 [3.9]	-0.32 [-0.3]	0	0	-0.03 [-0.03]	0.19 [0.2]	0.06 [0.05]
Y	-0.32 [-0.3]	8.32 [8.3]	0	0	-0.06 [-0.06]	-0.38 [-0.4]	0.03 [0.03]
P1	0	0	0	0	0	0	0
P2	0	0	0	0	0	0	0
P3	-0.03 [-0.03]	-0.06 [-0.06]	0	0	0.05 [0.05]	0	0
P4	0.19 [0.2]	-0.38 [-0.4]	0	0	0	0.19 [0.05]	0
P5	0.06 [0.05]	0.03 [0.03]	0	0	0	0	0.05 [0.05]

Table 3.2 Synchronously, Non-dimensional) Reduced Dynamic Coefficients; (a)

Stiffness and (b) Damping

(a)

	X	Y
X	0.57[0.55]	0[0]
Y	0[0]	3.42 [3.4]

(b)

	X	Y
X	2.46[2.5]	0[0]
Y	0[0]	4.83 [4.8]

3.3 Calculation of Lubricant Temperature in the Bearing's Oil Film

3.3.1 Energy Equation

The temperature distribution in the fluid film is governed by the energy equation. The solution of the energy equation requires pressure distribution, velocity distribution, and viscosity distribution. The Reynolds equation and the energy equation are coupled via the viscosity distribution. When the problem is solved for constant viscosity, the energy equation need not be solved, and the Reynolds equation and the energy equation are both uncoupled. The updated viscosity distribution is used in solving the Reynolds equation.

For a laminar, incompressible, Newtonian fluid, the energy equation is given by

$$\rho c_p \left(\frac{\partial T}{\partial t} + u \frac{\partial T}{\partial x} + v \frac{\partial T}{\partial y} \right) = k \left(\frac{\partial^2 T}{\partial x^2} + \frac{\partial^2 T}{\partial y^2} \right) + \mu \left[\left(\frac{\partial u}{\partial y} \right)^2 + \left(\frac{\partial w}{\partial y} \right)^2 \right] \qquad (3.20)$$

Viscosity has a strong dependence on temperature and a weak dependence on pressure. Viscosity is assumed to follow an exponential relationship given by

$$\mu = \mu_0 e^{-\beta(T-T_0)} \qquad (3.21)$$

The finite element method FEM method is utilized for solving energy equation. Four node isoparametric elements are used for discretizing the problem domain. The derivation of the "weak" form of this problem, and full finite element formulation is illustrated in reference [42]. The following boundary conditions are applied for all the cases except for the Morton effect simulation:

 (a) The mixing temperature theory [44] is used for the supply temperature.

(b) The shaft temperature is assumed not to vary circumferentially.

The shaft   temperature is given as a constant at the shaft fluid film interface.

(c) The bearing is assumed to be insulated. This is a good valid assumption as the solution obtained using this boundary condition will always give a temperature field which is hotter than when there is heat transfer to surroundings. This will give a conservative solution.

(d) For the cavitation region, the dissipation term in the energy equation is set to zero. In addition, when cavitation occurs, the film thermal conductivity is replaced with air thermal conductivity.

3.3.2 Upwind Scheme [45]

The finite element formulation yields the set of algebraic equations for nodal temperatures;

$$[B_T]\{T\} = \{F_T\} \tag{3.22}$$

This set of equations can be solved using any unsymmetric banded solver. Matrix Bt contains the coefficients obtained from the convection and conduction terms, while vector T contains the temperatures, and the vector $\{F_T\}$ contains the coefficients of the dissipative term and boundary conditions.

The presence of first order derivatives in the energy equation causes the solution to oscillate about its exact value. Whenever these first order derivatives increase in magnitude, the numerical oscillations in solution increase resulting in erroneous results. For countering and minimizing the numerical oscillations and for insuring a converged

solution void of numerical oscillations, the classical Galerkin scheme is modified by employing upwind techniques. In these techniques isoparametric shape functions are retained, but, the weight functions are modified depending on the magnitude and direction of the local flow parameter, the Peclet number. The modified weight function can be represented as;

$$W(\eta, \zeta) = N(\eta, \zeta) + \alpha F(\eta, \zeta) \qquad (3.23)$$

N is the shape function for isoparametric element, while alpha is a variable function of the magnitude and direction of flow, and the local Peclet number, and varies from 0(classical Galerkin scheme) to 1(full upwinding), and F is the polynomial upwinding function whose order can be varied.

The one dimensional isoparametric shape function are given by

$$N_1(\zeta) = \frac{1}{2}(1 - \zeta)$$

$$N_2(\zeta) = \frac{1}{2}(1 + \zeta)$$

$$N_3(\zeta) = \frac{1}{2}(1 + \zeta)$$

$$N_4(\zeta) = \frac{1}{2}(1 - \zeta) \qquad (3.24)$$

The natural coordinate direction is shown in the Figure 3.4 for a typical 4 node isoparametric element. The one dimensional shape functions for the other coordinates are also similar, and denote by N. The shape function for a four node bilinear isoparametric element then becomes;

$$N_i(\eta,\zeta) = N_i(\eta)N_i(\zeta) \tag{3.25}$$

The corresponding one dimensional weight function in η and ς coordinate directions are given by

$$W_i(\eta) = N_i(\eta) + \alpha_{ij}\frac{3}{4}(1-\eta)(1+\eta)$$

$$W_i(\zeta) = N_i(\zeta) + \beta_{ij}\frac{3}{4}(1-\zeta)(1+\zeta) \tag{3.26}$$

α and β are upwinding parameters dependent on the local velocity magnitude and direction on the side i-j of the element. These parameters are functions of local velocity, element size, and thermal conductivity. The local Peclet number can be defined as

$$Pe = \frac{u_{ij}h}{k} \tag{3.27}$$

In the above equation, h is the element size in the direction of interest, k is the thermal conductivity, and U_{ij} is the velocity of the side i-j of the element under consideration. This velocity is given by

$$u_{ij} = \frac{1}{2}(u_i + u_j)\cdot l_{ij} \tag{3.28}$$

In the above equation u_i and u_j represent the velocity vectors at the nodes i and j, and the directional unit vector is given by l_{ij} for the side i-j. The 2 dimensional weight functions then, can be represented as;

$$W_i(\eta,\zeta) = W_i(\eta)W_i(\zeta) \tag{3.29}$$

The value of alpha and beta can be varied manually from 0 to 1 or an optimum value can be found depending on the local Peclet number as follows;

$$\alpha_{ij} = \beta_{ij} = (\coth(\frac{Pe}{2})) - \frac{2}{Pe} \qquad (3.30)$$

To check the validity of including upwinding in the energy equation finite formulation, simple 2D problem is solved. Its problem domain and boundary conditions are shown in Figure 3.5.The results shown in Figure 3.6 show a minimization in the numerical oscillations with the inclusion of upwinding.
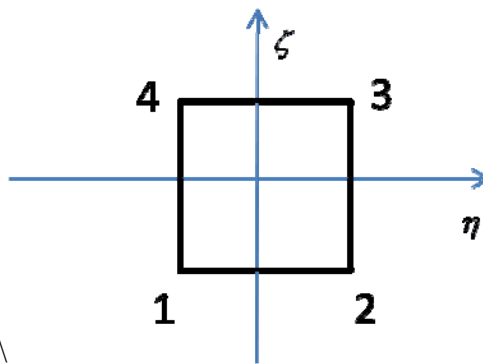
Fig. 3.4   Four Node Isoparametric Element in Natural Coordinate Domain
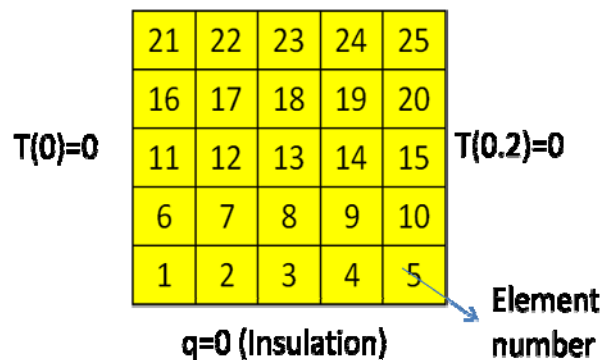
Fig. 3.5 Model Verification for Steady State Energy Equation, 2D Problem Domain and Boundary Condition
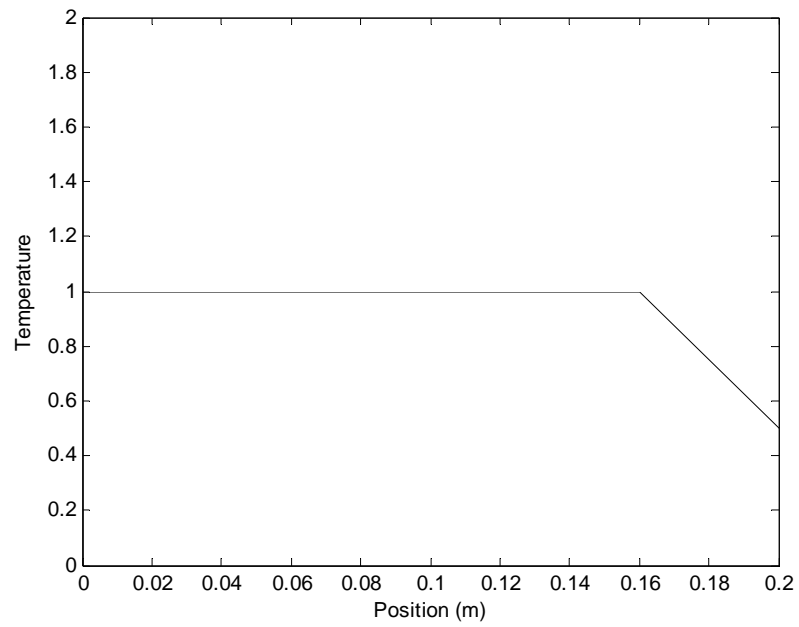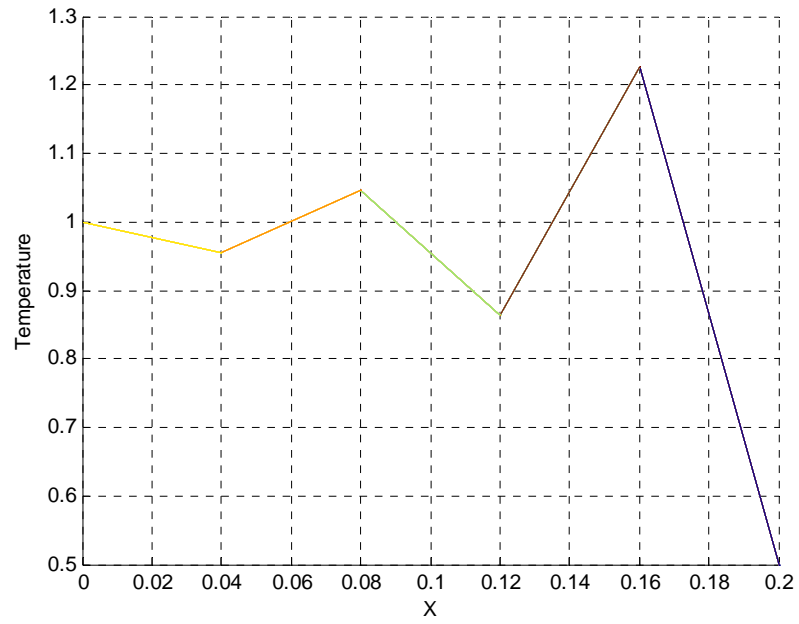
Fig. 3.6 Model Verification for Steady State Energy Equation; Results for U=95,

with and without Upwinding

3.3.3 Verification

The developed model compared with reference [46]. Figure 3.7 shows the 4 pad tilt pad bearing and its geometry. As mentioned earlier, to solve Energy equation, pressure distribution determined. Figure 3.8 shows the pressure distribution for each pad. Figure 3.9 shows the film thickness (unit: $10^{-5} m$) and temperature ($^{\circ}C$) distribution. The film thickness of pad #1,2 is greater than that of pad #3,4. As the film thickness decreases, the temperature in the lubricant also increases. Comparison is made between current simulation results and reference [46].

Journal diameter: 0.1 m
Bearing length: 0.07 m
Radial Pad Clearance(Cr)=0.160e-3 m
Preload(mb): 0.47
Pad Thickness:0.02 m
Pad Arc Angle: 75 degrees
Offset: 0.5
Viscosity: 0.0277 at 40 ℃
Thermoviscosity coefficient: 0.034
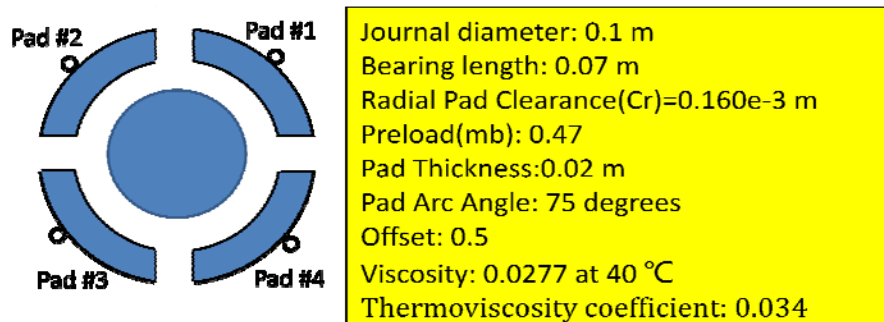
Fig. 3.7 Four Tilt Pad Bearing Geometry
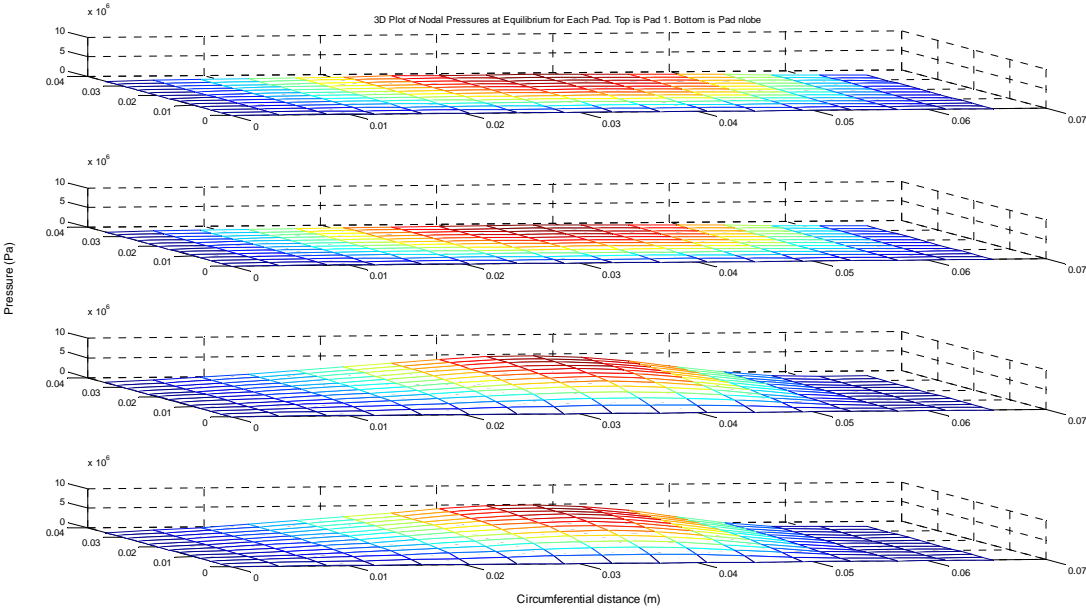
Fig. 3.8 Pressure Distribution at Each Pad
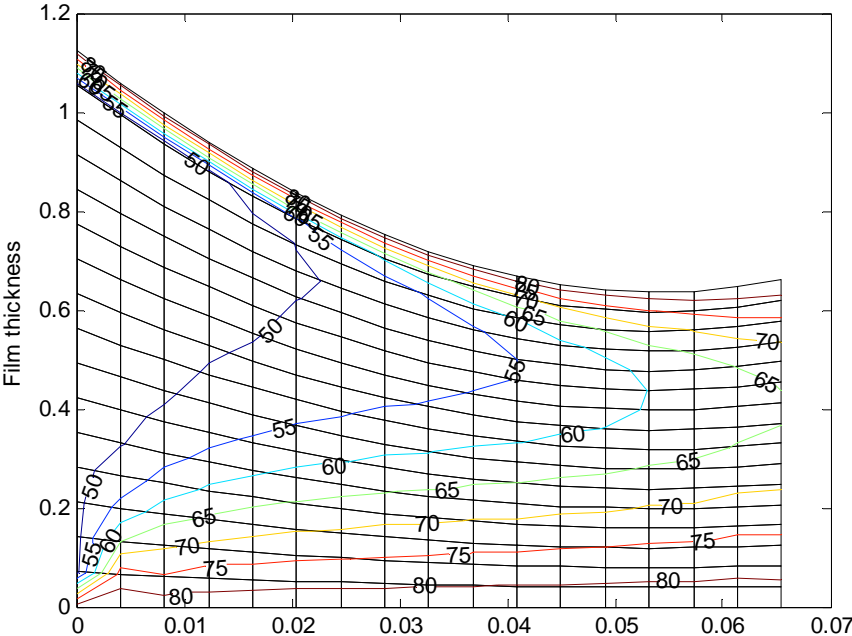
(a) Pad #1
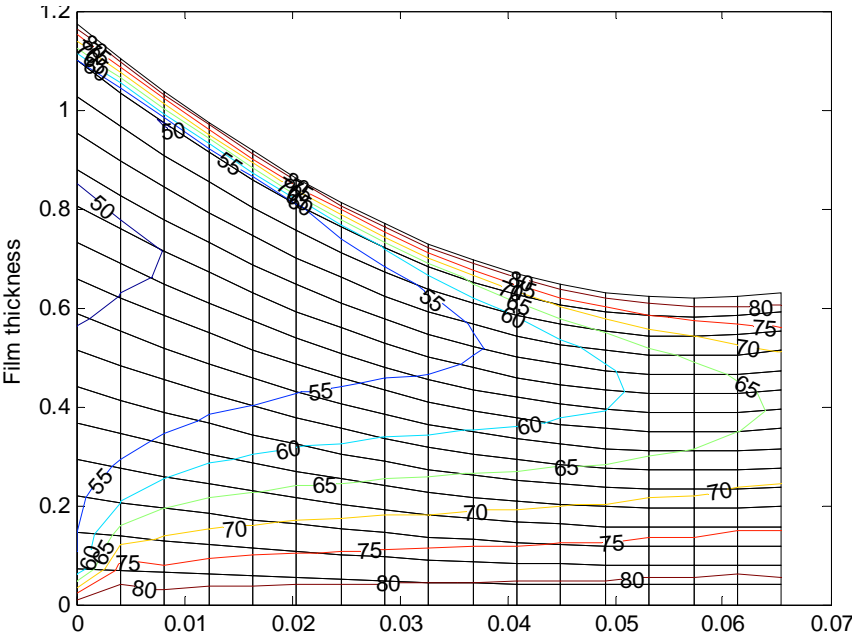
(b) Pad #2

Fig. 3.9 Temperature Distribution at Each Pad
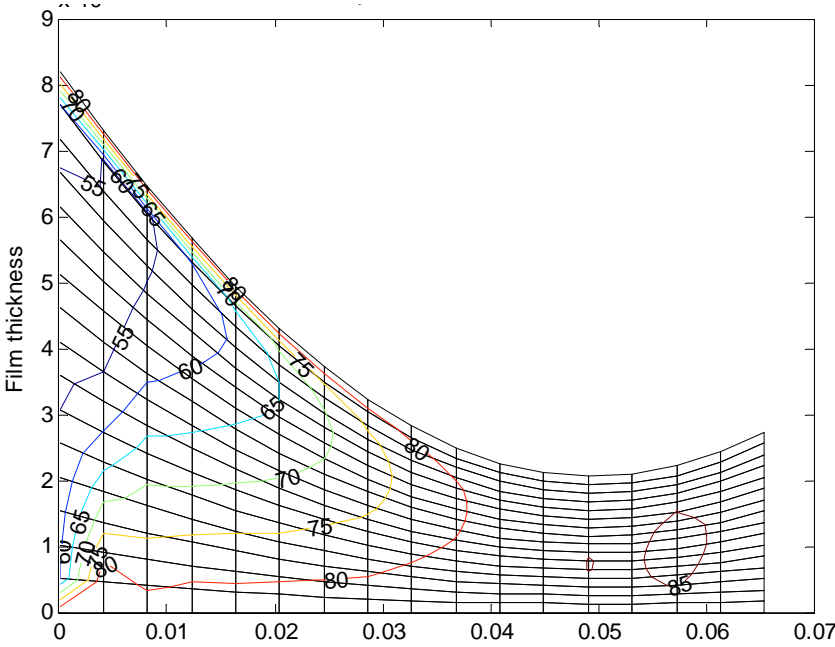
(c) Pad #3
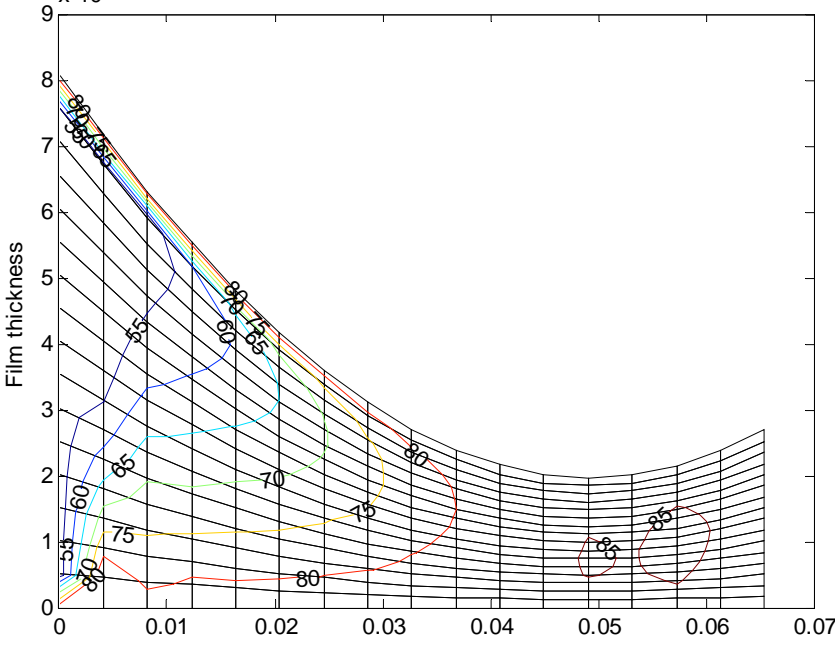
(d) Pad #4

Fig. 3.9 Continued
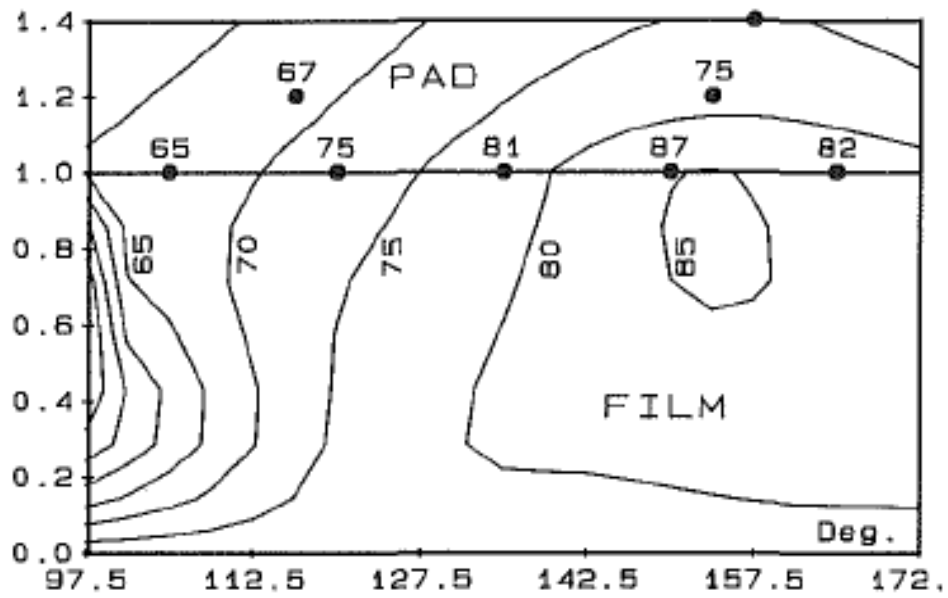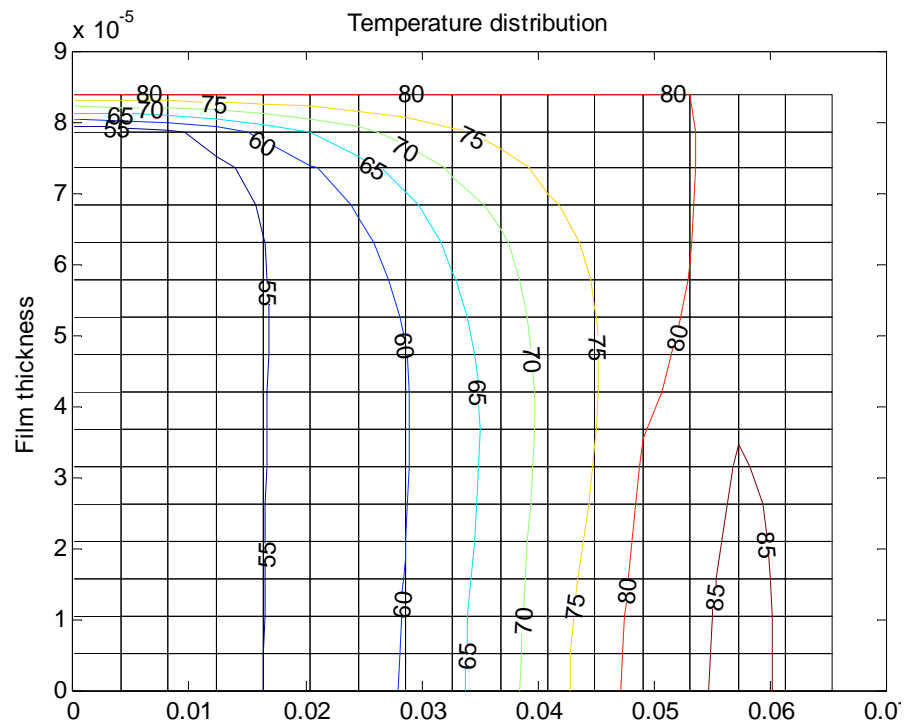
Fig. 3.10 Temperature Distribution Comparison

The temperature distribution at pad #3 shown in Figure 3.10 is compared with reference[46]. In the current research, there is no heat transfer through pad, but, in reference[46] heat transfer between lubricant and pad or surroundings is considered. Due to such boundary condition, the temperature distribution is slightly different from results from reference[46]. Figure 3.11 presents both theoretical and experimental temperature variation. The big difference is that the current model did not consider elastic deformation of pad. But, the theoretical temperature profile is similar to experiment.
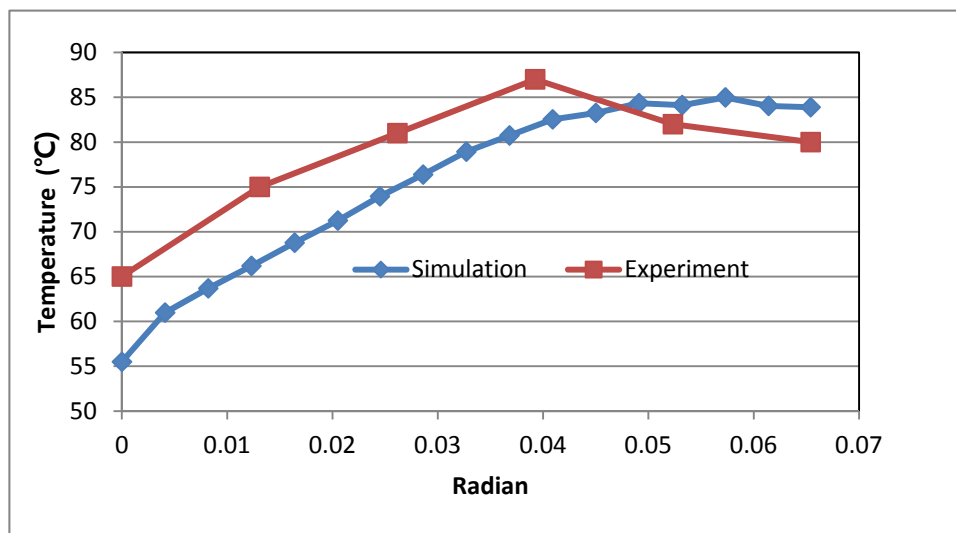
Fig. 3.11 Temperature Distribution; Theory and Experiment

3.4 Heat Conduction Equation

The journal temperature distribution is calculated by solving the transient heat conduction given by

$$\frac{\partial^2 T}{\partial x^2} + \frac{\partial^2 T}{\partial y^2} = \frac{\rho c}{k} \frac{\partial T}{\partial t} \tag{3.31}$$

It is assumed that there is no axial thermal gradient. The finite element method FEM method is utilized for solving heat conduction equation. Four node isoparametric elements are used for discretizing the problem domain. For the boundary conditions, temperature and flux continuity boundary conditions are assigned to the interface between journal and lubricant.

$$k_L \frac{\partial T_L}{\partial x}\bigg|_{y=r} = k_s \frac{\partial T_J}{\partial x}\bigg|_{y=r} \tag{3.32}$$

$$T_L\big|_{y=r} = T_s\big|_{y=r} \tag{3.33}$$

3.5 Flexible Rotor Model with Thermal Unbalance

The asymmetric heat caused shaft bent at bearing as shown in Figure 3.12. The bow angle is calculated by

$$\beta(t) = \beta_x + i\beta_y = \frac{\xi}{I} \int_0^r \int_0^{2\pi} \int_{-L/2}^{L/2} T(r,\phi,z,t)\, r^2 e^{i\phi}\, dz\, d\phi\, dr \tag{3.34}$$

where ξ and I are thermal expansion coefficient and the second moment of area of the journal, respectively.

The flexible rotor is modeled by Timoshenko beam elements considering shear

deformation. The equation of motion for flexible rotor bearing system can be written as:

$$M_R \ddot{q} + (C_R + \Omega G_R) \dot{q} + K_R q = F_{im} + F_B \qquad (3.35)$$

where M_R , C_R , G_R and K_R are the rotor mass, damping, gyroscopic and stiffness matrices, respectively. F_{im} is the external force vector due to imbalance. F_B is the nonlinear bearing force. For a bent rotor, the total deflection of the rotor can be expressed by

$$q = q_e + q_t \qquad (3.36)$$

where q_e and q_t are deflection due to imbalance and thermal bow, respectively.

Substitution Eq (3.36) into Eq (2.31) yields

$$M_R (\ddot{q}_e + \ddot{q}_t) + (C_R + \Omega G_R)(\dot{q}_e + \dot{q}_t) + K_R q_e = F_{im} + F_B \qquad (3.37)$$

This can also be written as

$$M_R \ddot{q}_e + (C_R + \Omega G_R) \dot{q}_e + K_R q_e = F_{im} + F_B - M_R \ddot{q}_t - (C_R + \Omega G_R) \dot{q}_t \qquad (3.38)$$

If the damping of rotor is negligible, the Eq (3.38) becomes

$$M_R \ddot{q}_e + \Omega G_R \dot{q}_e + K_R q_e = F_{im} + F_B - M_R \ddot{q}_t \qquad (3.39)$$

The last term of the right hand side indicates the equivalent imbalance force due to thermal imbalance at the overhung mass. The equivalent thermal imbalance force, which is similar to initial mechanical imbalance, is written by

$$F_x^t = m_d e_d \omega^2 \cos(\omega t + \varphi) \qquad (3.40)$$

$$F_y^t = m_d e_d \omega^2 \sin(\omega t + \varphi) \qquad (3.41)$$

where e_d and φ are defined by

$$e_d = L_d \sqrt{\beta_y^2 + \beta_x^2} \qquad (3.42)$$

$$\varphi = \tan^{-1}\left(\frac{\beta_y}{\beta_x}\right) \qquad (3.43)$$

L_d is distance between bearing and overhung mass.
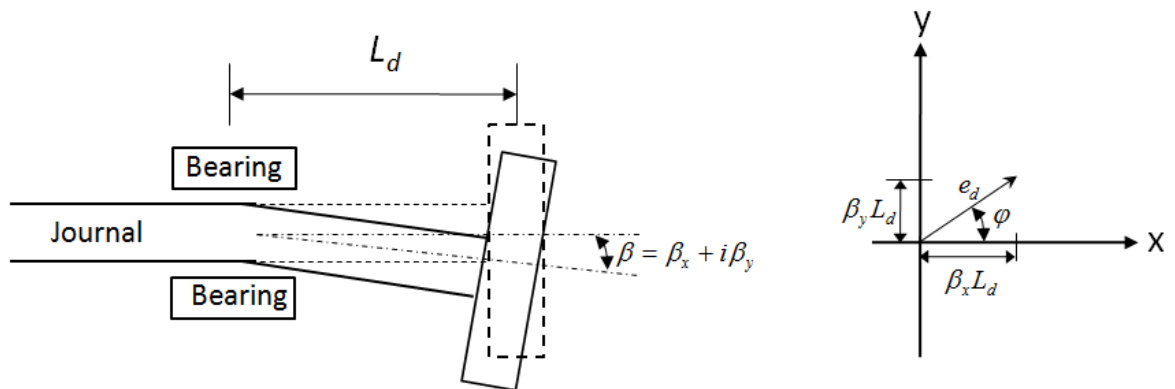
Fig. 3.12 Thermally Induced Bend in a Rotor with an Overhung Mass

3.6. Thermal Mode Analysis Combined Staggered Integration Scheme

3.6.1 Thermal Mode Analysis [47]

In thermal problems, as in structural mechanics, a time-varying solution may be obtained by the modal method. If material properties are not temperature-dependent, and the solution is dominated by a few of the lowest eigenmodes and is needed over a long time span, then the modal method is favored. This greatly reduces the computation time without sacrificing significant accuracy.

The equations to be solved have the form

$$[C]\dot{T} + [K]T = F \tag{3.44}$$

The procedure is very similar to that used for structural dynamics. It is outlined as follows. One first considers the eigenproblem

$$([K] - \lambda[C])T = 0 \tag{3.45}$$

If each eigenvector $\{T\}$ is normalized with respect to [C], that is, if $\{T\}^T[C]\{T\} = 1$, then

$$[\phi]^T[C][\phi] = [I] \tag{3.46}$$

$$[\phi]^T[K][\phi] = [\lambda] \tag{3.47}$$

where $[\phi]$ is the modal matrix; that is, a matrix whose columns are normalized eigenvectors $\{T\}$, $[I]$ is a unit matrix, and $[\lambda]$ is the diagonal eigenvalue matrix. Nodal temperatures are transformed to generalized temperatures $\{Z\}$ by

$$T = [\phi]\{Z\} \tag{3.48}$$

where the Z in $\{Z\}$ state the proportion of each eigenvector in the transformation. Using this modal approach, we obtained uncoupled equations.

$$\{\dot{Z}\} + [\lambda]\{Z\} = [\phi]^T F \tag{3.49}$$

To verify the thermal mode approach, a simple heat conduction problem is solved as shown in Figure 3.13. Temperature distribution from the thermal mode approach is similar to solutions of original equations. As mode number used in the simulation increases, the simulation time significantly increases shown in Figure 3.14.

(a)

(b)

(c)

(d)
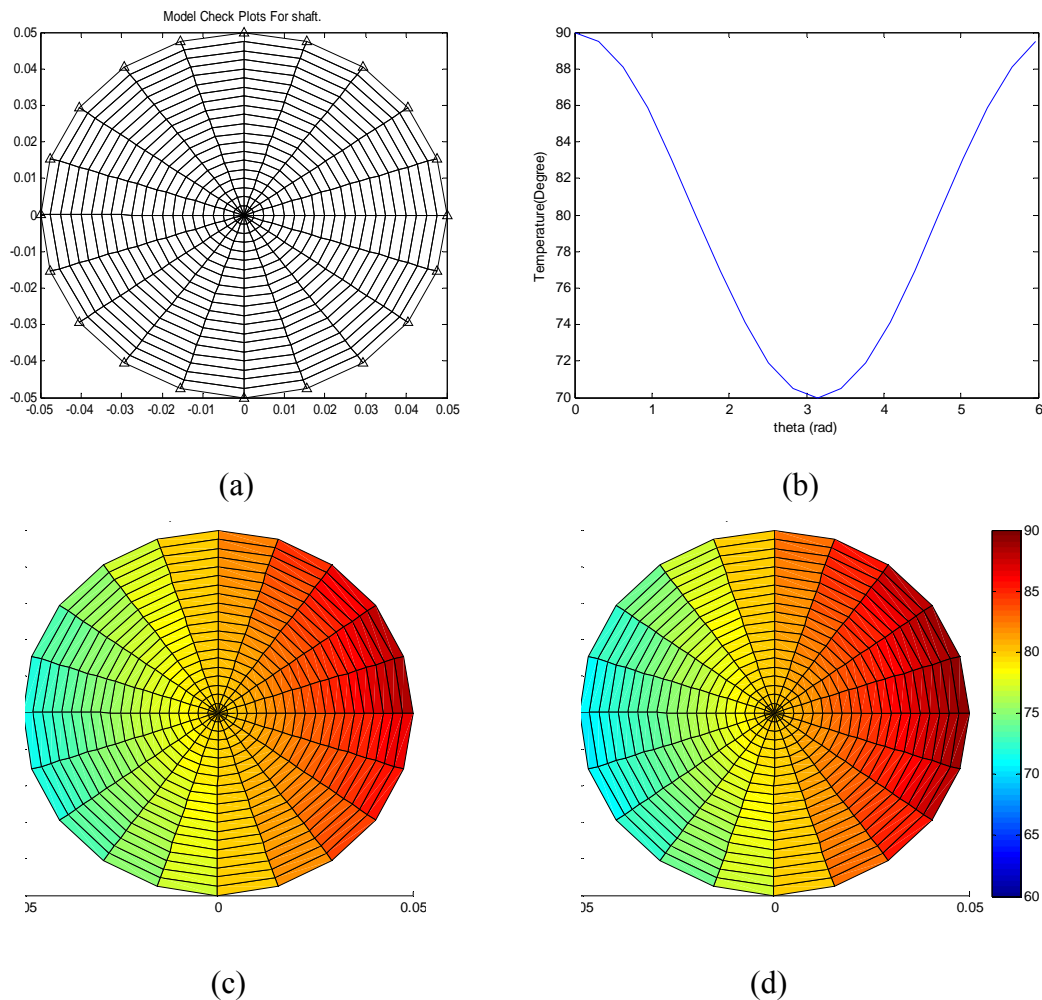
Fig. 3.13 Verification of Thermal Mode Approach; (a) Computation Domain, (b) Boundary Condition, (c) Transient Results, and (d) Steady State Solution
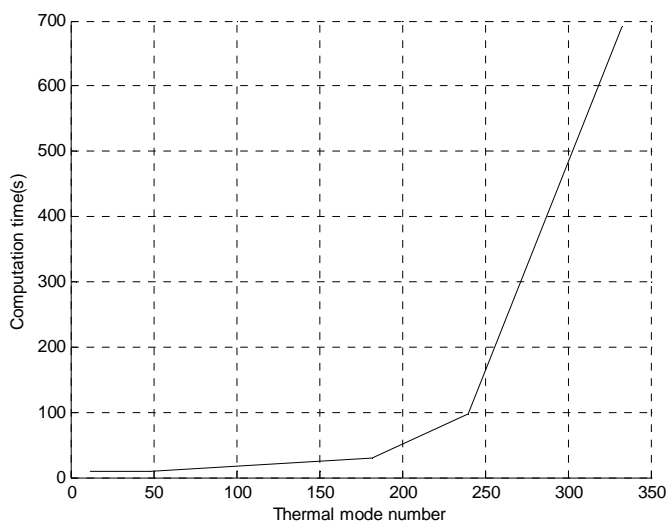
Fig. 3.14 Computation Time vs Mode Number

3.6.2 Staggered Integration Scheme

The flowchart shown in Figure 3.15 is for calculating temperature difference of journal for a given orbit. At the beginning of the program, the uniform journal temperature distribution and constant viscosity are assumed and those values are updated during iteration. During one revolution, the journal temperature is calculated at the equally spaced 20 points on the orbit, and evaluated the averaged journal temperature after one revolution. Convergence criterion of iterated solution is 0.001.

Figure 3.16 shows another flowchart for simulating Morton Effect instability including rotordynamic analysis. The analysis code calculates the thermal induced imbalance and solves rotordynamic problem during iteration. The simulation for evaluating thermal gradient of the journal solves the Reynolds, energy equation, heat conduction equation. This is a very time consuming work even though thermal mode

approach reduces computation time a little bit. In order to significantly reduce computation time, staggering method is applied to simulation. A staggered integration shown in Figure 3.17 scheme is proposed to greatly increase the computational efficiency without losing the accuracy of solutions for a dynamic model, which has local nonlinearities and two types of solutions with different time constants. Staggered integration scheme whose cycle is 100 revolutions consists of two stages. At the first stage (1) which is from 1 to 10 revolutions, the Reynolds, energy, heat conduction, and EOM for rotor are solved. At the ninth revolutions, the temperature and viscosity data saved and applied is to the next stage. The second stage (2) is from 11 to 100 revolutions, the heat conduction equation is only solved. After the completion of second stage, the bow angle is calculated and is used as thermal imbalance defined by Eqs (3.40)-(41). This process can be used alternately several times to obtain extended simulation results.
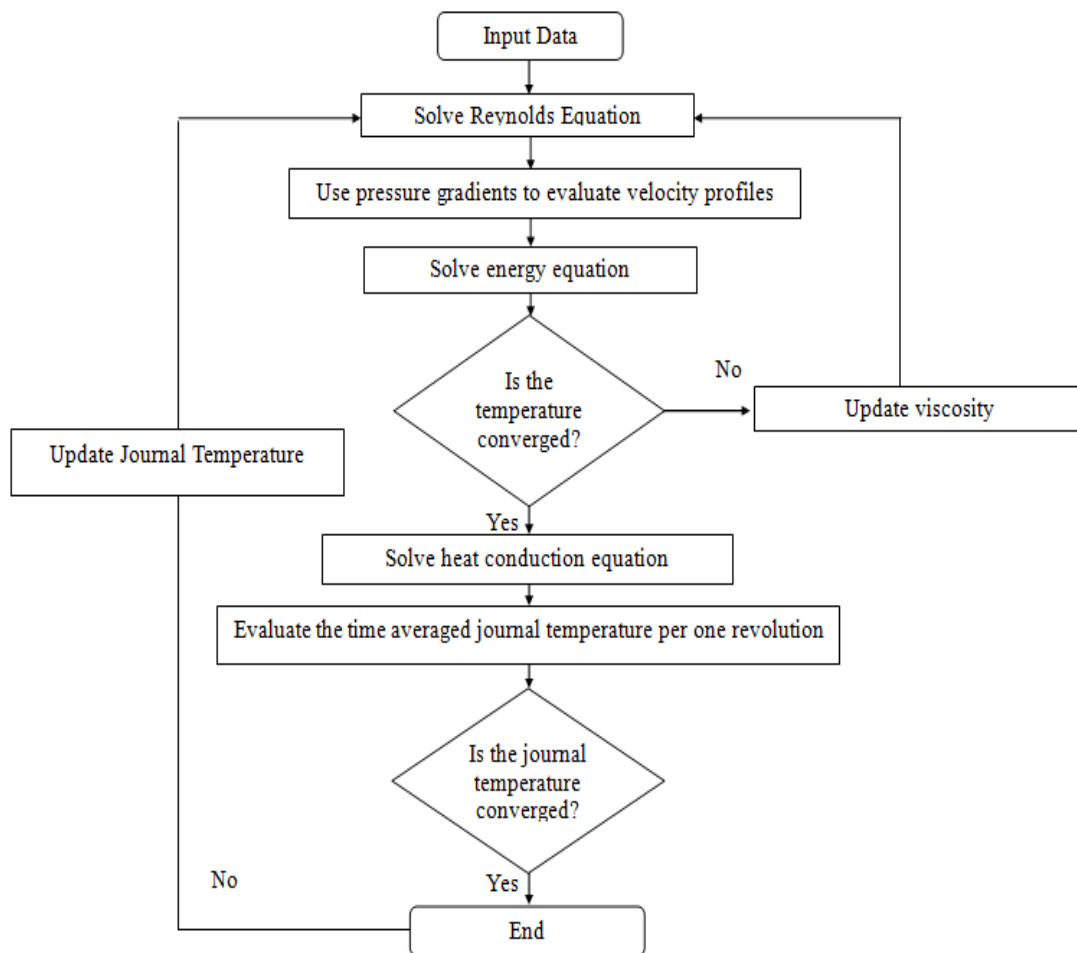
Fig. 3.15 Flowchart for Calculating Temperature Difference of Journal for a Given Orbit
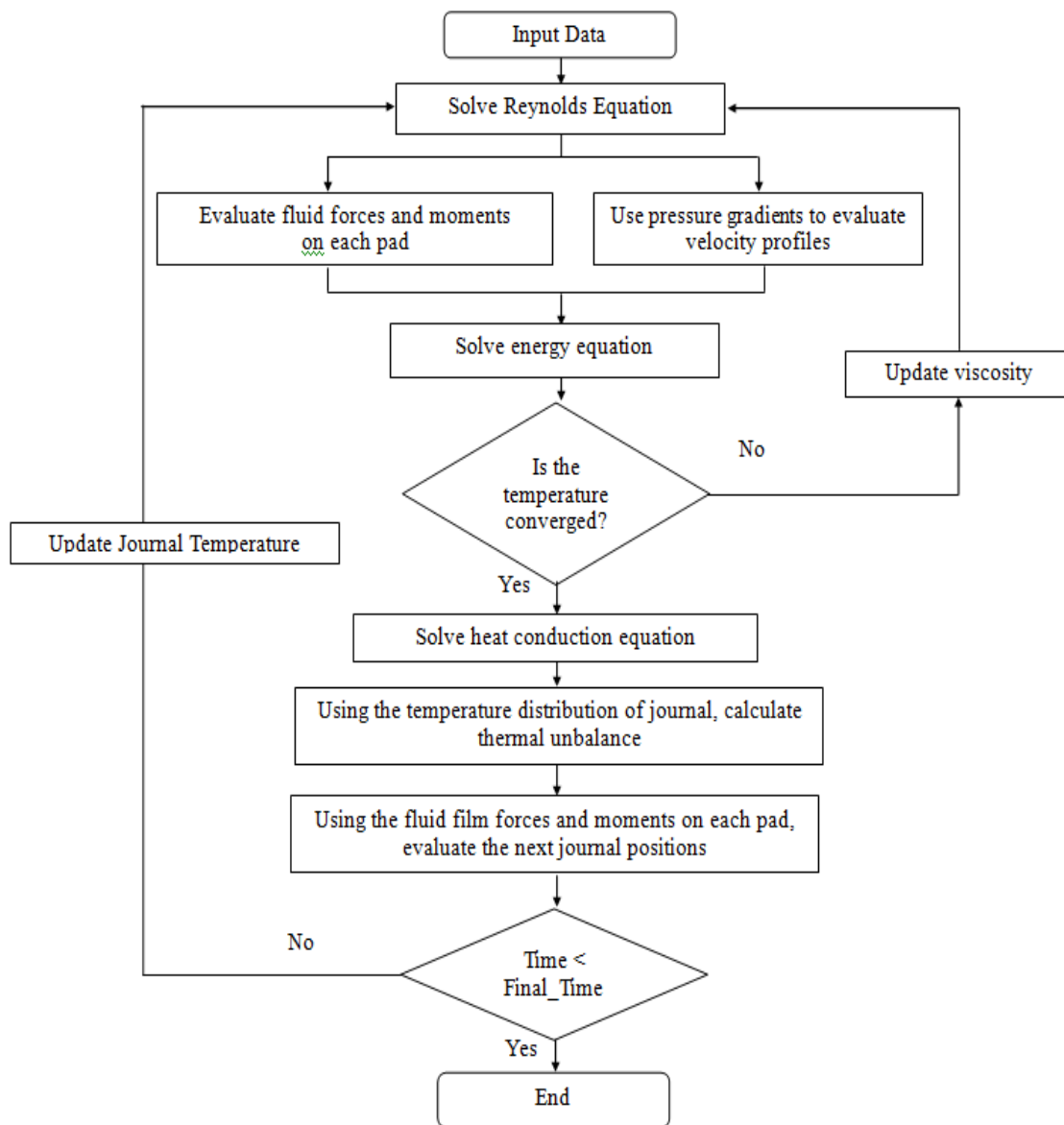
Fig. 3.16 Flowchart for Full Time Transient Analysis
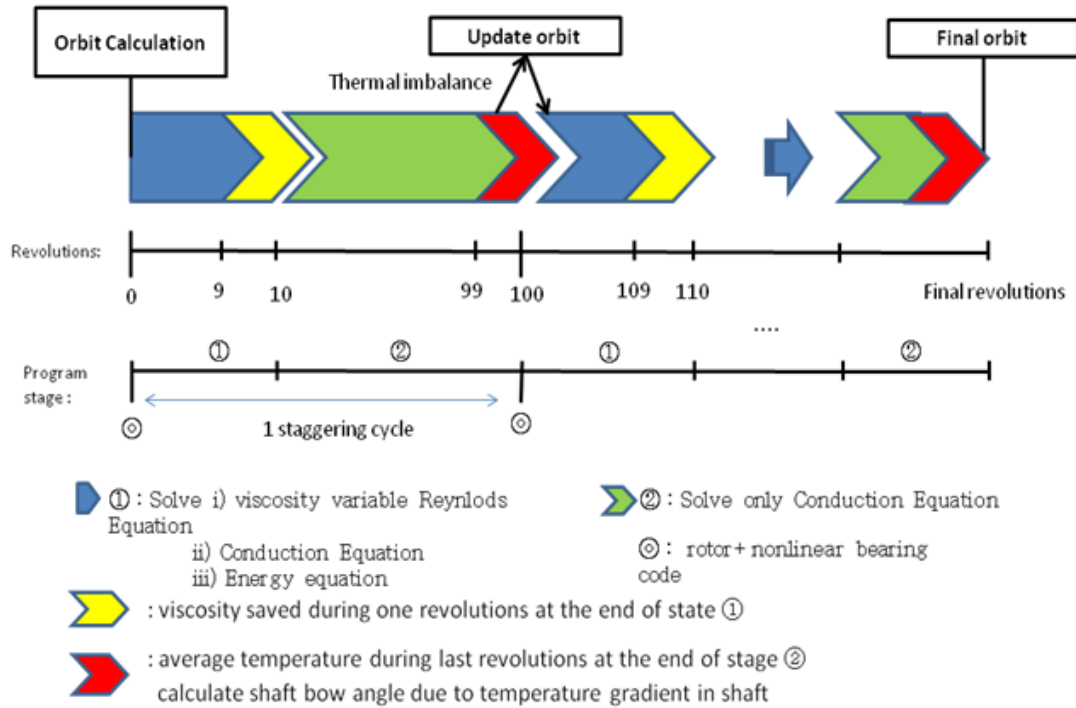
Fig. 3.17 Staggered Integration Scheme.

3.7 Simulation Results and Discussions

3.7.1 Verification for Morton Effect Model

Plain journal bearing: In order to verify current approach, the temperature difference of journal for plain journal bearing is compared with reference [16]. The plain journal bearing has two circular two-inlet and the simulation parameters are listed in Table 3.3. The static eccentricity ratio (ε_0) and attitude angle (ψ_0) are 0.7 and 38º. The spin speed is 10,000 rpm (1047 *rad/s*). Figure 3.18 shows the comparison between reference and current approach. As the forward whirl radius ratio increases, the temperature difference also increases. But the relationship between whirl radius ratio and temperature difference is not linear. The temperature difference resulted from current approach is slightly higher than that of reference. This is due to 1) insulation boundary condition at the bearing side, 2) ignoring axial thermal gradient. The temperature distribution of journal surface is sinusoidal, and phage lag is identical to reference. The pure sinusoidal temperature on the surface of journal indicated that temperature across journal varies linearly.

Tilting pad journal bearing: The open literature does not provide any results for predicted or measured temperature difference across the journal, for tilting pad bearings. The available data in the references shows only the unstable spin speed due to thermal gradient on the journal to demonstrate the journal asymmetric heating for titling pad journal application, four pad titling pad journal bearing is considered and the geometric and material data shown in Table 3.4 corresponds to the experimental bearing of Fillon et al. [46].

Table 3.3 Simulation Parameters

	Journal	Lubricant	Air		
Mass Density (kg/m^3)	7850	850	1.2	Viscosity (Pas)	0.0183
Thermal Conductivity (W/mK)	50	0.15	0.025	Viscosity Exponent ($1/K$)	0.0295
Specific Heat Capacity (J/kgK)	460	2000	1000	Inlet Temperature (^oC)	50
Radius (m)	0.1			Supply Pressure (MPa)	1.2, 1.5
Length (m)	0.45			Bearing Clearance (μm)	72.6
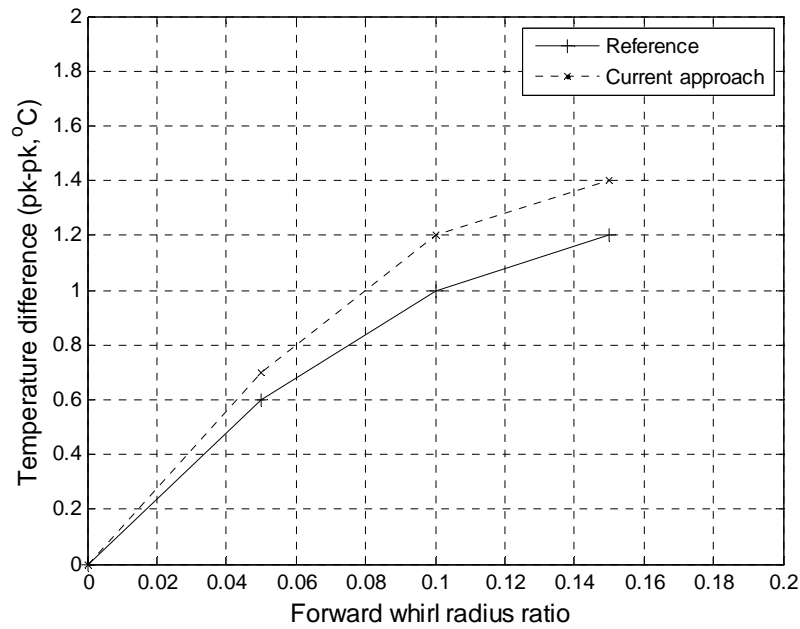
(a)

Fig. 3.18 Journal Surface Temperature Comparison; (a) ΔT (pk-pk) vs ε_f,

(b) Temperature Distribution on the Journal Surface at z/L=0 and (c) Reference

Results
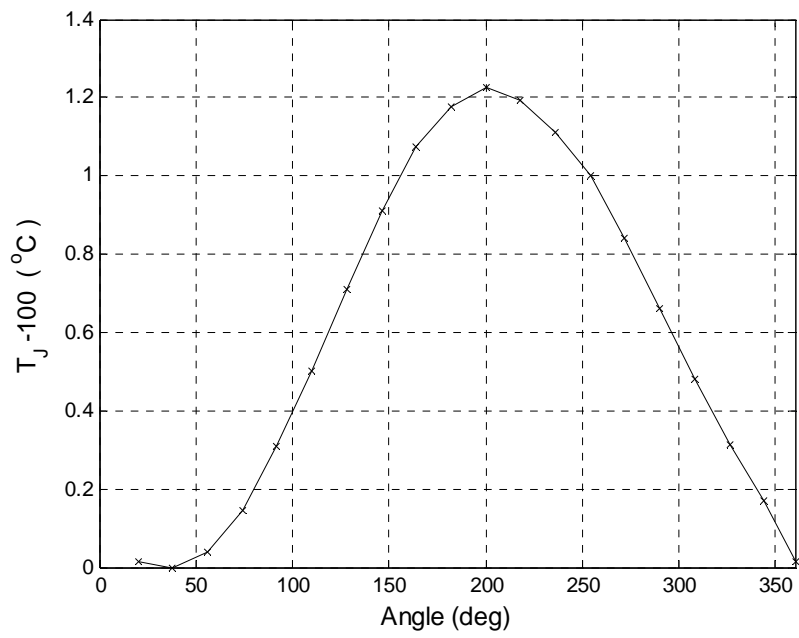
(b)
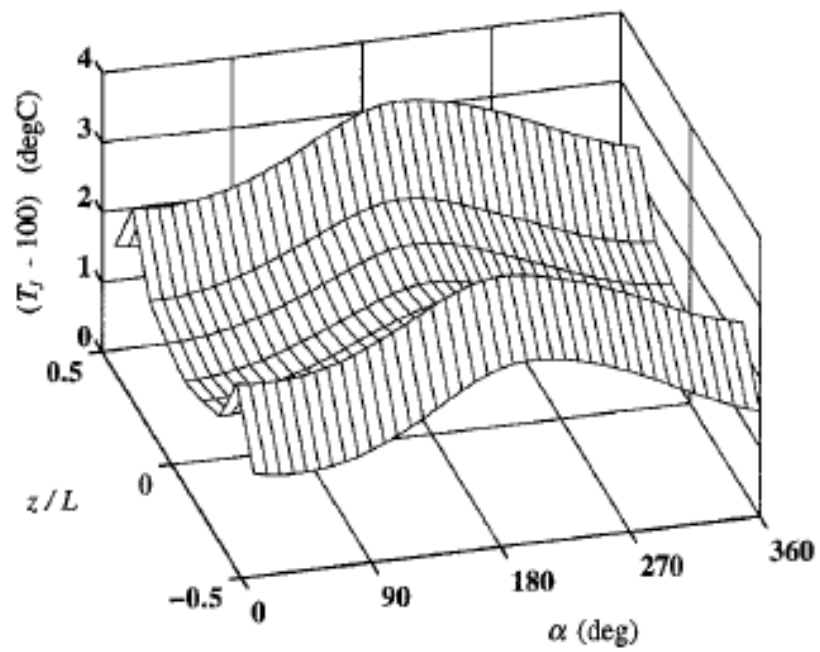
(c)

Fig. 3.18 Continued

First, consider a given circular (elliptic) orbit, which produces the journal temperature distribution shown in Figure 3.19. As the number of revolutions increases, the temperature in the shaft approaches steady value. As we expected, there is a thermal gradient along the circumferential direction. We observed in simulation results that temperature across journal varies linearly shown in Figure 3.20 and that as the radius of orbit increases, the temperature difference also increases but it is not linearly proportional to the orbit size shown in Figure 3.21. Figure 3.22 shows the temperature distribution of journal for some forward whirl cases.

Table 3.4 Bearing Geometry and Lubricant Properties

Parameter	Value	Parameter	Value
Pad Parameters		Lubricant Parameters	
Journal Radius (m)	0.0498	Supply Pressure (MPa)	0.5
Axial Pad Length (m)	0.7	Supply Temperature (^oC)	40
Pad Thickness (m)	0.02	Viscosity (cP)	27.7
Radial Pad Clearance (μm)	68	Viscosity Exponent ($1/^o C$)	0.034
Angular Dimension of Pad (deg)	75	Lubricant Density (kg/m^3)	860
Pivot Angles of Pads (deg)	45, 135, 225, 315	Specific Heat Capacity (J/kgK)	2000
Preload Factor	0.68		
Offset	0.5		
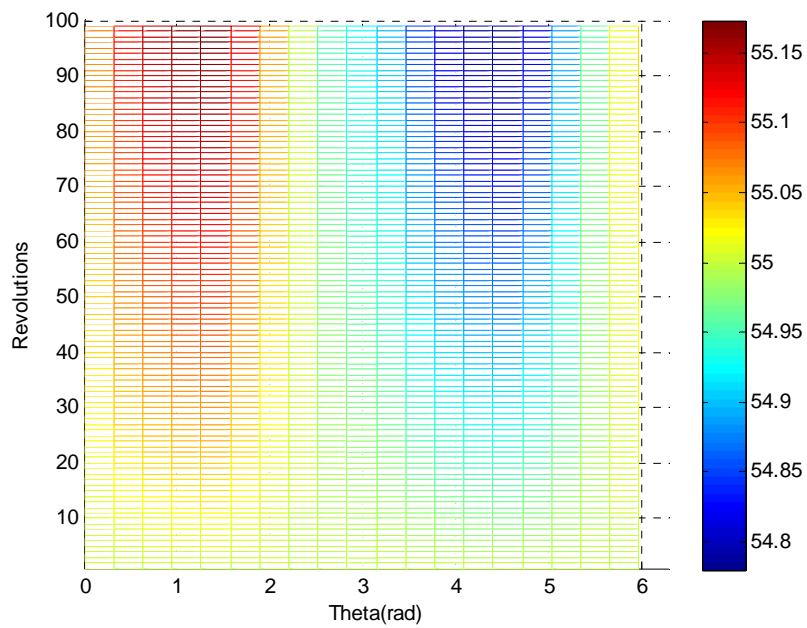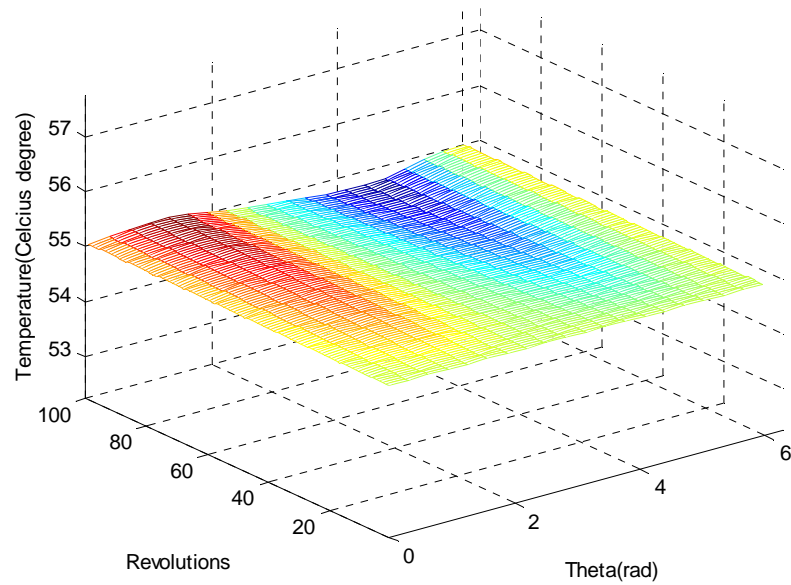
(a)

Fig. 3.19 Temperature Distribution vs Theta vs Revolutions; Forward Whirl

Radius ratio (a) 0.05, (b) 0.15 after 100 Revolutions.
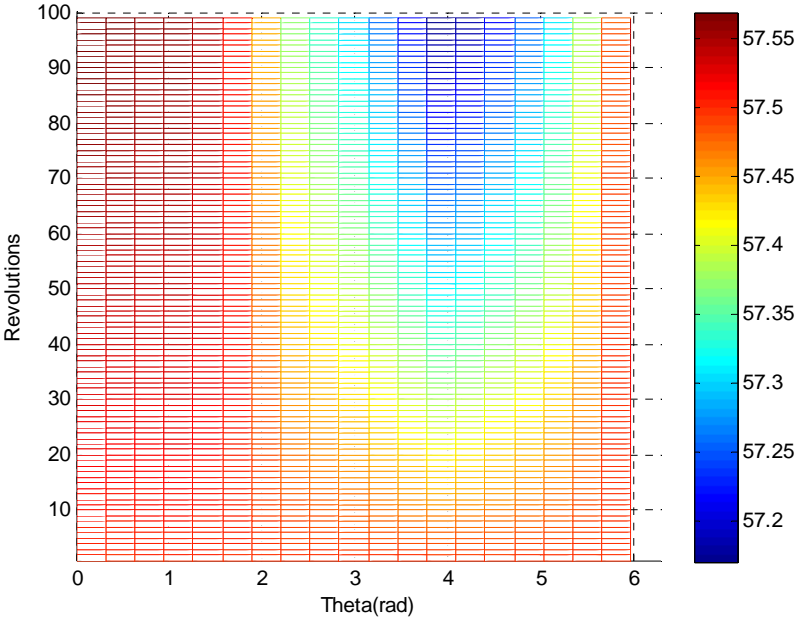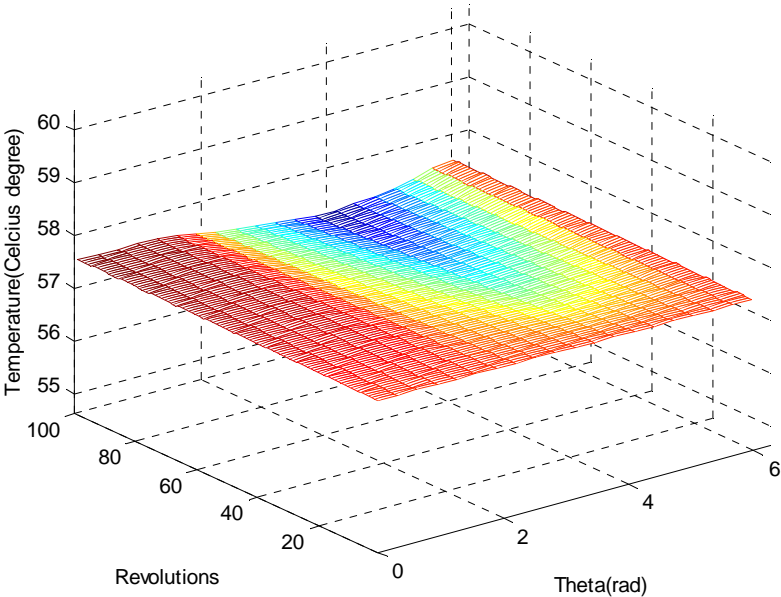
(b)

Fig. 3.19 Continued
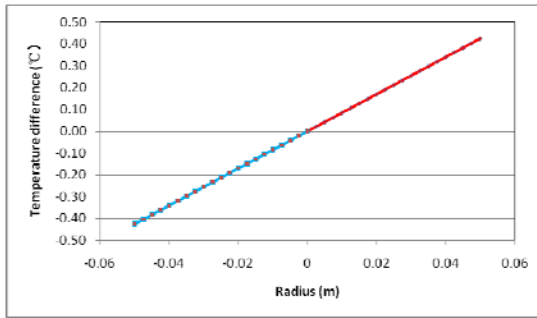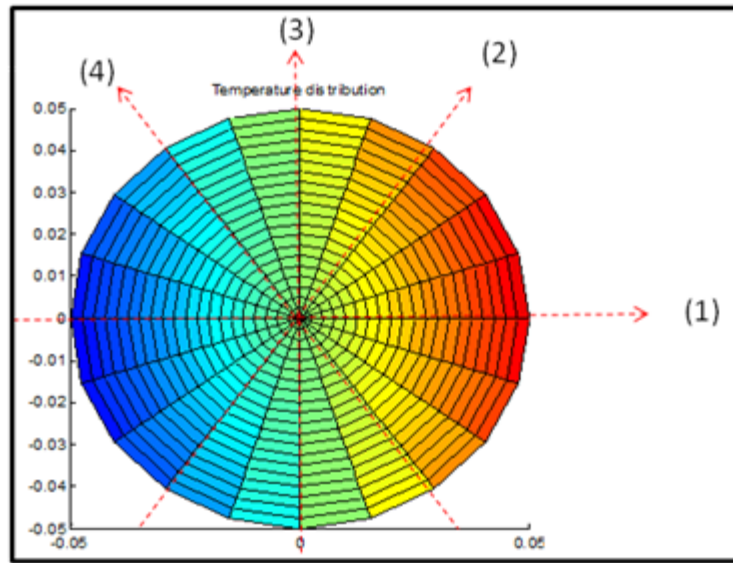
(1)
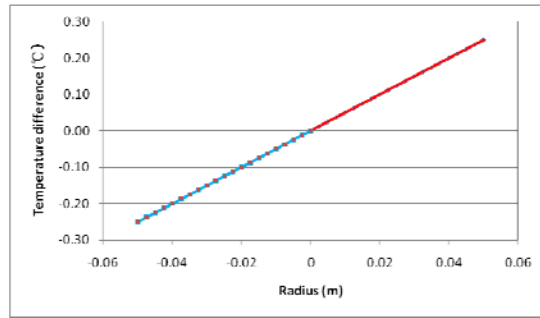
(2)
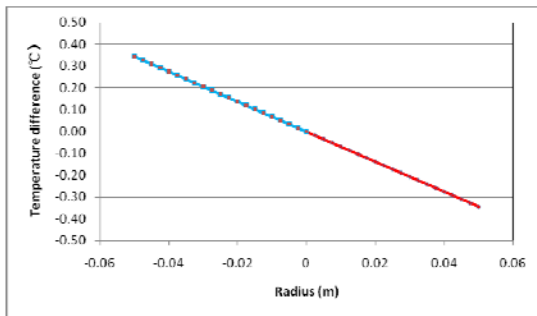
(3)
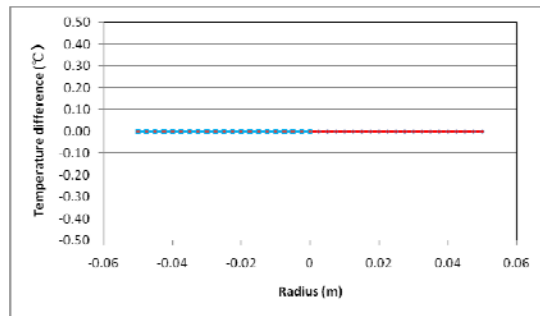
(4)

Fig. 3.20 Temperature Variation across Journal
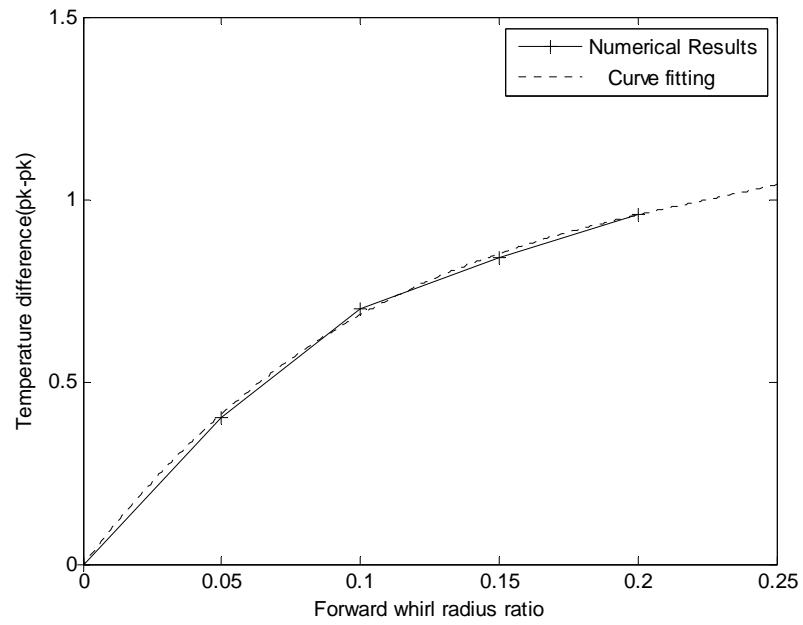
Fig. 3.21 Temperature Difference vs Forward Whirl Radius Ratio

(a)   (b)
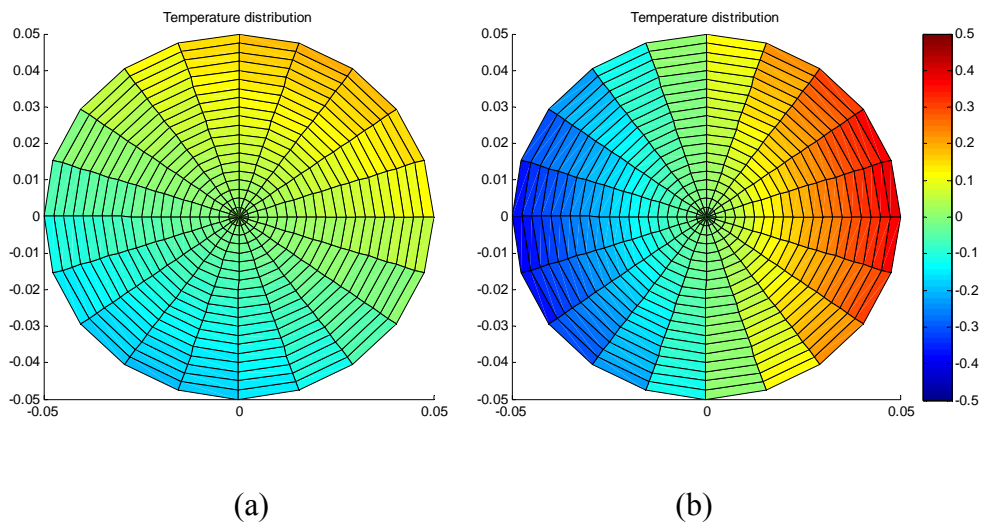
Fig. 3.22 Temperature Distribution of the Journal; Forward Whirl Radius Ratio (a)

0.05, (b) 0.15

The temperature difference, moments, and phase lag between high spot and hot spot summarized in Table 3.5 depending on forward whirl radius ratio. According to Keogh and Morton [14], the phase lag is caused by convective heat transfer within lubricant film. As the orbit size increase, the phase lag approaches to certain values.

An elliptic orbit can be decomposed forward circular orbit and backward circular orbit. We expected that temperature difference for elliptic orbit case is equal to sum of the temperature difference for each forward and backward. However, simulation results shown in the Figure 3.23 and Table 3.6 indicate that the temperature difference for elliptic orbit cannot be represented by the sum of temperature difference of forward and backward whirl. It means that in general the moments due to the thermal imbalance for elliptic motion may not equal the sum of moments from forward and backward whirl motion.

Table 3.5 Simulation Results; Temperature Difference, Phase Lag, and Moments for Steady State

Forward Whirl Radius Ratio	0.05	0.1	0.15	0.2
Temperature Difference (^oC)	0.4	0.7	0.85	0.95
Phase Lag	90	60	30	30
Mx (Nm)	0	62	93	104
My(Nm)	43	45	0	0
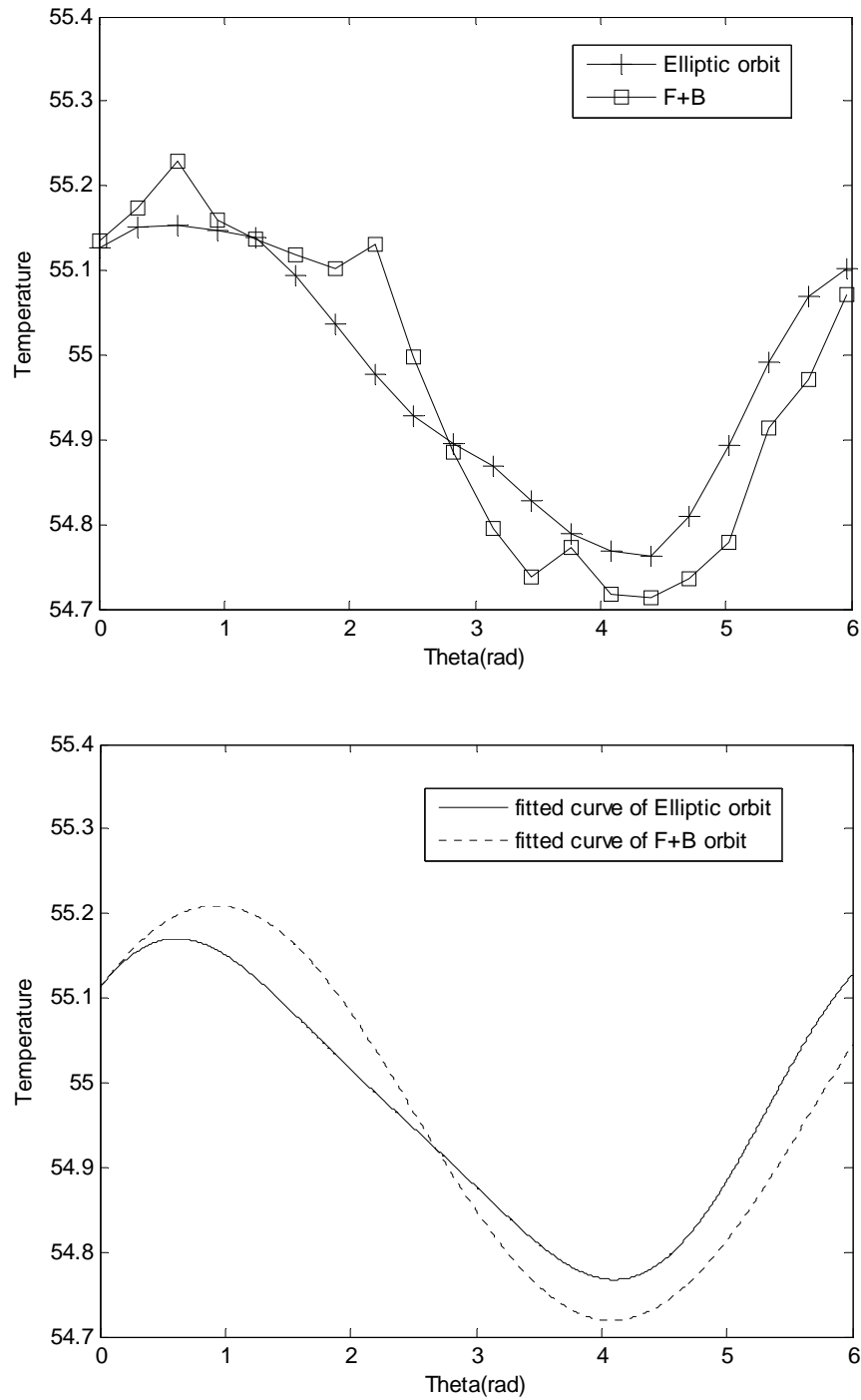
Fig. 3.23 Temperature Distribution for Elliptic Motion and

Forward(0.1)+Backward(0.05)

To verify the staggering method, the full simulation results are compared to results from staggering method. The comparison shown in the Figure 3.24 and Figure 3.25 shows that there is small error, less than 1%. In addition, the computation time significantly reduced from 6 hr to 1hr for 100 rev.

Table 3.6 Temperature difference and Moments after 200 rev

Whirl type	Forward(0.1) + Backward(0.05)	Elliptic
Temperature Difference (^oC)	0.5	0.4
Moment, Mx(Nm)	33	25
Moment, My(Nm)	42	35
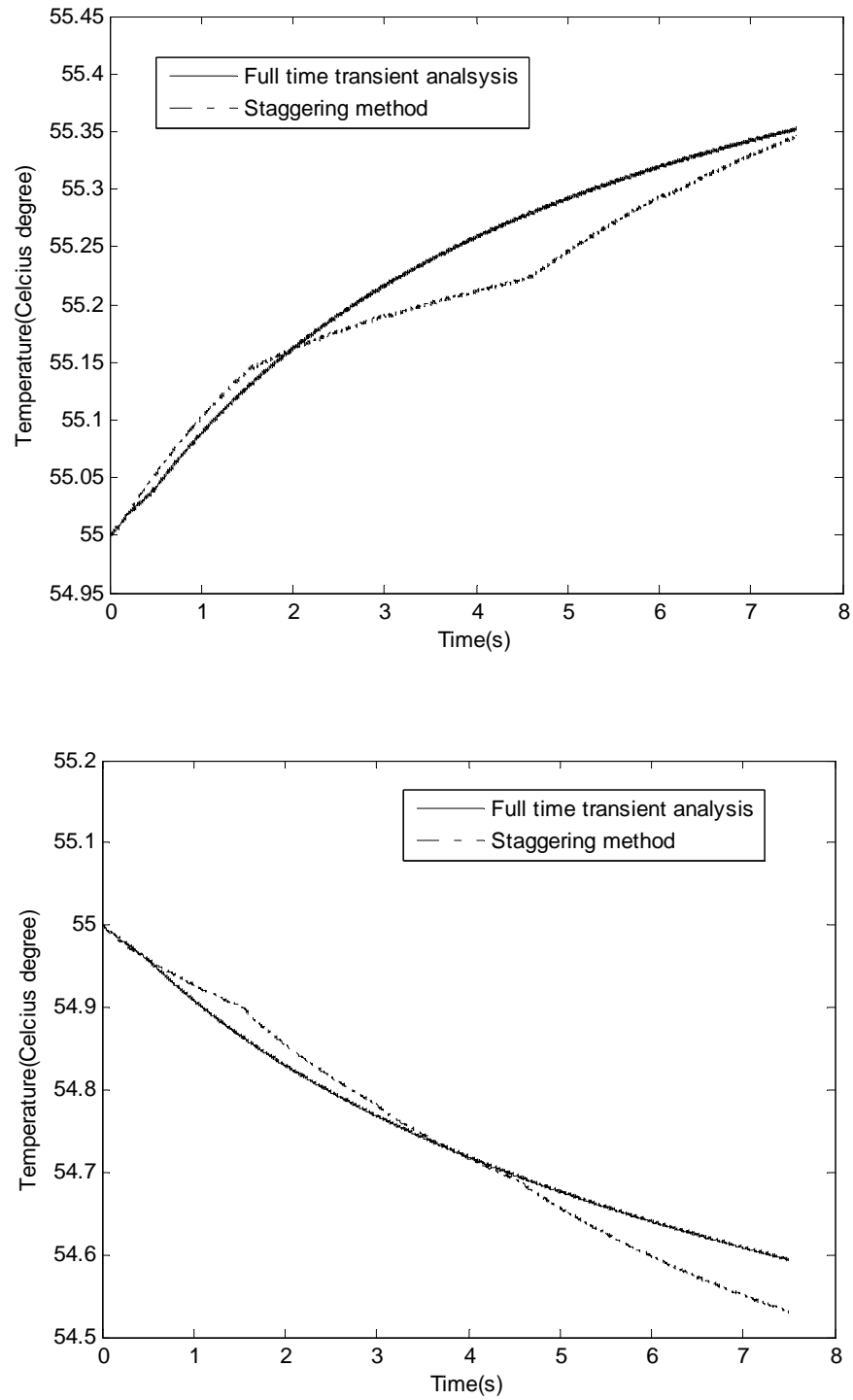
Fig. 3.24 Comparison between Staggering Method and Full Simulation

Temperature distribution on the shaft surface

Temperature distribution on the shaft surface
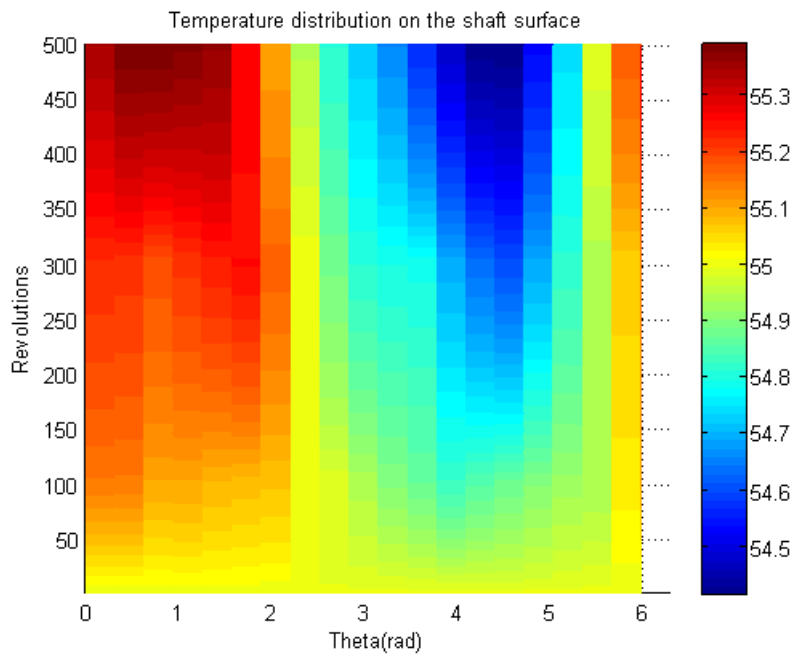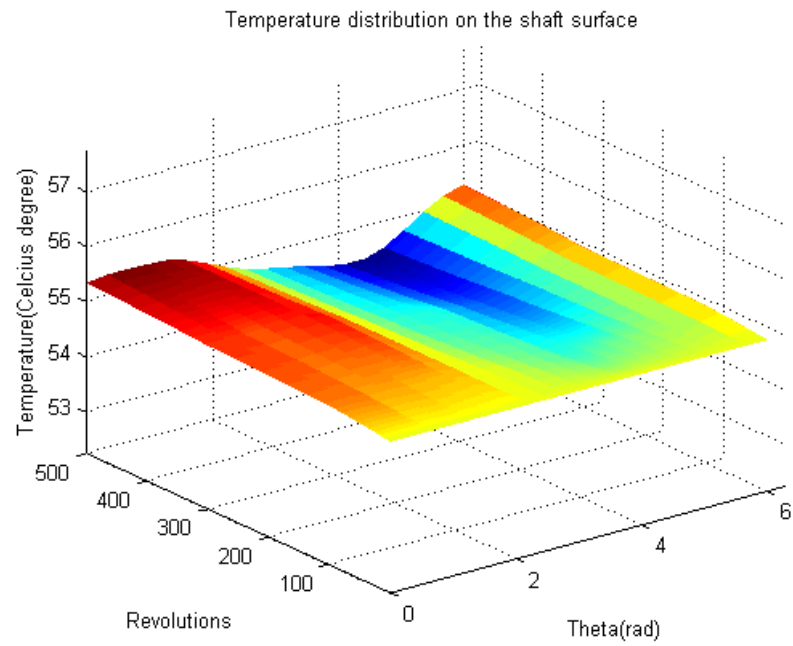
(a)

Fig. 3.25 Temperature Distribution (a) Full simulation (b) Staggering Method
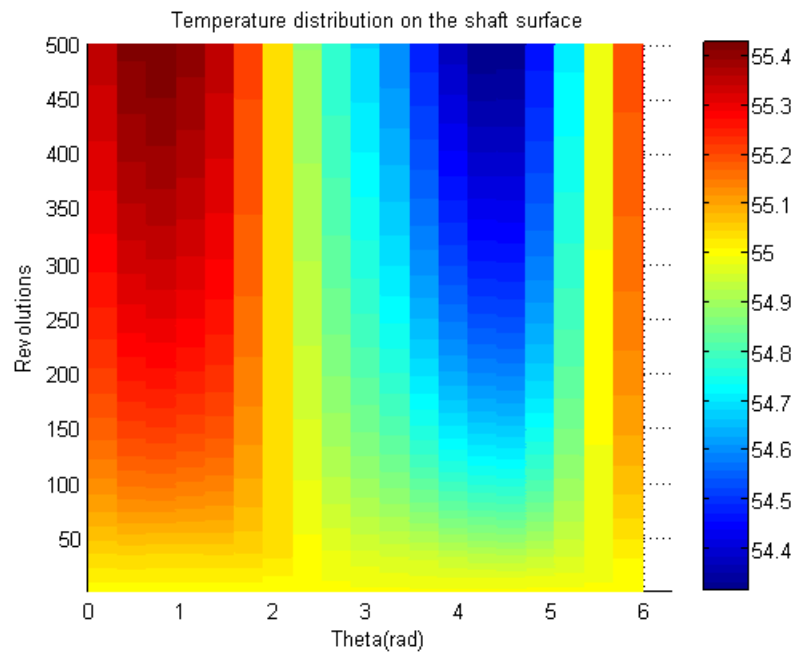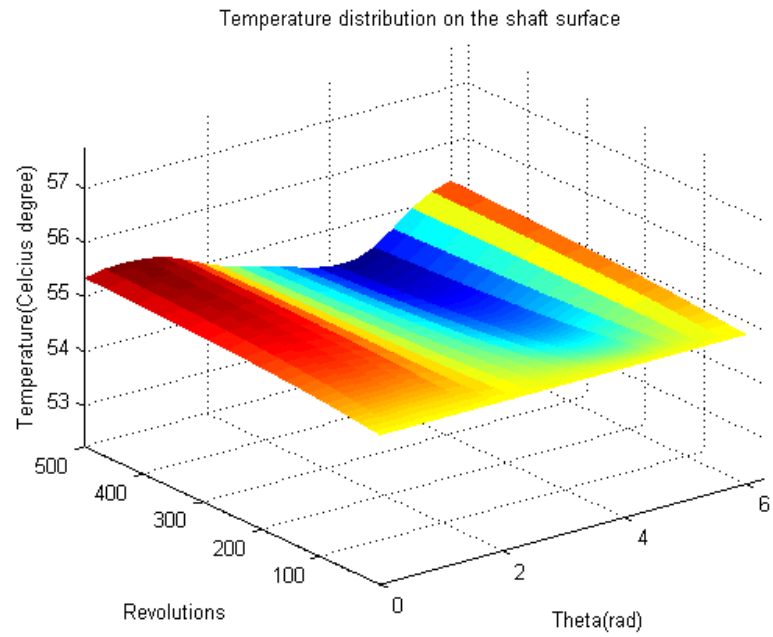
(b)

Fig. 3.25 Continued

The synchronous stabilty of the rotor-bearing system is checked by comparing the using the developed code with the results of de Jongh and van der Hoeven[48]. According to their experiment, during operation, these compressors exhibited large vibration levels above 7,200 rpm and the machines had to be shut down. The rotor bearing system consists of large overhung mass and two tilt pad jorunal bearing. The FEM model are given in Figure 3.26. The bearing data at the non-drive end (NDE) near the overhung mass is listed in Table 3.7 and Figure 3.27 shows the experiment results of de Jongh. The Morton effect simulation is only applied on the bearing near the overhung mass.
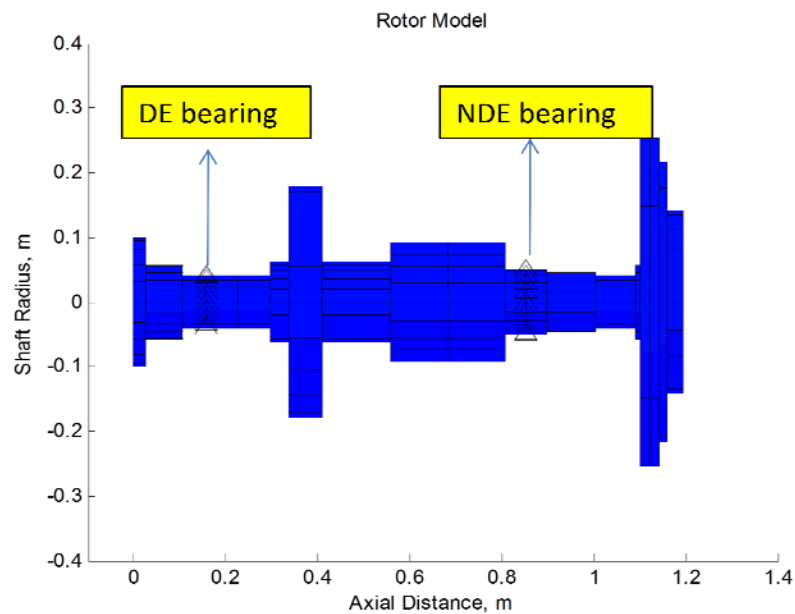
DE: Drive end, NDE: Non-drive end

Fig. 3.26 FEM Rotor Model

Table 3.7 Input Parameters

Parameter	Value	Parameter	Value
Pad parameters		Lubricant Parameters	
Axial Pad Length (m)	0.0508	Supply Pressure (MPa)	0.132
Pad Thickness (m)	0.0127	Supply Temperature (^oC)	50
Radial Pad Clearance (μm)	178	Viscosity (cP)	20.3
Angular Dimension of Pad (deg)	56	Viscosity Exponent ($1/^oC$)	0.031
Pivot Angles of Pads (deg)	54, 126, 198, 270, 342	Lubricant Density (kg/m^3)	860
Preload Factor	0.5	Specific Heat Capacity (J/kgK)	2000
Offset	0.5		
Journal/Bearing Parameters			
Radius of Journal (m)	0.0508		
Bearing Load (N)	2180		
Overhang Mass (kg)	113		
Overhang Distance (m)	0.27		
Initial Mechanical Unbalance ($kg \cdot mm$)	0.27		

The spin speeds are selected as 7200, 8000, and 8500 rpm. First, we simulated the transient analysis without considering asymmetric heating on the shaft. For three spin rpm, there is no large vibration level increase. However, with considering asymmetric heating the simulation results shown in Figure 3.28 and Figure 3.29 indicates the large

vibration level change above 7200 rpm. The vibration level of simulation results is less than that of experiment by 20%. However, the simulation results clearly show that the increasing vibration level due to asymmetric heating of journal. In addition, it is worth to note that the orbit starts to increase until it reaches its maximum value, and then the orbit begins to decreases by the certain level which is greater than the orbit without including asymmetric heating. During the simulation, the orbit oscillates between maximum and minimum level. The gradually increasing temperature difference of journal leads to big vibration, which in turn changes the bearing oil temperature, which affects the temperature distribution of journal. This chain of events shown in Figure 3.30 is a limit cycle which is stable oscillation of the envelope of the amplitude of synchronous vibration.
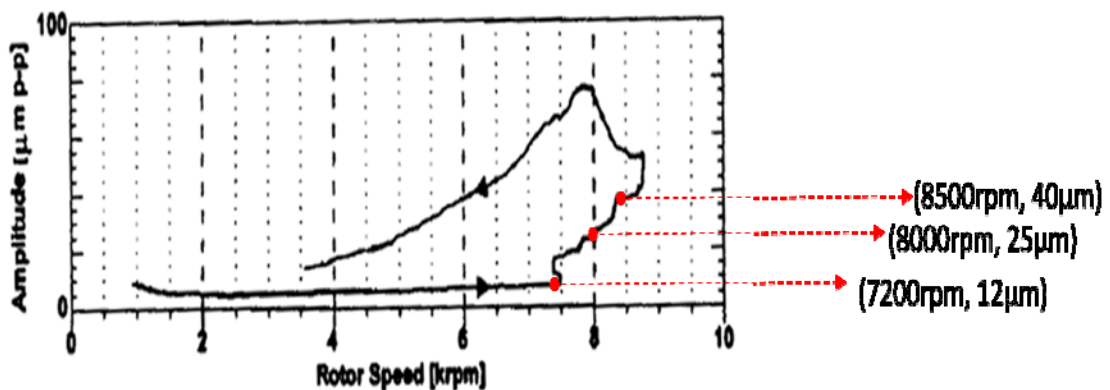
Fig. 3.27 Test Results by de Jongh et al.
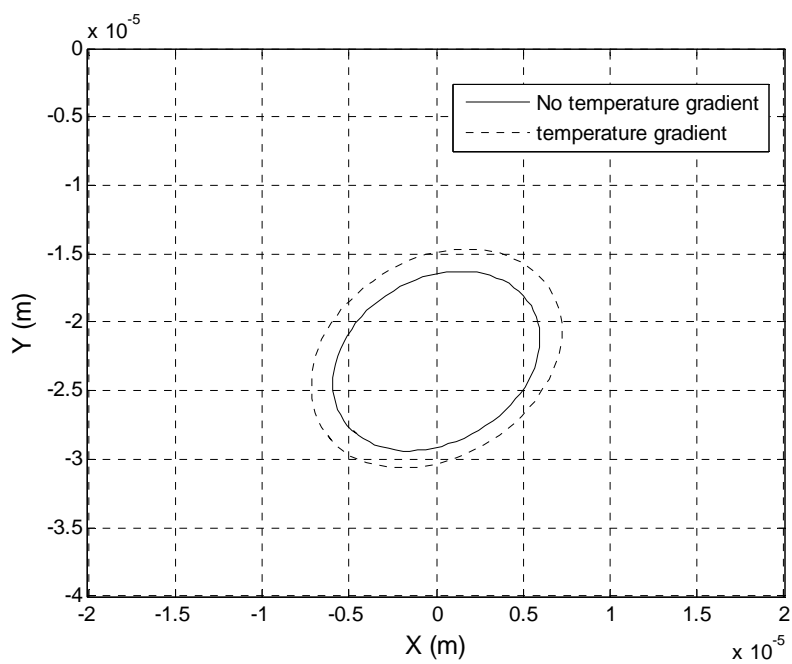
(a)
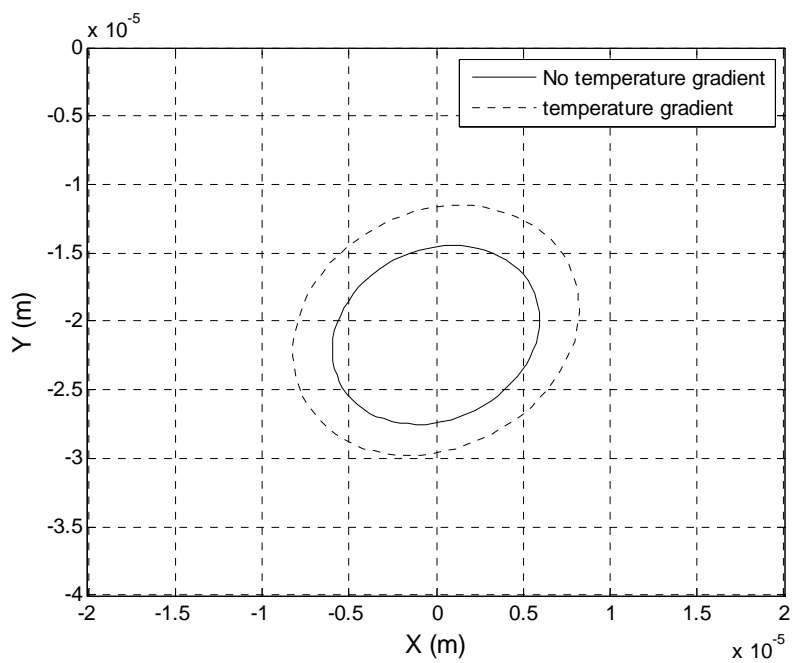
(b)

Fig. 3.28 Morton Effect Simulation Results; (a) 7200, (b) 8000, and (c) 8500 rpm
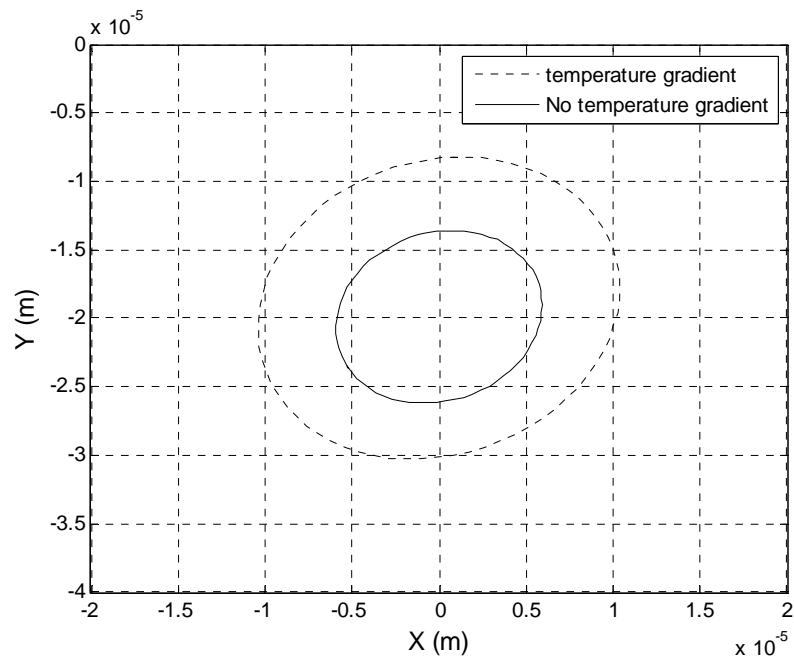
(c)

Fig. 3.28 Continued
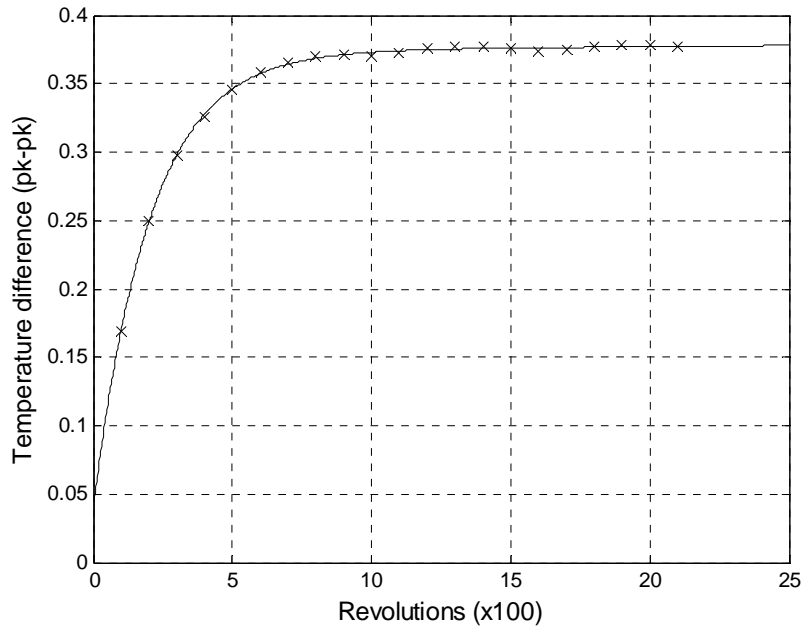
(a)
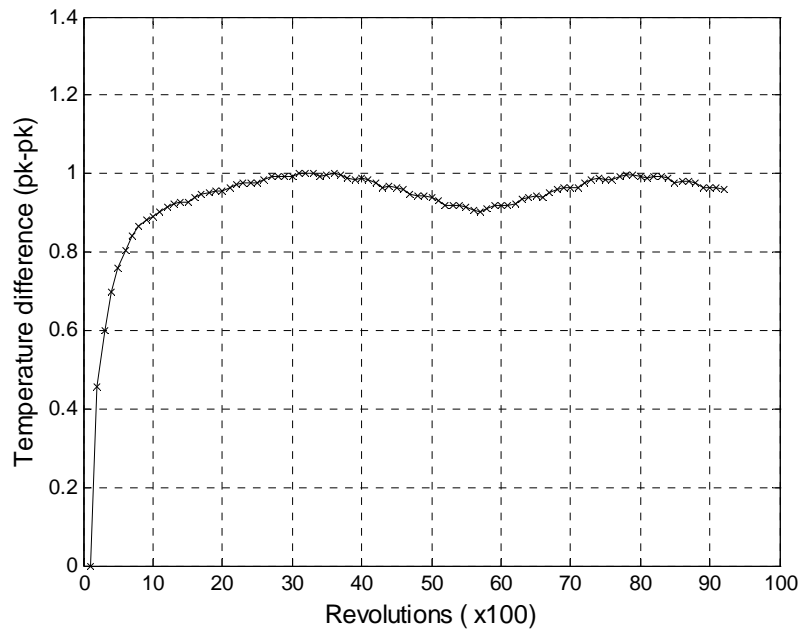
(b)

Fig. 3.29 Temperature Difference vs Revolutions; (a) 7200, (b) 8000 rpm, and (c)

8500 rpm
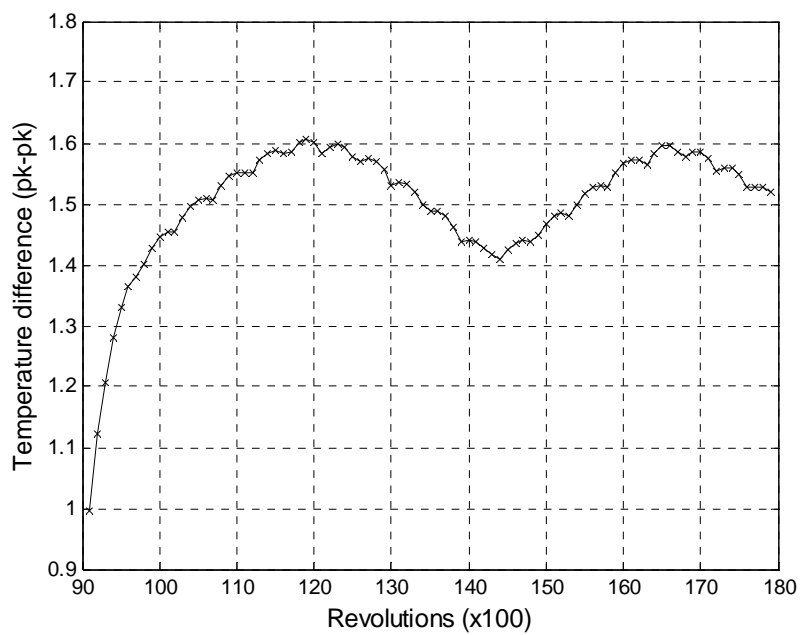
(c)

Fig. 3.29 Continued
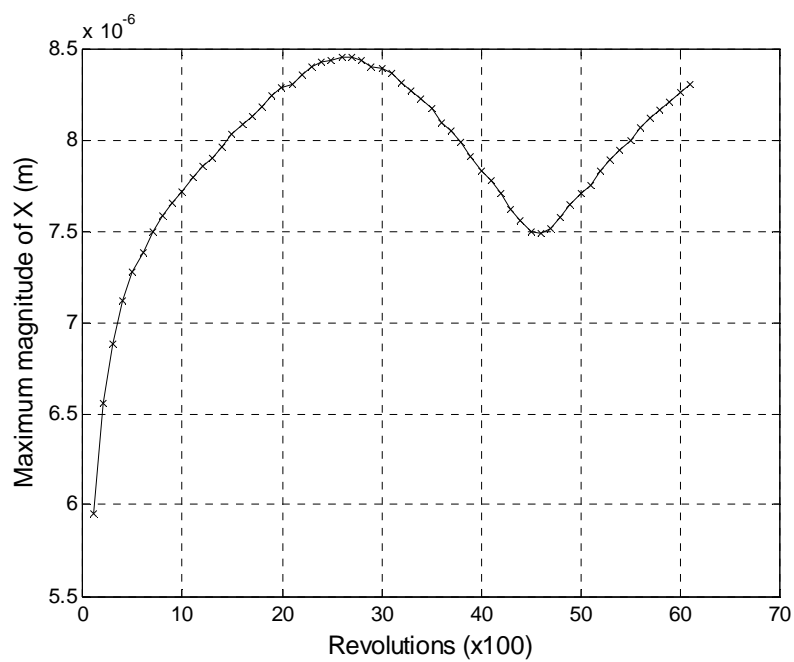
(a)
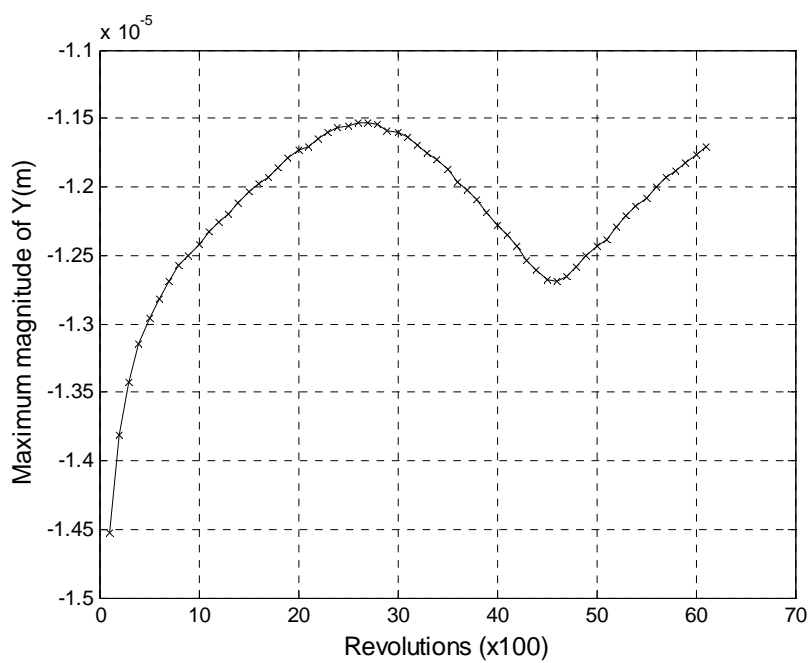
(b)

Fig. 3.30 Limit Cycle at 8000 rpm; (a) Maximum Magnitude of X, (b) Maximum

Magnitude of Y, and (c) Orbit Plot
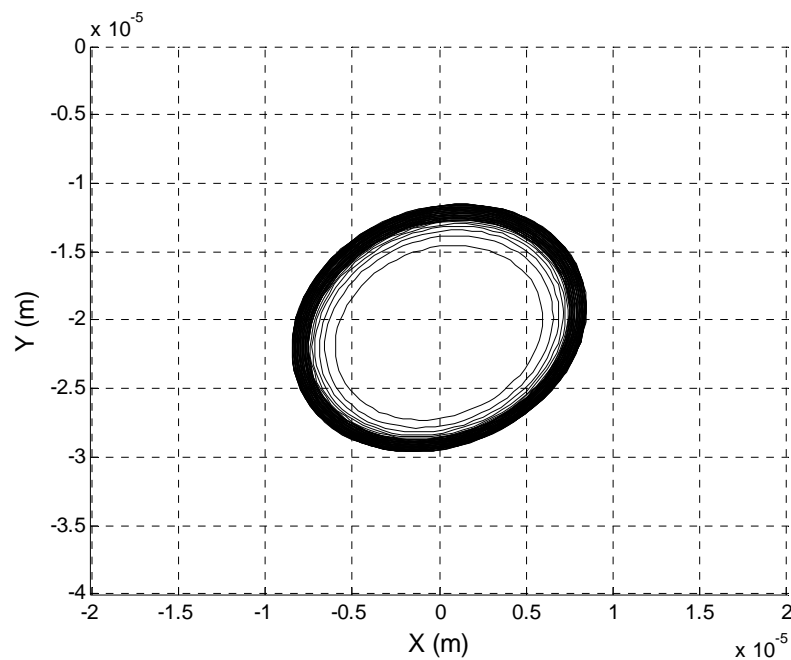
(c)

Fig. 3.30 Continued

In order to reduce the synchronous instability, some methods such as redesign bearing or shaft and change viscosity properties are suggested. In current study, the two methods are adapted to mitigate the Morton effect; i) reduce bearing clearance and ii) change lubrication viscosity. Figure 3.31 shows the effect of these methods. Even though the reducing bearing clearance induces the higher viscous shear stress and larger temperature difference, the increasing stiffness and damping result in a machine less sensitive to overhung imbalance. However, the effect of reducing bearing clearance is not significant in this case. Another method, the change of lubricant, the lower viscosity reduces the lower viscous shear, and thus less asymmetric heating. Therefore, the vibration level is decreased by about 50%.
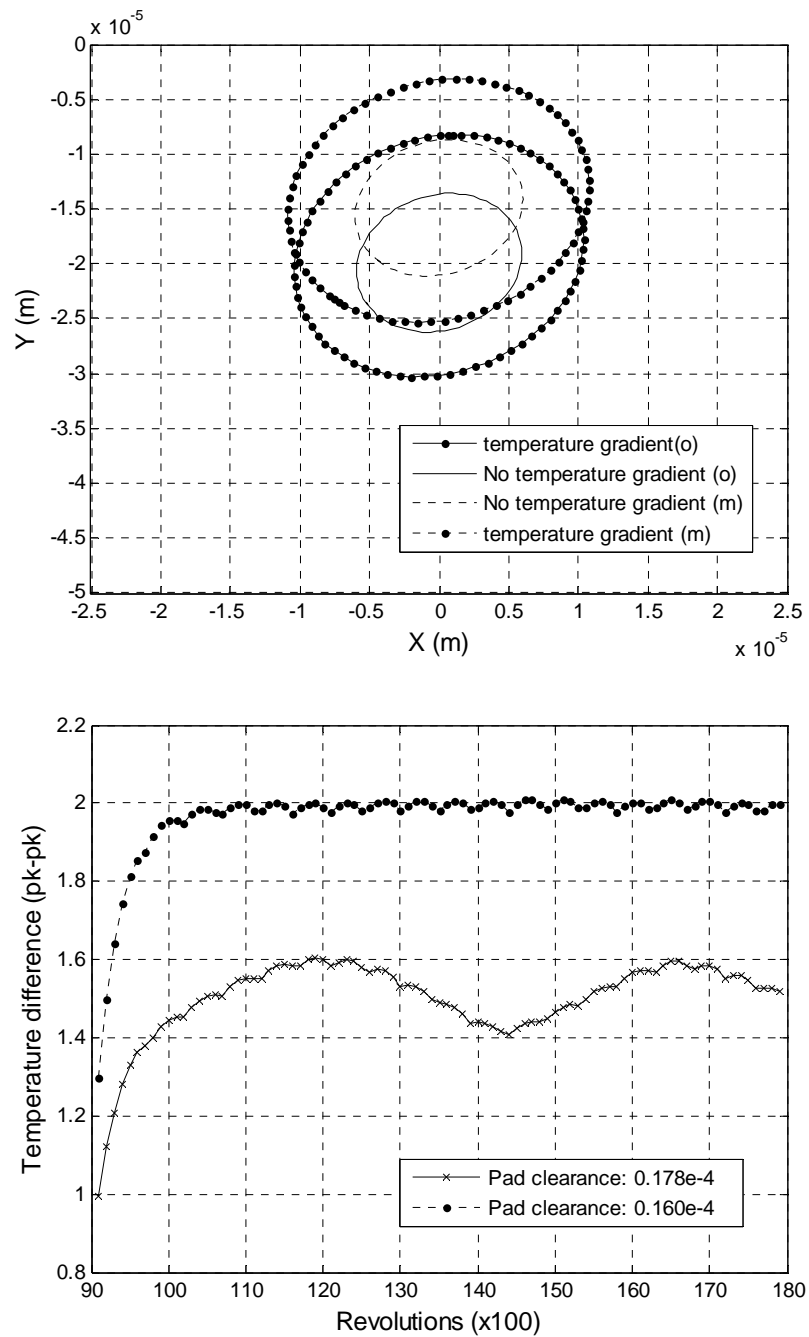
(a)

Fig. 3.31 the Methods to Mitigate the Morton Effect; (a) Reducing the Bearing

Clearance and (b) Lower Viscosity Lubricant
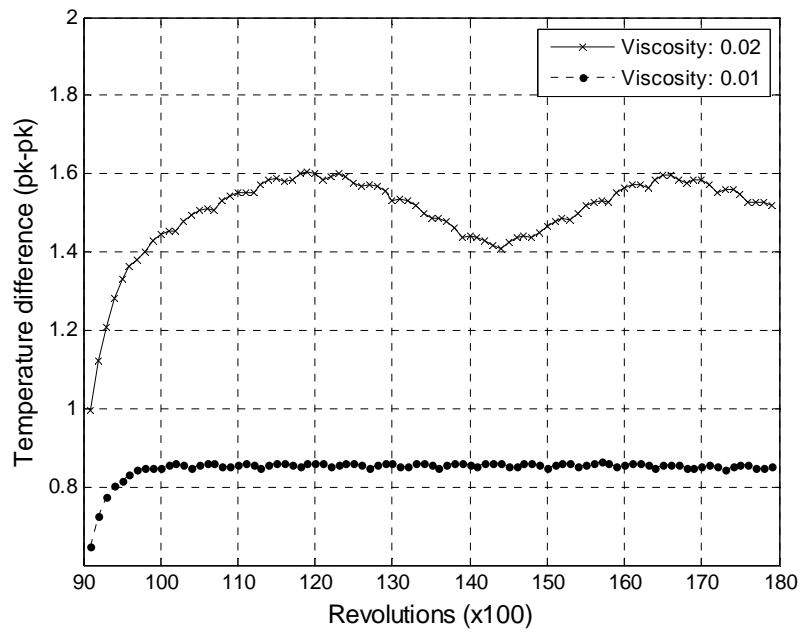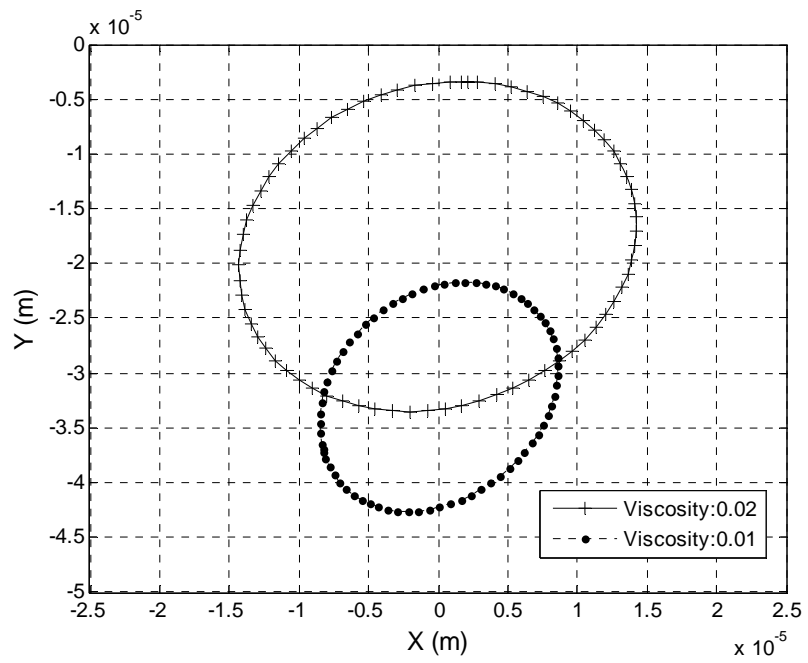
(b)

Fig. 3.31 Continued

CHAPTER IV

PRESSURE-DEPENDENT VISCOSITY REYNOLDS EQUATION

4.1 Overview

The Reynolds equation is the governing equation for fluid film motion in the fluid bearing applications. In the derivation, there are some assumptions; ; i) fluid is Newtonian fluid, ii) inertia and body force terms are negligible compared with the pressure and viscous terms, iii) there is a negligible variation of pressure across the fluid, and iv) viscosity is constant. However, in the EHL problem which occurred in rolling bearing element, the assumption that viscosity is constant is not valid.

In this chapter, the 2D modified pressure-dependent Reynolds equation for incompressible and isothermal liquid is derived. Even though the lubricant subjected to high pressure should no longer be considered incompressible, it is assumed that the density effect is much smaller than the viscosity effect. Furthermore, for the simplicity, it is assumed that the angular deformation of lubricant is negligible in the fluid film. After having described the new mathematical formulation for Reynolds equation, the effects of pressure-viscosity are studied in some cases-rigid rigid ball bearing and elastic ball bearing. Finally, the pressure distributions obtained from 2D modified Reynolds equation are compared with those of the classical Reynolds equation.

4.2 Derivation of Modified Reynolds Equation

The classical Reynolds equation represented by equation (4.1) is derived under

assumptions that i) fluid is Newtonian fluid, ii) inertia and body force terms are negligible compared with the pressure and viscous terms, iii) there is a negligible variation of pressure across the fluid, and iv) viscosity is constant.

$$\frac{\partial}{\partial x}\left(\frac{h^3}{12\mu}\frac{\partial p}{\partial x}\right)+\frac{\partial}{\partial y}\left(\frac{h^3}{12\mu}\frac{\partial p}{\partial y}\right)-\frac{\partial}{\partial x}\left(\frac{\alpha h}{3}Q_x\frac{\partial h}{\partial x}\frac{\partial p}{\partial x}\right)=\frac{U}{2}\frac{\partial(h)}{\partial x} \tag{4.1}$$

In order to consider pressure dependent viscosity effect, the Cauchy stress T is employed as a start point. For the incompressible fluid, if the Cauchy stress T is linear in stretching tensor D, the stress is expressed by [32]

$$T = -pI + 2\mu(p)D \tag{4.2}$$

where p is pressure acting on the fluid and $\mu(p)$ is a pressure-dependent viscosity. The stretching tensor D is defined by

$$D = \begin{bmatrix} \dfrac{\partial u}{\partial x} & \dfrac{1}{2}\left(\dfrac{\partial v}{\partial x}+\dfrac{\partial u}{\partial y}\right) & \dfrac{1}{2}\left(\dfrac{\partial w}{\partial x}+\dfrac{\partial v}{\partial z}\right) \\ \dfrac{1}{2}\left(\dfrac{\partial v}{\partial x}+\dfrac{\partial u}{\partial y}\right) & \dfrac{\partial v}{\partial y} & \dfrac{1}{2}\left(\dfrac{\partial w}{\partial y}+\dfrac{\partial u}{\partial z}\right) \\ \dfrac{1}{2}\left(\dfrac{\partial w}{\partial x}+\dfrac{\partial u}{\partial z}\right) & \dfrac{1}{2}\left(\dfrac{\partial w}{\partial y}+\dfrac{\partial u}{\partial z}\right) & \dfrac{\partial w}{\partial z} \end{bmatrix} \tag{4.3}$$

where u, v, and w are velocity of fluid along the x, y, and z direction.

For the classical Reynolds equation, the viscosity term in Eq. (4.2) is considered as constant. As the procedure for deriving the classical Reynolds equation, on substituting the stress term given by Eq.(4.2) into the balance of linear momentum written by eq. (4.4)

$$\nabla \cdot T + \rho \vec{b} = \rho \frac{\partial \vec{v}}{\partial t} \tag{4.4}$$

we obtain

$$-\nabla \cdot pI + \mu(p)\Delta\vec{v} + 2D[grad\,\mu(p)] + \rho\vec{b} = \rho\frac{\partial\vec{v}}{\partial t} \qquad (4.5)$$

where $\vec{b}$ denotes the specific body force. By assumption that the body force can be neglected and restricting our attention to steady state flows of incompressible fluid, Eq. (4.5) becomes

$$\nabla \cdot pI = \mu(p)\Delta\vec{v} + 2D[grad\,\mu(p)] \qquad (4.6)$$

Other expressions of Eq. (4.6) are as follows

$$\frac{\partial p}{\partial x} = \mu(p)\left(\frac{\partial^2 u}{\partial x^2} + \frac{\partial^2 u}{\partial y^2} + \frac{\partial^2 u}{\partial z^2}\right) + 2\frac{\partial\mu}{\partial x}\frac{\partial u}{\partial x} + \left(\frac{\partial v}{\partial x} + \frac{\partial u}{\partial y}\right)\frac{\partial\mu}{\partial y} + \left(\frac{\partial w}{\partial x} + \frac{\partial v}{\partial z}\right)\frac{\partial\mu}{\partial z} \qquad (4.7)$$

$$\frac{\partial p}{\partial y} = \mu(p)\left(\frac{\partial^2 v}{\partial x^2} + \frac{\partial^2 v}{\partial y^2} + \frac{\partial^2 v}{\partial z^2}\right) + 2\frac{\partial\mu}{\partial y}\frac{\partial v}{\partial x} + \left(\frac{\partial v}{\partial x} + \frac{\partial u}{\partial y}\right)\frac{\partial\mu}{\partial x} + \left(\frac{\partial w}{\partial y} + \frac{\partial v}{\partial z}\right)\frac{\partial\mu}{\partial z} \qquad (4.8)$$

$$\frac{\partial p}{\partial z} = \mu(p)\left(\frac{\partial^2 w}{\partial x^2} + \frac{\partial^2 w}{\partial y^2} + \frac{\partial^2 w}{\partial z^2}\right) + 2\frac{\partial\mu}{\partial z}\frac{\partial w}{\partial z} + \left(\frac{\partial w}{\partial x} + \frac{\partial u}{\partial z}\right)\frac{\partial\mu}{\partial x} + \left(\frac{\partial w}{\partial y} + \frac{\partial v}{\partial z}\right)\frac{\partial\mu}{\partial y} \qquad (4.9)$$

It is assumed that a variation of pressure across the fluid film is negligible and the fluid film is thin. Eqs (4.6)~(8) become

$$\frac{\partial p}{\partial x} = \mu(p)\frac{\partial^2 u}{\partial z^2} + 2\mu'\frac{\partial p}{\partial x}\frac{\partial u}{\partial x} + \left(\frac{\partial v}{\partial x} + \frac{\partial u}{\partial y}\right)\mu'\frac{\partial p}{\partial y} \qquad (4.10)$$

$$\frac{\partial p}{\partial y} = \mu(p)\frac{\partial^2 v}{\partial z^2} + 2\mu'\frac{\partial p}{\partial y}\frac{\partial v}{\partial x} + \left(\frac{\partial v}{\partial x} + \frac{\partial u}{\partial y}\right)\mu'\frac{\partial p}{\partial x} \qquad (4.11)$$

The third term of right hand side in Eqs. (4.10) and (4.11) represents the angular deformation of fluid. By assumption that angular deformation is negligible, Eqs (4.10) and (4.11) yields

$$\frac{\partial p}{\partial x} = \mu(p)\frac{\partial^2 u}{\partial z^2} + 2\mu'\frac{\partial p}{\partial x}\frac{\partial u}{\partial x} \qquad (4.12)$$

$$\frac{\partial p}{\partial y} = \mu(p)\frac{\partial^2 v}{\partial z^2} + 2\mu'\frac{\partial p}{\partial y}\frac{\partial v}{\partial x} \qquad (4.13)$$

Since the pressures has been assumed to be a function of x and y only, these equations can be integrated directly to give expressions for the velocity.

$$u = \frac{1}{\mu}\left(1 - 2\mu'\frac{\partial u}{\partial x}\right)\frac{\partial p}{\partial x}\frac{z^2}{2} + c_1 z + c_2 \qquad (4.14)$$

$$v = \frac{1}{\mu}\left(1 - 2\mu'\frac{\partial v}{\partial y}\right)\frac{\partial p}{\partial y}\frac{z^2}{2} + c_1 z + c_2 \qquad (4.15)$$

If we assume zero slip at the fluid-solid interface, the boundary values for velocity are as follows

$$\begin{aligned} at\ z &= 0,\ \ u = u_b, v = 0, w = 0 \\ at\ z &= h,\ \ u = u_a, v = 0, w = 0 \end{aligned} \qquad (4.16)$$

The subscripts a and b refer to conditions on the upper and lower surfaces, respectively. With the boundary values given in Eq. (4.16), the velocity components can be written as

$$u = \frac{1}{\mu}\left(1 - 2\mu'\frac{\partial u}{\partial x}\right)\frac{\partial p}{\partial x}\frac{z^2}{2} + c_1 z + c_2 \qquad (4.17)$$

$$v = \frac{1}{\mu}\left(1 - 2\mu'\frac{\partial v}{\partial y}\right)\frac{\partial p}{\partial y}\frac{z^2}{2} + c_1 z + c_2 \qquad (4.18)$$

where

$$C_1 = \frac{1}{h}(u_a - u_b) - \frac{h}{2\mu}\left(1 - 2\mu'\frac{\partial u}{\partial x}\right)\frac{\partial p}{\partial x} \qquad (4.19)$$

$$C_2 = u_b \qquad (4.20)$$

$$C_3 = -\frac{h}{2\mu}\left(1-2\mu'\frac{\partial v}{\partial y}\right)\frac{\partial p}{\partial y} \tag{4.21}$$

$$C_4 = 0 \tag{4.22}$$

The modified Reynolds equation is formed by introducing velocity components expressions into the continuity equation written by

$$\int_0^h \left[\frac{\partial \rho}{\partial t}+\frac{\partial \rho u}{\partial x}+\frac{\partial \rho v}{\partial y}+\frac{\partial \rho w}{\partial z}\right]dz = 0 \tag{4.23}$$

Using Leibniz's integration formula, the continuity equation becomes

$$h\frac{\partial \rho}{\partial t}+\frac{\partial M_x}{\partial x}+\frac{\partial M_y}{\partial y}=0 \tag{4.24}$$

where

$$M_x = \rho\int_0^h u\,dz \tag{4.25}$$

$$M_y = \rho\int_0^h v\,dz \tag{4.26}$$

Substituting Eqs. (4.17)~(18) into Eqs. (4.25)~(26) yields

$$M_x = \rho\left[-\frac{h^3}{12\mu}\frac{\partial p}{\partial x}+\frac{h}{2}(u_a+u_b)-\frac{\mu'}{\mu}\int_0^h z(z-h)\frac{\partial u}{\partial x}\frac{\partial p}{\partial x}dz\right] \tag{4.27}$$

$$M_x = \rho\left[-\frac{h^3}{12\mu}\frac{\partial p}{\partial y}-\frac{\mu'}{\mu}\int_0^h z(z-h)\frac{\partial v}{\partial y}\frac{\partial p}{\partial y}dz\right] \tag{4.28}$$

Plugging Eqs.(4.27)~(28) into continuity equation yields

$$\frac{\partial}{\partial x}\left[\left(\frac{\rho h^3}{12\mu}-\rho\frac{\mu'}{\mu}\int_0^h z(h-z)\frac{\partial u}{\partial x}dz\right)\frac{\partial p}{\partial x}\right]+\frac{\partial}{\partial y}\left[\left(\frac{\rho h^3}{12\mu}-\rho\frac{\mu'}{\mu}\int_0^h z(h-z)\frac{\partial v}{\partial y}dz\right)\frac{\partial p}{\partial y}\right]$$
$$=u\frac{\partial \rho h}{\partial x}+\frac{\partial \rho h}{\partial t} \tag{4.29}$$

This is a modified Reynolds equation with considering pressure-dependent viscosity. If the viscosity is constant and fluid is incompressible for steady state flow, Eq. (4.29) becomes the classical Reynolds equation expressed by eq (4.1). As mentioned earlier, we only considers in the steady state flow for incompressible fluid. Therefore, modified Reynolds equation becomes

$$\frac{\partial}{\partial x}\left[\left(\frac{h^3}{12\mu}-\frac{\mu'}{\mu}\int_0^h z(h-z)\frac{\partial u}{\partial x}dz\right)\frac{\partial p}{\partial x}\right]+\frac{\partial}{\partial y}\left[\left(\frac{h^3}{12\mu}-\frac{\mu'}{\mu}\int_0^h z(h-z)\frac{\partial v}{\partial y}dz\right)\frac{\partial p}{\partial y}\right]=u\frac{\partial h}{\partial x}$$

(4.30)

For further simplifying Eq (4.30) and easy access by numerical methods, we define flow rate along the x-z and y-z plane.

$$Q_x = b \times h_{avg} \times u_{avg}$$ (4.31)

$$Q_y = a \times h_{avg} \times v_{avg}$$ (4.32)

where a and b are the contact length in the x-z and y-z plane for point contact.

By substituting $\partial u_{av}/\partial x$, $\partial v_{av}/\partial y$ for $\partial u/\partial x$, $\partial v/\partial y$, the second and fourth term of left hand side of Eq. (4.30) become

$$\int_0^h z(h-z)\frac{\partial u}{\partial x}dz = Q_x\frac{\partial h^2}{6\partial x}$$ (4.33)

$$\int_0^h z(h-z)\frac{\partial v}{\partial y}dz = Q_y\frac{\partial h^2}{6\partial y}$$ (4.34)

The pressure-dependent viscosity proposed by Barus is written by

$$\mu = \mu_0 e^{\alpha p}$$ (4.35)

The Q_y can be negligible in laminar flow and substituting eq (4.33) ~ (35) into eq (4.30)

and yields

$$\frac{\partial}{\partial x}\left(\frac{h^3}{12\mu}\frac{\partial p}{\partial x}\right)+\frac{\partial}{\partial y}\left(\frac{h^3}{12\mu}\frac{\partial p}{\partial y}\right)-\frac{\partial}{\partial x}\left(\frac{\alpha}{6}Q_x\frac{\partial h^2}{\partial x}\frac{\partial p}{\partial x}\right)=u\frac{\partial(h)}{\partial x} \qquad (4.36)$$

In EHL contact problems, the number of parameters can be significantly reduced. The dimensionless equation used in this study are mainly based on the Hertzian dry contact parameters, for Hertzian theory gives the pressure profile, the geometry of the contact region, and the elastic deformation of the contacting bodies in the case of a loaded contact between parabolically shaped elastic solids.

The dimensionless variables are as followings

$$X=\frac{x}{b}, \; Y=\frac{y}{a}, \; \bar{\eta}=\frac{\eta}{\eta_0}, \; H=h\frac{R_x}{b^2}, \; P=\frac{p}{p_{max}}, \; U=u\frac{\eta_0}{E'R_x}, \; \bar{Q}_x=b\times H_{avg}\times U/2 \quad (4.37)$$

After substitution of these variables in Eq. (4.36), the modified Reynolds equation becomes

$$\frac{\partial}{\partial X}\left(\varepsilon\frac{\partial P}{\partial X}\right)+\frac{\partial}{\partial Y}\left(\frac{\varepsilon}{k^2}\frac{\partial P}{\partial Y}\right)-\frac{\partial}{\partial X}\left(\varsigma\bar{Q}_x\frac{\partial H^2}{\partial X}\frac{\partial P}{\partial X}\right)=\frac{\partial H}{\partial X} \qquad (4.38)$$

where ε and ς as dimensionless parameters are defined as

$$\varepsilon=\frac{b^3H^3p_{max}}{12E'R_x^3U\bar{\eta}} \qquad (4.39)$$

$$\varsigma=\frac{b^2\alpha p_{max}}{3R_x^2U} \qquad (4.40)$$

If the pressure gradient along the Y direction can be negligible, the modified Reynolds equation is same as Rajagopal's derivation [32].

4.3 Numerical Solutions

The effect of the extra term appearing in the modified Reynolds equation in the case of point contact is investigated. In practical cases, the high pressure induced the elastic deformation, but to illustrate the effect of new term, we first consider the rigid body point contact case. And then we also investigate the elastic point contact.

4.3.1 Rigid Ellipsoidal Solids

Film thickness; The dimensionless film thickness between two rigid ellipsoidal solids can be written as

$$H = H_0 + \frac{X^2}{2} + k^2 \frac{Y^2}{2\alpha_a} \tag{4.41}$$

where the elliptic ratio k and α_a are defined as

$$k = \frac{a}{b} \quad \alpha_a = \frac{R_y}{R_x} \tag{4.42}$$

The unknowns are H_0, Pressure P, and cavitation boundary. To consider cavitation boundary condition, Reynolds boundary condition is used; when the negative pressure occurs, the negative value set to zero. In addition, at the inlet, the inlet pressure is taken as zero to give fully flooded conditions. To solve EHL point contact problem, FEM and relaxation method are utilized. The Hertzian pressure distribution is used as the initial pressure distribution. In the rigid body case, the uniform mesh scheme is applied to computational domain. The number of element is 900.

Discretized Force Balance Equation: The force balance equation ensures that the

integral over the pressure in the contact region balances the external applied load. Since the lubricant film carries the entire contact load exerted on the contacting bodies, the integral over the pressure in the film is equal to the applied load. The force balance equation reads

$$\iint p\,dx\,dy = F \tag{4.43}$$

The force balance equation is used to determine the value of the offset film thickness, H_0. The dimensionless force balance equation is written by

$$\iint P\,dX\,dY = \frac{2}{3}\pi \tag{4.44}$$

In the discrete form, the left hand side of Eq. (4.44) can be written as

$$\int_\Omega P\,dX\,dY = \sum_{e=1}^{N} \int_\Omega P^{(e)}\,dX\,dY = \sum_{e=1}^{N}\sum_{j=1}^{9} C_j^{(e)} P_j^{(e)} \tag{4.45}$$

where

$$C_j^{(e)} = \int_\Omega \phi_j\,dX\,dY \tag{4.46}$$

The computational domain is selected as $-2.5 \le X \le 1.2$ and $-2.0 \le Y \le 2.0$. In this case, starvation or vortex could be avoided. Due to the symmetry of the domain in Y direction, only positive half of $0.0 \le Y \le 2.0$ is taken into account in the computation. In addition, the Reynolds boundary condition is applied when the cavitation occurs near the outlet region. Figure 4.1 shows that the modified Reynolds equation yields higher pressure than the original Reynolds equation.
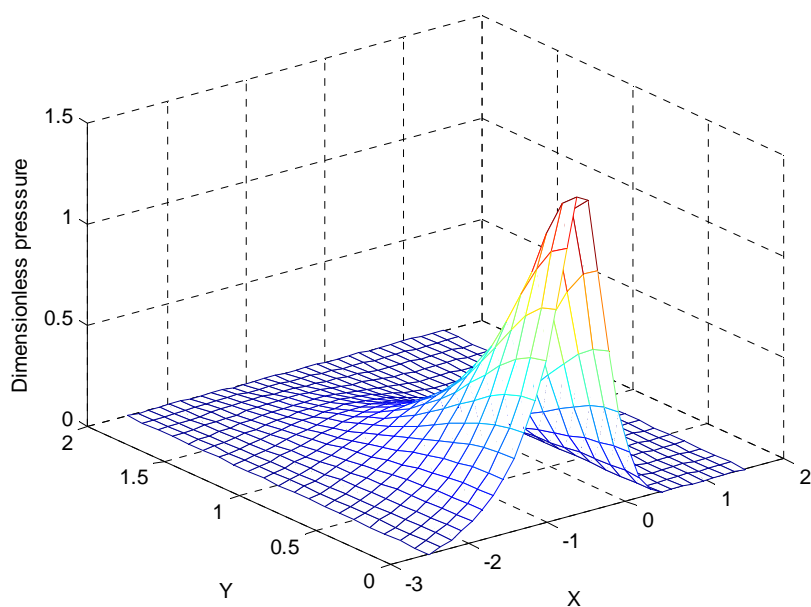
(a)
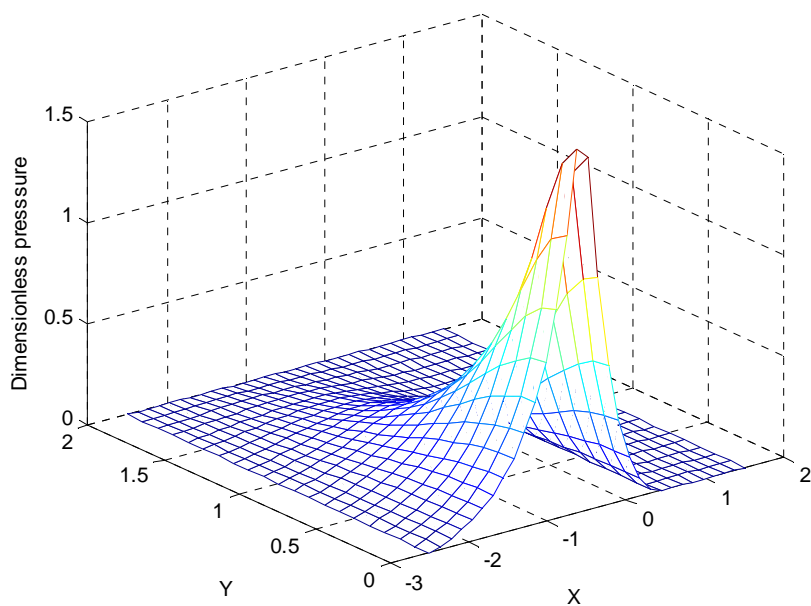
(b)

Fig. 4.1. Pressure Distribution for Rigid Body Case; (a) Original Reynolds Equation (ORE), (b) Modified Reynolds Equation (MRE), and (c) Comparison between ORE and MRE
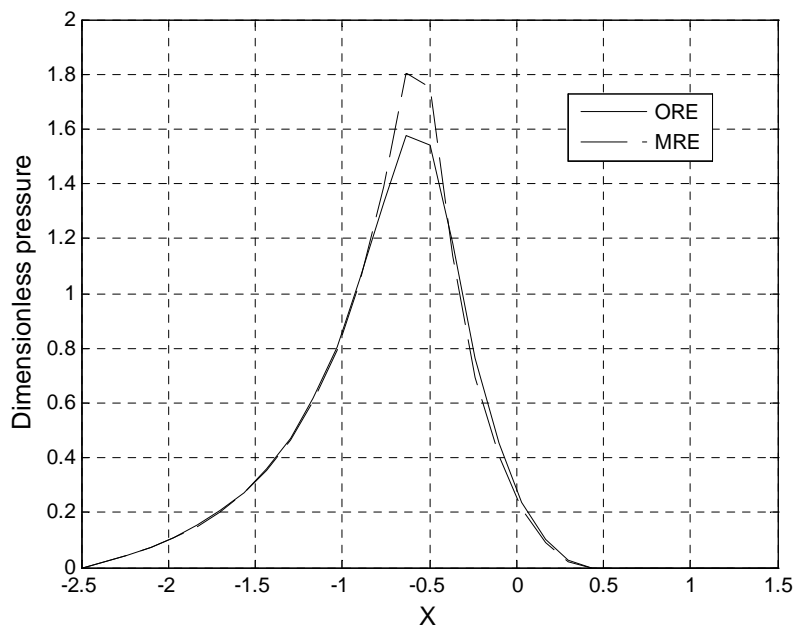
(c)

Fig. 4.1. Continued

4.3.2 Elastic Ellipsoidal Solids

In the point contact EHL problems, two ellipsoidal solids subjected to a pressure induces deformation of elastic solids. To calculate the elastic deformation due to pressure, Boussinesq's equation is used [49] and the following discretization is based on Hou et al.'s approach [50]. The resulting elastic deformation can be calculated by the following equation

$$\delta(\overline{x},\overline{y}) = \frac{1-\nu^2}{\pi E} \int\int \frac{p(x,y)}{\sqrt{(x-\overline{x})^2+(y-\overline{y})^2}}\,dxdy \qquad (4.47)$$

In an element domain consists of nine-node element, the dimensionless equation of elastic deformation for the deformation at the node (u,v) by the pressure profile on the

element can be expressed as

$$\delta_j^{(e)}(u,v) = \frac{3FR_x^2}{\pi^2 ab^3 E'} \sum_{j=1}^{9} P_j^{(e)} \iint \frac{\phi_j(\bar{X},\bar{Y})}{\sqrt{(\bar{X})^2 + (\bar{Y})^2}} d\bar{X} d\bar{Y} = \frac{3FR_x^2}{\pi^2 ab^3 E'} \sum_{j=1}^{9} d_j^{(e)} P_j^{(e)} \qquad (4.48)$$

where

$$d_j^{(e)}(u,v) = \int_{\Omega_e} \frac{\phi_j(\bar{X},\bar{Y})}{\sqrt{\bar{X}^2 + \bar{Y}^2}} d\bar{X} d\bar{Y} = \int_{x_1}^{x_3} \int_{y_1}^{y_3} \frac{\phi_j(\bar{X},\bar{Y})}{\sqrt{\bar{X}^2 + \bar{Y}^2}} d\bar{X} d\bar{Y} \qquad (4.49)$$

Because the shape function $\phi_j = b_1^j(\bar{X}^2 + b_2^j \bar{X} + b_3^j)(\bar{Y}^2 + b_4^j \bar{Y} + b_5^j)$, $d_j^{(e)}$ can be expressed

as

$$d_j^{(e)}(u,v) = b_1^j \left[g(\bar{X}_1,\bar{Y}_1) + g(\bar{X}_3,\bar{Y}_3) - g(\bar{X}_1,\bar{Y}_3) - g(\bar{X}_3,\bar{Y}_1) \right] \qquad (4.50)$$

where

$$g(\bar{X},\bar{Y}) = \begin{cases} 0 & \text{if } \bar{X}^2 + \bar{Y}^2 = 0 \\ g(\bar{X},\bar{Y}) & \text{if } \bar{X}^2 + \bar{Y}^2 \neq 0 \end{cases} \qquad (4.51)$$

The analytic expression of $g_1(\bar{X},\bar{Y})$ is given as

$$
\begin{aligned}
g(\bar{X},\bar{Y}) = t^3 & \left[\frac{\bar{X}}{2}\left(\frac{\bar{Y}}{4} + \frac{b_4^j}{3} \right) + b_2^j \frac{\bar{Y}}{4} + \frac{b_2^j b_4^j}{3} \right] + \frac{\bar{X}}{2}\left(b_2^j b_5^j - b_2^j \frac{\bar{X}^3}{4} - \frac{\bar{X}^4}{4} + 2b_5^j \frac{\bar{X}^2}{4} \right) \ln(\bar{Y}+t) \\
& - \frac{\bar{X}^2 \bar{Y} t}{8}\left(\frac{\bar{X}}{2} + b_2^j \right) - \frac{\bar{Y}^5}{10}\left(L - \frac{1}{5} \right) - \frac{\bar{X}\bar{Y}t}{40}\left(\bar{Y}^2 - \frac{3\bar{X}^2}{2} \right) + b_5^j \bar{Y}\left(b_2^j \frac{t}{2} - b_3^j \right) \\
& + \frac{\bar{X}\bar{Y}t}{6}\left(b_3^j + b_5^j \right) + \frac{b_3^j b_4^j}{2}\left[\left(t^2 - \bar{X}^2 \right) L + \bar{X}^2 + \bar{X}t - \frac{\bar{Y}^2}{2} \right] - b_4^j \frac{\bar{Y}^4}{8}\left(L - \frac{1}{4} \right) \\
& - b_4^j \frac{\bar{X}t}{24}\left(\bar{Y}^2 - 2\bar{X}^2 \right) + \frac{\bar{Y}^3}{3}\left(L - \frac{1}{3} \right)\left(b_3^j - \frac{b_5^j}{2} \right) + b_3^j \bar{X} \ln(\bar{Y}+t)\left(b_5^j - \frac{\bar{X}^2}{6} \right)
\end{aligned}
$$

$$(4.52)$$

here

$$t = \sqrt{\bar{X}^2 + \bar{Y}^2} \qquad (4.53)$$

$$
L = \begin{cases} \ln(\bar{X}+t) & \text{if } \bar{X}+t \neq 0 \\ 0 & \text{if } \bar{X}+t = 0 \end{cases} \tag{4.54}
$$

For the entire contact region consisting of N elements, the deformation at node (u,v) produced by all global nodal pressure can be written as follows

$$
\delta(u,v) = \frac{3FR_x^2}{\pi^2 ab^3 E'} \sum_{e=1}^{N} \sum_{j=1}^{9} d_j^{(e)} P_j^{(e)} \tag{4.55}
$$

It defines here load parameter, W and material parameter, G of conventional EHL analysis

$$
W = \frac{F}{E'R_x^2} \quad G = \alpha E' \tag{4.56}
$$

In this case, the non-uniform mesh scheme is applied to computational domain for obtaining an accurate pressure distribution near the outlet region. The number of element is 900. The computation domain and the boundary condition are same as in rigid body cases.

Load applied to the rolling element bearings depends on the operating conditions. The rolling bearing element manufacturers recommend the maximum applied load by introducing load rating – static load rating and dynamic load rating. The static load rating is the maximum radial or thrust load a bearing can endure without excessive permanent deformation. Maximum deformation of rolling element or race that does not significantly degrade bearing performance is 0.0001 times the diameter of rolling element bearings. The dynamic load rating is the load at which 90% of a group of bearings can survive 1 million inner-race revolutions. The fatigue life of rolling elements is evaluated based on these load ratings. The Hertzian contact stress corresponding to

maximum load is around 4 GPa. In general rolling bearing applications, the Hertzian stress ranges from 0.5 GPa to 2 GPa for longer lifespan of rolling elements bearings. Thus, in this paper, moderate operating condition where the maximum Hertzian contact stress is around 1 GPa is under consideration. Table 4.1 shows the values used in numerical simulation.

Figure 4.2 shows the 3-D pressure distribution for heavy load case. Figure 4.3 shows the pressure distribution and film thickness at Y=0 for heavy load case. The first peak pressure of modified Reynolds equation is similar to that of original Reynolds equation, but slightly moved to outlet region. The second peak pressure which called 'pressure spike' increased by 10%, while the minimum film thickness slightly increased for the modified Reynolds equation. For the moderate load case, the second pressure peak increased by 6%, but the minimum film thickness is close to that of the original Reynolds equation shown in Figure 4.4. When the applied load is light, the pressure distribution and film thickness for modified Reynolds equation are same as those of original Reynolds equation shown in Figure 4.5.

Table 4.1 Simulation Parameters

	Value			Value
$R_x(m)$	0.01114	$U(10^{-11})$		1.0
$R_y(m)$	0.01582	G		4522
$\eta_0\,(Ns/m^2)$	0.01326	$W(10^{-6})$ ( ); Maximum Hertizan Pressure	Light	0.54 (0.57 GPa)
$\alpha\,(1/Pa,\times10^{-8})$	2.05		Moderate	1.83 (0.86 GPa)
$E'(GPa)$	2.2		Heavy	3.66 (1.10 GPa)
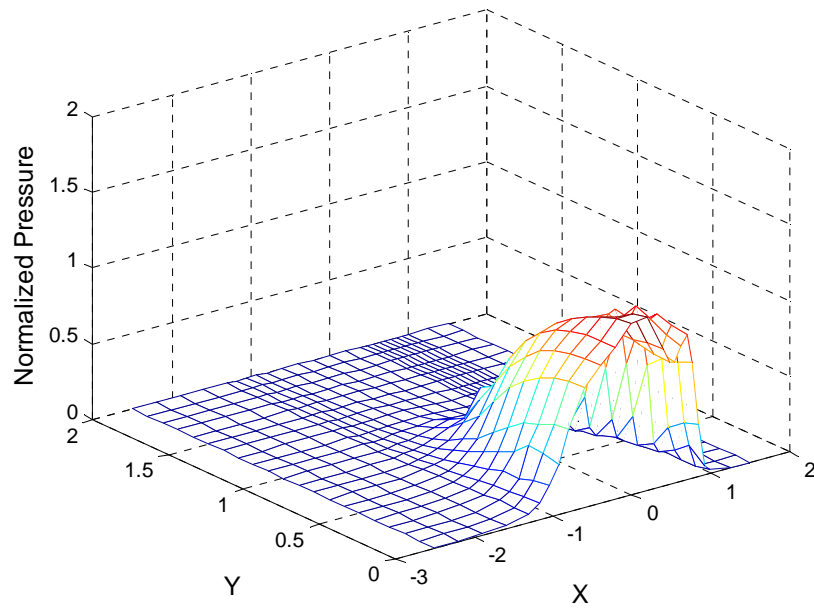
(a)
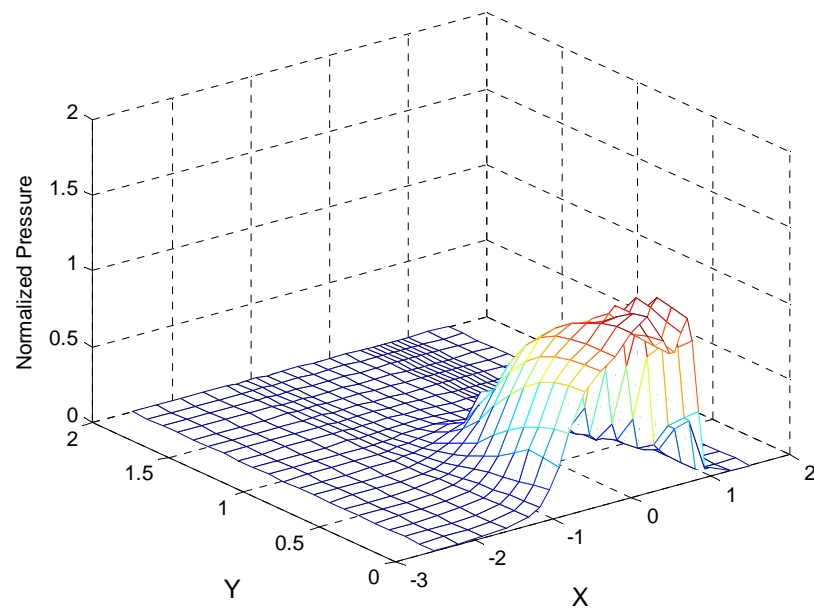
(b)

Fig. 4.2 Normalized Pressure Distribution; (a) Original Reynolds Equation(ORE)

and (b) Modified Reynolds Equation(MRE)
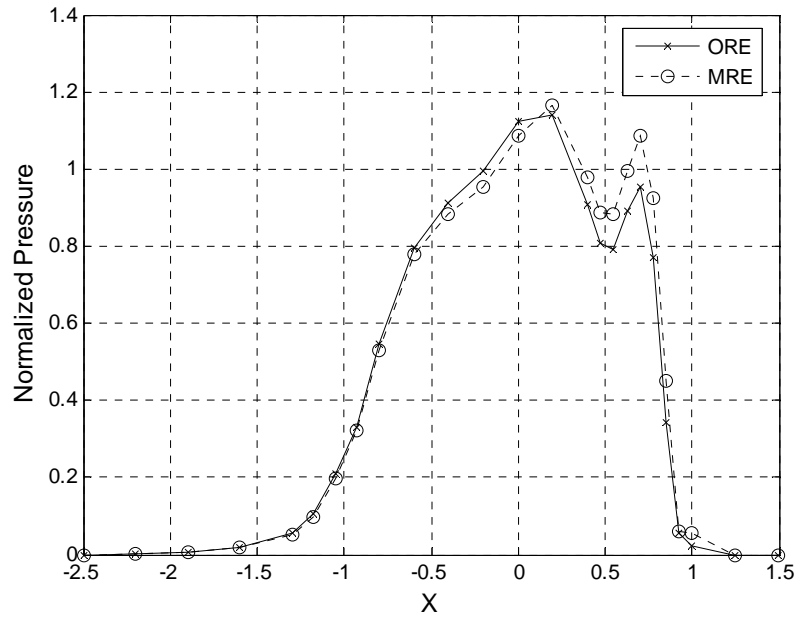
(a)
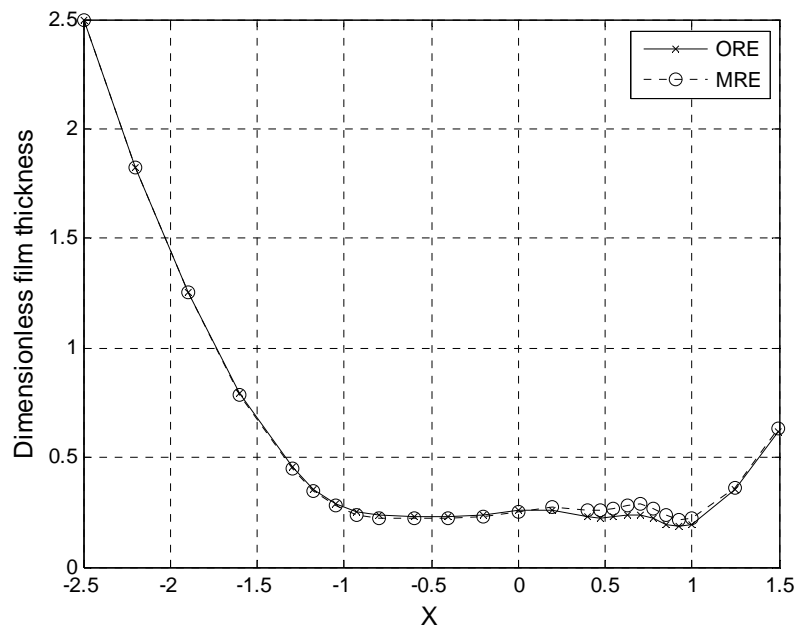
(b)

Fig 4.3 Simulation Results for Heavy Load: (a) Pressure Distribution and (b) Film Thickness
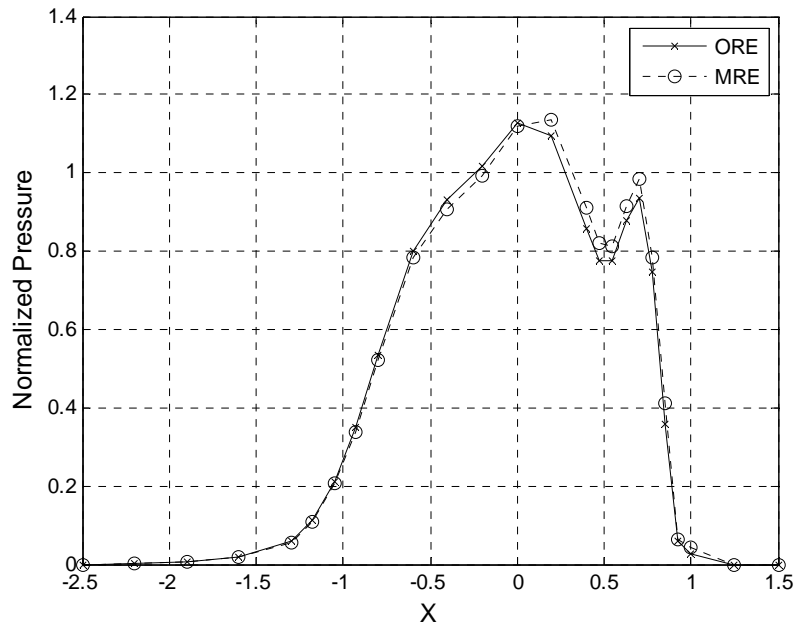
(a)
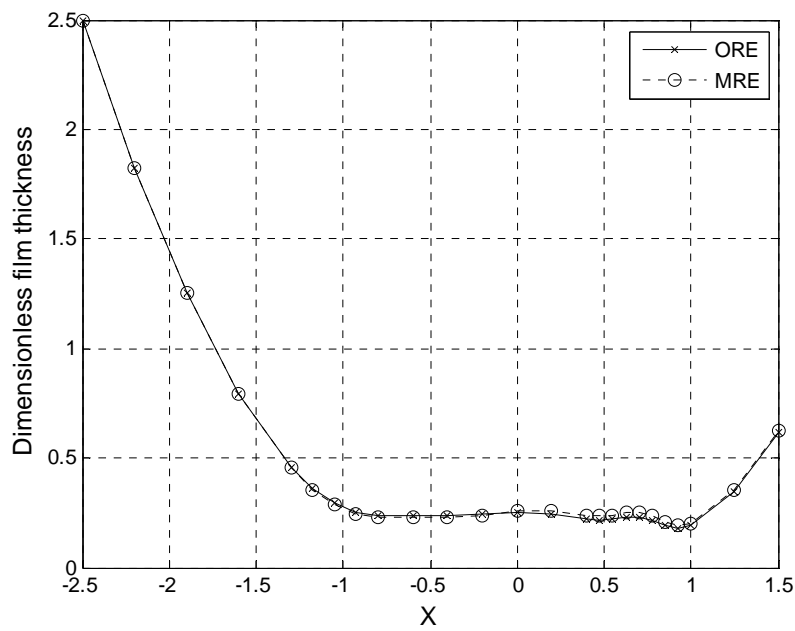
(b)

Fig. 4.4 Simulation Results for Moderate Load: (a) Pressure Distribution and (b)
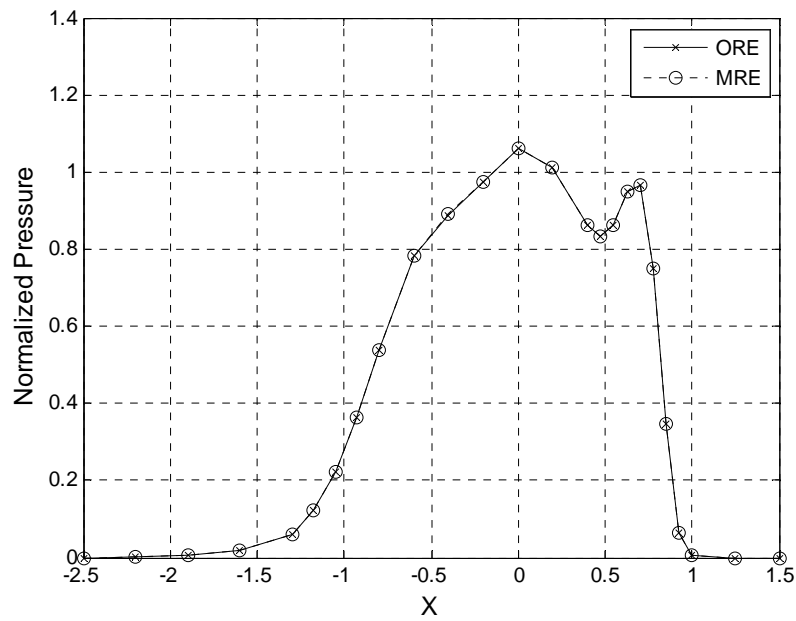
Film Thickness

(a)
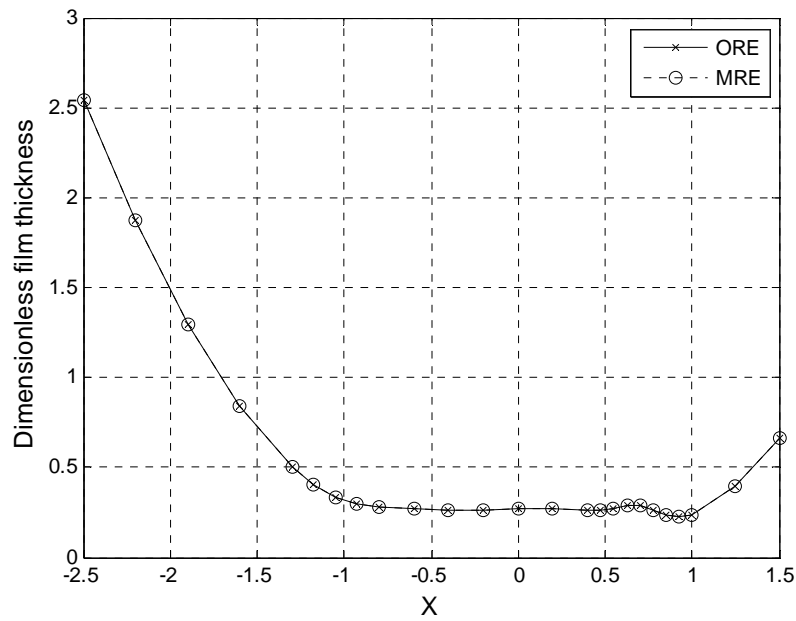
(b)

Fig. 4.5 Simulation Results for Light Load: (a) Pressure Distribution and (b) Film

Thickness

CHAPTER V

CONCLUSION AND FUTURE WORK

In this dissertation, the three research topics are considered, ;) catcher bearing fatigue life prediction, ii) the Morton effect, and iii) the two dimensional modified Reynolds equation.

Firstly, for the life prediction of the catcher bearing, it was employed a high fidelity, thermal-structural, fully nonlinear ball bearing, and flexible finite element shaft model, and rainflow counting approach to evaluate the life of catcher bearings in terms of number of drop occurrences to failure. It was found that decreasing rotor-inner race contact friction, reducing catcher bearing air gap, applying a constant side load after a drop event, reducing support stiffness and increasing support damping, and reducing speed (rpm) all increase the life of an AMB catcher bearing. The life prediction involved determining contact load, Hertzian stresses, subshear stress, surface shear stress, and thermal growths. In addition, simulation results indicated that forward whirl can occur for a rotor with large imbalance.

Secondly, a method for calculating the temperature difference (peak to peak) in the plain or tilting pad journal bearing for a given orbit was suggested. For plain journal bearing case, the prediction of temperature difference was similar to published data. Journal of tilting pad bearing is also experienced asymmetric thermal heating, which induced the thermal bow. The differential increased with orbit size for two cases. However, the relationship between orbit size and differential was nonlinear as orbit size increases. Furthermore, simulation results indicate that the non-uniform temperature

distribution of journal can be removed by i) small amplitude orbit, ii) small eccentricity. In addition, the theoretical model including FE rotor model and nonlinear bearing model showed the synchronous thermal instability due to asymmetric journal heating known as Morton Effect. The simulation result of current approach agreed well with the published data. Although there was a small temperature difference, this differential caused to significant thermal bow and induced instability phenomenon under some conditions. To reduce the Morton synchronously instability, reducing bearing clearances and lower viscosity lubricant were utilized to simulation model. The simulation results show the reduced orbit resulted from two suggested methods.

Finally, the classical Reynolds equation derived under the assumption of a constant viscosity is not valid for Elastohydrodynamics problem occurred in rolling element bearings. In order to consider the variation of viscosity with pressure, the modified Reynolds equation was derived. The modified Reynolds equation contains an extra terms which takes into account pressure dependent viscosity. For the three load cases-heavy, moderate, and light, the pressure distribution and film thickness were obtained. The numerical solutions showed that the pressure dependent viscosity characteristic of lubricant yielded slightly higher pressure than the original Reynolds equation, and the peak pressure gets higher as the applied load increases.

The expected future works can be addressed as follows:

(a) Conduct rotor drop test and correlate test data with simulation results

(b) Develop a similar fatigue life prediction method for roller and plain sleeve catcher bearings

(c) Conduct the Morton Effect instability test

(d) Apply the modified Reynolds equation to prediction of ball bearing stiffness and damping.

REFERENCES

[1]   Schweitzer, G., Bleuler, H., and Traxler, A. 1994, *Active Magnetic Bearings: Basics, Properties and Applications*, vdf Hochschulverlag AG, Zurich.

[2]   Ishii, T., and Kirk, R. G. 1996, "Transient Response Technique Applied to Active Magnetic Bearing Machinery during Rotor Drop," ASME J. Vibr.Acoust., **118**: 154–163.

[3]   Orth, M., Erb, R., and Nordmann, R. 2000, "Investigations of the Behavior of a Magnetically Suspended Rotor during Contact With Retainer Bearings," in Proceedings of the Seventh ISMB, Zurich, Switzerland.

[4]   Ishii, T., and Kirk, R. G. 1991, "Transient Response Technique Applied to Active Magnetic Bearing Machinery During Rotor Drop," ASME Conference in Proceedings, Rotating Mach. Veh. Dyn., **35**: 191–199.

[5]   Fumagalli, M., Varadi, P., and Schweitzer, G. 1994, "Impact Dynamics of High Speed Rotors in Retainer Bearings and Measurement Concepts," in Proc. of the Fourth International Symposium on Magnetic Bearings, Zurich, Switzerland, 239–244.

[6]   Fumagalli, M. A. 1997, "Modelling and Measurement Analysis of the Contact Interaction Between a High Speed Rotor and Its Stator," Ph.D. thesis, Swiss Institute of Technology, Switzerland.

[7]   Cole, M. O. T., Keogh, P. S., and Burrows, C. R. 2002, "The Dynamic Behavior of a Rolling Element Auxiliary Bearing Following Rotor Impact," ASME J. Tribol., **124**: 406–413.

[8]   Sun, G. 2006, "Rotor Drop and Following Thermal Growth Simulations using Detailed Bearing and Damper Models," J. of Sound and Vibration, **289**: 334-359.

[9]   Sun, G., Palazzolo, A., Provenza, A. and Montague, G. 2004, "Detailed Ball Bearing Model for Magnetic Suspension Auxiliary Service," J. of Sound and Vibration, **269**: 933-963.

[10]   Taktak, S., Ulker, S., and Gunes, I. 2008, "High Temperature Wear and Friction Properties of Duplex Surface Treated Bearing Steels," Surface and Coatings Technology, **202**: 3367-3377.

[11]   Böhmer, H., Lösche, T., Ebert, F., and Streit, E. 1999, " The Influence of Heat Generation in the Contact Zone on Bearing Fatigue Behavior," ASME J. Tribol., **121**: 462-467.

[12]   API Std 617, *Axial and Centrifugal Compressors and Expander Compressors for Petroleum, Chemical and Gas Industry Services*, seventh ed. 2002, American Petroleum Institue.

[13]   Sun,G. 2006, "Auxiliary Bearing Life Prediction Using Hertzian Contact Bearing Model," J. of Sound and Vibration, **128**: 203-209.

[14]   Keogh, P.S., and Morton, P.G. 1994, "The dynamic nature of rotor thermal bending due to unsteady lubricant shearing within bearing," Proc.R.Soc. Lond. A **445**: 157-163.

[15]   deJongh, F.M., and Morton, P.G. 1994, "The synchronous instability of a compressor rotor due to bearing journal differential hearing," ASME paper **94-GT-35**: 1-13.

[16]   Gomiciaga, R. and Keogh, P. S. 1999, "Orbit Induced Journal Temperature Variation in Hydrodynamic Bearings," ASME Journal of Tribology, **121**: 77-84

[17]   Larsson,B. 1999, "Journal Asymmetric Hearing-Part I: Nonstationary Bow," Journal of Tribology, **121**: 157-163

[18]   Larsson,B. 1999, "Journal Asymmetric Hearing-Part II: Alteration of Rotor Dynamic Properties," Journal of Tribology, **121**: 164-168

[19]   Balbahadur, A.C. and Kirk, R.G. 2004, "Part I-Theoretical Model for a Synchronous Thermal Instability Operating in Overhung Rotors," International Journal of Rotating Machinery, **10(6)**: 469-475.

[20]   Balbahadur, A.C. and Kirk, R.G. 2004, "Part II-Case Studies for a Synchronous Thermal Instability Operating in Overhung Rotors," International Journal of Rotating Machinery, **10(6)**: 477-487.

[21]   Murphy, B.T. and Lorenz J.A. 2010, "Simplified Morton Effect Analysis for Synchronous Spiral Instability," Journal of Vibration and Acoustics, **132**: 051008-1-7.

[22]   Reynolds, O. 1886, "On the Theory of Lubrication and Its Application to Mr.Beauchamp Tower's Experiments, Including an Experimental Determination of the Viscosity of Olive Oil," *Philos. Trans. R. Soc. Lond.*, **177**: 157-234

[23]   Bendler, J.T., Fontanella, J.J., and Schlesinger, M.F. 2001, "A New Vogel-like Law:ionic Conductivity, Dielectric Relaxation and Viscosity near the Glass Transition," Phys. Rev. Lett. **87**: 195503.

[24]   Cutler, W. G., McMickles, R. J., Webb, W. & Schiessler, R. W. 1958, "Study of

the Compressions of Several High Molecular Weight Hydrocarbons," *J. Chem. Phys.*, **29**: 727-740.

[25] Griest, E. M., Webb, W. & Schiessler, R. W., 1958, "Effect of Pressure on Viscosity of Higher Hydrocarbons and Their Mixtures," *J. Chem. Phys.* **29**: 711-720.

[26] Johnson, K. L. & Cameron, R. 1967, "Shear Behaviour of Elastohydrodynamic Oil Films at High Rolling Contact Pressures," *Proc. Inst. Mech. Engrs,* **182**: 307-319.

[27] Johnson, K. L. & Greenwood, J. A. 1980, "Thermal Analysis of an Eyring Fluid in Elastrohydrodynamic Traction," *Wear,* **61**: 355-374.

[28] Johnson, K. L. & Tevaarwerk, J. L. 1977, "Shear Behaviour of Elastohydrodynamic Oil Films," *Proc.R. Soc. Lond.* **A356**: 215-236.

[29] Paluch, M., Dendzik, Z. & Rzoska, S. J. 1999, "Scaling of High-Pressure Viscosity Data in Lowmolecular-Weight Glass-Forming Liquids," *Phys. Rev.* **B60**: 2979-2982.

[30] Barus, C. 1983, "Isotherms, Isopiestics, and Isometrics Relative to Viscosity," *Am. J. Sci.*, **45**: 87-96

[31] Roelands, C. J. A. 1966, "Correlation Aspects of the Viscosity-Temperature-Pressure Relationship of Lubricating Oils," PhD dissertation, Technische Hogeschool Delft, The Netherlands.

[32] Rajagopal, K.R., Szeri, A.Z. 2003,"On An Inconsistency in the Derivation of The Equations of Elastohydrodynamic Lubrication," *Proc.R. Soc. Lond.,* **A459**:.2771-

2786.

[33]   Harris, T.A., *Rolling Bearing Analysis*, fourth ed., 2001, John Wiley and Sons, New York.

[34]   Jorgensen, B.R., Shin, Y.C. 1997, "Dynamics of Machine Tool Spindle/Bearing Systems under Thermal Growth," Journal of Tribol., **119**: 875–882.

[35]   Stein, J.L., Tu, J.F. 1994, "A State-space Model for Monitoring Thermally Induced Preload in Anti-friction Spindle Bearings of High Speed Machine Tools," Journal of Dynamic Systems, Measurement, and Control, **116**: 372–386.

[36]   Nelson, H. D., and McVaugh, J. M. 1976, "The Dynamics of Rotor Bearing Systems Using Finite Elements," ASME J. Eng. Ind., **98**: 593–600.

[37]   Palmgren, A., *Ball and Roller Bearing Engineering*, 3rd edition, 1959, SKF Industries, Philadelphia.

[38]   Lazovic, T., Ristivojevic, M., Mitrovic, R. 2008, "Mathematical Model of Load Distribution in Rolling Bearing," FME Transactions, **36**: 189-196.

[39]   Wirsching, P. H., Paez, T. L., and Ortiz, K., *Random Vibrations:Theory and Practice*, 2006, Dover Publications, New York.

[40]   Raje, N. and Sadeghi, F. 2009, "Statistical Numerical Modeling of Sub-surface Initiated Spalling in the Bearing Contacts," in Proc. IMechE, Part J: J.Engineering Tribol., **223**: 849-858.

[41]   Kärkkäinen, A. Y. J., Sopanen, J.T., and Mikkola A. N. 2006, "Simulation of AMB Supported Rotor during Drop on Retainer Bearings," Research Report No.**63.**, Lappeenranta University of technology, Finland.

[42]   Majumdar P., *Computational Methods for Heat and Mass Transfer*, 2005, Taylor and Francis, New York

[43]   Allaire, P.E., Parsell, J.K., and Barrett, L.E. 1981, "A Pad Perturbation Method for the Dynamic Coefficients of Tilting Pad Journal Bearings," Wear, 29~44.

[44]   Pinkus O., *Thermal Aspects of Fluid Film Tribology*, 1990, ASME PRESS, New York

[45]   Gadangi, R.K. 1995, "Transient Rotordynamics with Flexible Shaft and Flexible Nonlinear Hydrodynamic Journal Bearings Including Thermal Effect," Ph. D. Disseration, Texas A&M University, College Station, Texas

[46]   Fillon.M., Bligoud, J.C.,Frene, J. 1991, "Experimental Study of Tilting Pad Journal Bearings Comparison with Theoretical Thermoelastohydrodynamic Results," ASME Paper **91-Trib-17**: 1~9.

 [47]   Cook, R.D., Malkus, D.S., and Plesha, M.E., *Concepts and Applications of Finite Element Analysis*, 3rd edition, 1989, John Wiley and Sons, New York.

[48]   de Jongh, F. M., and van der Hoeven, P. 1998, "Application of a Heat Barrier Sleeve to Prevent Synchronous Rotor Instability," in Proceedings of the 27th Turbomachinery Symposium, Turbomachinery Laboratory, Texas A&M University, College Station, Texas.

[49]   Timoshenko, S. and Goodier, J. N., *Theory of Elasticity*, 1951, McGraw-Hill.

[50]   Hou. K., Zhu D., and Wen. S. 1985, "A New Numerical Technique for Computing Surface Elastic Deformation Caused by a Given Normal Pressure Distribution," Transactions of the ASME, **107**: 128-131.

APPENDIX A

RAINFLOW CYCLE COUNTING METHOD
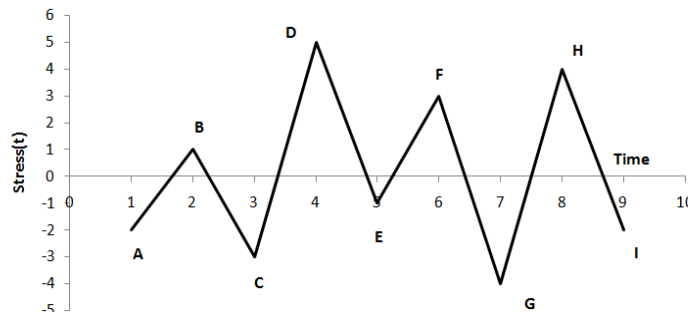
Fig. A.1 Stress vs Time

The rainflow cycle counting is explained according to the ASTM E-1049 Standard Practices for Cycle Counting in Fatigue Analysis. Rules for the rainflow counting method are given as follows;

Let X denotes range under consideration; Y, previous range adjacent to X; and S, starting point in the stress history

a. Read next peak or trough. If out of data, go to step f.

b. If there are less than three points, go to step a. Form ranges X and Y using the three most recent peaks and trough that have not been discarded.

c. Compare the absolute values of ranges X and Y

  i.   If X<Y, go to step a.

  ii. If X>Y, go to step d.

d. If range Y contains the starting point S, go to step e; otherwise, count range Y as one cycle; discard the peak and trough of Y and go to step b.

e. Count range Y as one-half cycle; discard the first point in range Y; move the starting point to the second point in range Y and go to b.

f. Count each range that has not been previously counted as one-half cycle.

The number of cycles corresponding to stress range illustrated in Figure A.1 is summarized in Table A.1.

Table A.1 Stress Cycle Count

Stress range	Cycle counts	Events
10	0	
9	0.5	D-G
8	1	C-D, G-H
7	0	
6	0.5	H-I
5	0	
4	1.5	B-C, E-F
3	0.5	A-B
2	0	
1	0	

APPENDIX B

FINITE ELEMENT FORMULATION OF REYNOLDS EQUATION

This appendix deals with the derivation of finite element equations for the variable viscosity Reynolds equation. The governing equation and the boundary conditions are

$$\nabla \bullet (C_1 \nabla p) + (\nabla C_2) \cdot (U_1 - U_2) + (\nabla h) \cdot U_1 + \frac{dh}{dt} = 0 \tag{B.1}$$

Subject to the boundary conditions;

$$\begin{aligned} P &= P^* &\quad on\ \Gamma_p \\ P &= q^* &\quad on\ \Gamma_q \end{aligned} \tag{B.2}$$
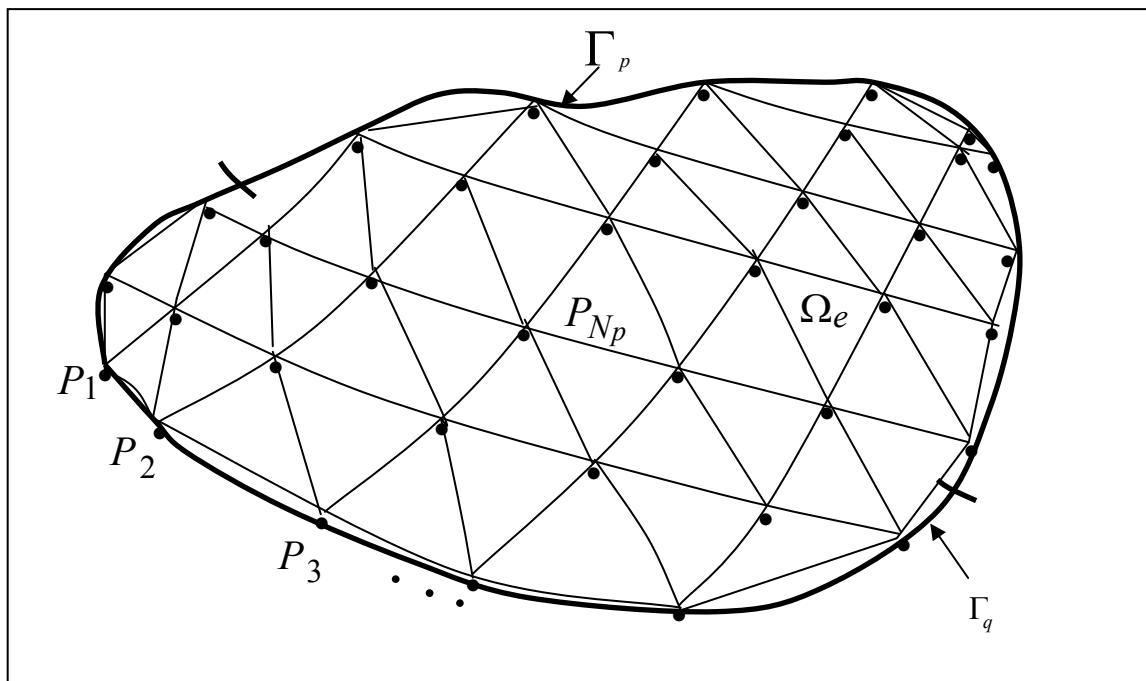
Fig. B.1 FEM Mesh Covering Lubricant Domain Ω

The problem domain with boundaries marked is shown in Fig. B.1. The boundary comprises of two regions, on the first region Γ_p pressure is prescribed, and on the second region Γ_q, flow rate is prescribed. The regions are such that they do not overlap $\Gamma_p \cap \Gamma_q = \varnothing$ and $\Gamma_p \cup \Gamma_q = \Gamma$. The functional for variable viscosity Reynolds equation with the boundary conditions mentioned above is obtained using variational principles and is given by (Huebner, 1981)

$$J_p = \int_\Omega \left[-\frac{1}{2} C_1 \nabla P \cdot \nabla P + C_2 U \cdot \nabla P + P \frac{\partial h}{\partial t} \right] d\Omega + \int_{\Gamma_q} Pq \cdot n d\Gamma \qquad \text{(B.3)}$$

The problem is to find a function P which minimizes the functional shown above. By utilizing the maxima and minima principles, the first derivative of the functional with respect to the function itself should vanish at the minimum. This is shown as;

$$\frac{\partial J_p}{\partial P} = 0 \qquad \text{(B.4)}$$

The finite element method used while discretizing the problem domain, is the Galerkin method. The approximated function P_{ap} is expressed in terms of vectors of shape functions and nodal values of approximated function as shown below;

$$P_{ap} = N \cdot P \qquad \text{(B.5)}$$

In the above equation, vector N is the shape function vector and the vector P is the nodal pressure vector. The final global finite element matrices can then be expressed in the following way;

$$[K_f]\{P\} = \{F_f\} \qquad \text{(B.6)}$$

where

$$[K_f] = -\int_\Omega C_1 \left(\frac{\partial N_i}{\partial x}\frac{\partial N_j}{\partial x} + \frac{\partial N_i}{\partial y}\frac{\partial N_j}{\partial y} \right) d\Omega$$

$$\{B\} = \int_\Omega C_2 U_x \frac{\partial N_i}{\partial x} d\Omega + \int_\Omega C_2 U_y \frac{\partial N_i}{\partial y} d\Omega \tag{B.7}$$

$$\{S\} = -\frac{\partial h}{\partial t}\int_\Omega N_i d\Omega$$

$$\{L\} = -\int_{\Gamma_q} q N_i d\Gamma$$

The above equations are in the final global form. The problem domain needs to be discretized into finite element as shown in Fig. B.1. Discretization of the domain implies the domain Ω is now represented by $\sum \Omega_e(i)$, where i=1, n_{el} and Ω_e is the domain of discretized finite element, and n_{el} is the total number of finite elements. The global matrix $[K_f]$ and the force vector $\{F_f\}$ are given by;

$$[K_f] = \sum_{i=1}^{n_{el}} [K_f^e]$$

$$\{F_f\} = \sum_{i=1}^{n_{el}} \{F_f^e\} \tag{B.8}$$

In the above equations, superscript e implies that these matrices and vectors have been evaluated on the elemental domain. In the chapter 3, the simplex triangular element consists of linear shape functions shown in Fig B.2 are used, while the nine node isoparametric element is used in the chapter 4.
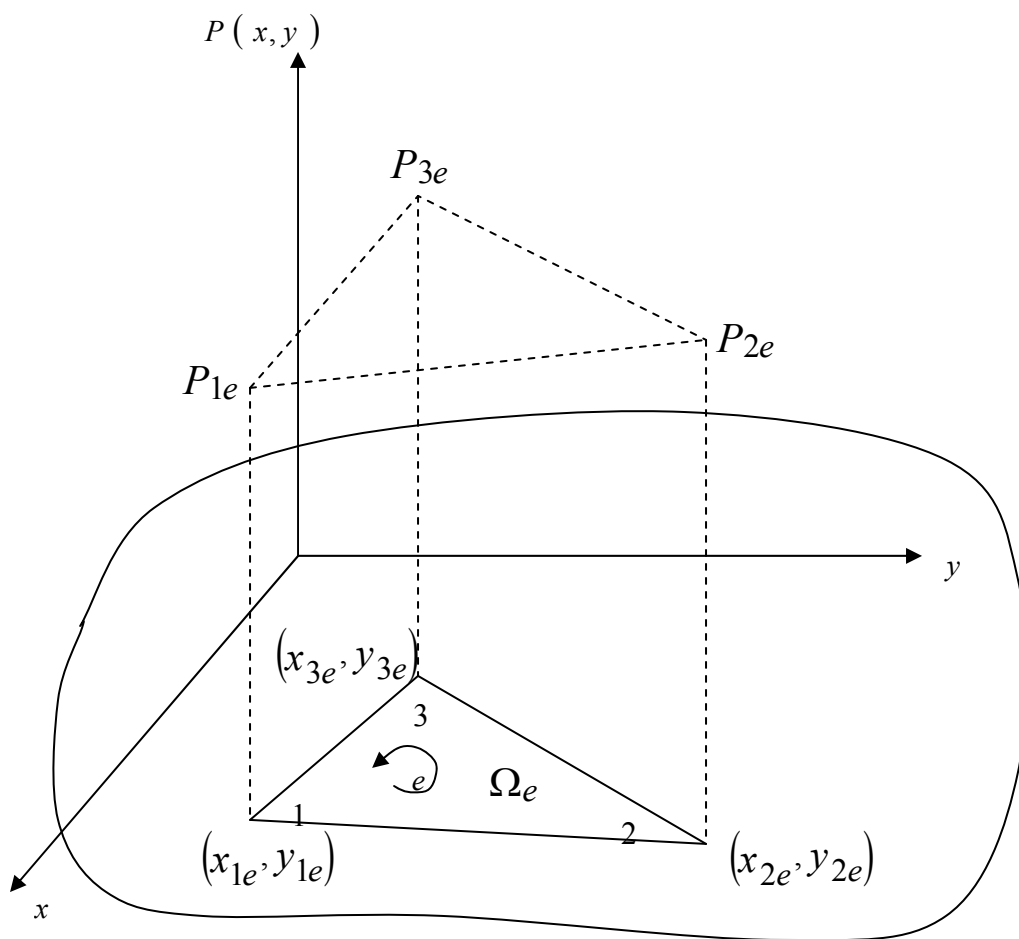
Fig. B.2 Linear Interpolation of Pressure in a 3 Node Simplex Element

i) The discretization of the Reynolds equation using the simplex triangular elements

The shape functions for a simplex triangular element are given by (Segerlind, 1976)

$$N_i = \left(\frac{1}{2A^e}\right)\left(a_i^e + b_i^e + c_i^e\right), \quad i = 1, 2, 3 \tag{B.9}$$

where

$$A^e = \frac{1}{2}\left[(x_2 y_3 - x_3 y_2) - (x_1 y_3 - x_3 y_1) + (x_1 y_2 - x_2 y_1)\right] \tag{B.10}$$

$$
\begin{bmatrix} a_1 & a_2 & a_3 \\ b_1 & b_2 & b_3 \\ c_1 & c_2 & c_3 \end{bmatrix} = \begin{bmatrix} x_2 y_3 - x_3 y_2 & x_3 y_1 - x_1 y_3 & x_1 y_2 - x_2 y_1 \\ y_2 - y_3 & y_3 - y_1 & y_1 - y_2 \\ x_3 - x_2 & x_1 - x_3 & x_2 - x_1 \end{bmatrix} \qquad \text{(B.11)}
$$

The area and line integrals for these shape functions are performed using the following

exact expressions

$$
\int_{A^e} N_1^\alpha N_2^\beta N_3^\gamma \, dA = 2 A^e \, \frac{\alpha! \beta! \gamma!}{(\alpha + \beta + \gamma + 2)!}
$$

$$
\int_{side1-2} N_1^\alpha N_2^\beta \, dL = L_{1-2} \, \frac{\alpha! \beta!}{(\alpha + \beta + 1)!} \qquad \text{(B.12)}
$$

$$
\int_{side1-2} N_3^\gamma \, dL = 0
$$

where $!$ denotes a factorial and L_{1-2} is the length of the element side from nodes 1 to 2.

Substituting the shape functions into Eq (B.7), applying the exact integration equations

given above, the final elemental matrices and vectors are given by

$$
[K_f] = -\int_\Omega C_1 \left(\frac{\partial N_i}{\partial x} \frac{\partial N_j}{\partial x} + \frac{\partial N_i}{\partial y} \frac{\partial N_j}{\partial y} \right) d\Omega = -(b_i b_j + c_i c_j) \frac{\overline{C_1}}{4 A^e}
$$

$$
\{B\} = \int_\Omega C_2 U_x \frac{\partial N_i}{\partial x} d\Omega + \int_\Omega C_2 U_y \frac{\partial N_i}{\partial y} d\Omega = (U_x b_i + U_y c_i) \frac{\overline{C_2}}{2}
$$

$$
\{S\} = -\frac{\partial h}{\partial t} \int_\Omega N_i d\Omega = -\frac{\rho A^e}{3} \frac{\partial h}{\partial t} \qquad \text{(B.13)}
$$

$$
\{L\} = -\int_{\Gamma_q} q N_i d\Gamma = -q \frac{L_{i-j}}{2}
$$

$$
\overline{C_i} = \frac{1}{A^e} \int_{\Omega_e} C_i d\Omega_e
$$

The coefficients defined in Eq.(B.13) are integrated over the elements and divided by

their areas, to get an average.

ii) The discretization of the Reynolds equation using the nine none isoparametric elements

The field pressure at a point inside an element is also interpolated by using the same geometry interpolation function ϕ_j

$$P^{(e)} = \sum_{j=1}^{9} \phi_j P_j^{(e)} \tag{B.14}$$

where $P_j^{(e)}$ is the nodal pressure at (X_j, Y_j) of the element. Furthermore, the Galerkin weighting approach is implemented. That is, the nodal weight functions w_j are chosen exactly as the geometry shape function ϕ_j. Hence

$$w = \{\phi\}^T \tag{B.15}$$

Evaluation of Eq. at each node of every element with its corresponding weight function results in nine independent equations for each element.

$$[K_f] = -\int_\Omega C_1 \left(\frac{\partial N_i}{\partial x} \frac{\partial N_j}{\partial x} + \frac{\partial N_i}{\partial y} \frac{\partial N_j}{\partial y} \right) d\Omega = \int_\Omega \left(\varepsilon \frac{\partial \phi_i}{\partial x} \frac{\partial \phi_j}{\partial x} + \frac{\varepsilon}{\kappa^2} \frac{\partial \phi_i}{\partial y} \frac{\partial \phi_j}{\partial y} \right) d\Omega \tag{B.16}$$

$$\{f\} = \int_\Omega C_2 U_x \frac{\partial N_i}{\partial x} d\Omega + \int_\Omega C_2 U_y \frac{\partial N_i}{\partial y} d\Omega = \int_\Omega H \frac{\partial \phi_i}{\partial X} d\Omega + \int_\Gamma q \cdot n d\Gamma \tag{B.17}$$

where ε and κ are defined in the chapter 4.

The shape functions used in the chapter 4 are given by:

$$\phi_1 = \frac{1}{4}(\hat{x}^2 - \hat{x})(\hat{y}^2 - \hat{y})$$

$$\phi_2 = \frac{1}{2}(1 - \hat{x}^2)(\hat{y}^2 - \hat{y})$$

$$\phi_3 = \frac{1}{2}(\hat{x}^2 + \hat{x})(\hat{y}^2 - \hat{y})$$

$$\phi_4 = \frac{1}{2}(\hat{x}^2 - \hat{x})(1 - \hat{y}^2)$$

$$\phi_5 = (1 - \hat{x}^2)(1 - \hat{y}^2)$$

$$\phi_6 = \frac{1}{2}(\hat{x}^2 + \hat{x})(1 - \hat{y}^2)$$

$$\phi_7 = \frac{1}{4}(\hat{x}^2 - \hat{x})(\hat{y}^2 + \hat{y})$$

$$\phi_8 = \frac{1}{2}(1 - \hat{x}^2)(\hat{y}^2 + \hat{y})$$

$$\phi_9 = \frac{1}{4}(\hat{x}^2 + \hat{x})(\hat{y}^2 + \hat{y}) \tag{B.18}$$

The coordinate transformations from the physical coordinate to the natural coordinate

are considered. Since $X = \sum_{i=1}^{9} \phi_i(\hat{x}, \hat{y}) X_i$ and $Y = \sum_{i=1}^{9} \phi_i(\hat{x}, \hat{y}) Y_i$, the mapping from global

to local coordinates is expressed as

$$\frac{\partial \phi_i}{\partial \hat{x}} = \frac{\partial \phi_i}{\partial X} \frac{\partial X}{\partial \hat{x}} + \frac{\partial \phi_i}{\partial Y} \frac{\partial Y}{\partial \hat{x}} \tag{B.19}$$

$$\frac{\partial \phi_i}{\partial \hat{y}} = \frac{\partial \phi_i}{\partial X} \frac{\partial X}{\partial \hat{y}} + \frac{\partial \phi_i}{\partial Y} \frac{\partial Y}{\partial \hat{y}} \tag{B.20}$$

That is

$$\left\{ \begin{array}{c} \dfrac{\partial \phi_i}{\partial \hat{x}} \\ \dfrac{\partial \phi_i}{\partial \hat{y}} \end{array} \right\} = \left[\begin{array}{cc} \dfrac{\partial X}{\partial \hat{x}} & \dfrac{\partial Y}{\partial \hat{x}} \\ \dfrac{\partial X}{\partial \hat{y}} & \dfrac{\partial Y}{\partial \hat{y}} \end{array} \right] \left\{ \begin{array}{c} \dfrac{\partial \phi_i}{\partial X} \\ \dfrac{\partial \phi_i}{\partial Y} \end{array} \right\} = [J] \left\{ \begin{array}{c} \dfrac{\partial \phi_i}{\partial X} \\ \dfrac{\partial \phi_i}{\partial Y} \end{array} \right\} \tag{B.21}$$

where $[J]$ is the Jacobian matrix.

Thus

$$\begin{Bmatrix} \dfrac{\partial \phi_i}{\partial X} \\[2mm] \dfrac{\partial \phi_i}{\partial Y} \end{Bmatrix} = [J]^{-1} \begin{Bmatrix} \dfrac{\partial \phi_i}{\partial \hat{x}} \\[2mm] \dfrac{\partial \phi_i}{\partial \hat{y}} \end{Bmatrix} \tag{B.22}$$

Also

$$dXdY = \det[J]d\hat{x}d\hat{y} \tag{B.23}$$

For the numerical integration scheme, some variables are defined by

$$H(x,y) = \sum_{i=1}^{9} \phi_i(x,y) H_i \tag{B.23}$$

$$\eta(x,y) = \sum_{i=1}^{9} \phi_i(x,y) \eta_i \tag{B.24}$$

Then

$$\varepsilon = \lambda \frac{H^3}{\eta} = \lambda \frac{\left(\displaystyle\sum_{i=1}^{9} \phi_i H_i^{(e)}\right)^3}{\displaystyle\sum_{i=1}^{9} \phi_i \eta_i^{(e)}} \tag{B.25}$$

where $\lambda = \dfrac{b^3 P_{max}}{12 E' R_x^3 u}$

For a function $g(\hat{x}, \hat{y})$, the numerical integration reads

$$\int_{-1}^{1}\int_{-1}^{1} g(\hat{x},\hat{y})d\hat{x}d\hat{y} \approx \int_{-1}^{1}\left[\sum_{J=1}^{N_G} g(\hat{x},\hat{y}_J)w_J\right]d\hat{x} = \sum_{I=1}^{M_G}\sum_{J=1}^{N_G} g(\hat{x}_I,\hat{y}_J)w_J w_I \tag{B.26}$$

where M_G and N_G are the number of quadrature points in $\hat{x}$ and $\hat{y}$ directions, $(\hat{x}_I, \hat{y}_J)$

are Gauss points, w_I and w_J are corresponding Gauss weights listed in Table B.1. The global fluidity matrix and the force vectors are assembled according to the nodal connectivity of the finite element mesh. The system of global equations gives a symmetric banded matrix. This symmetric banded matrix can be reduced and solved with a symmetric banded solver to increase efficiency. The solution of these global system of linear equations gives a solution vector contacting the nodal pressures.

Table B.1 Gauss Quadrature Points and Weight Factors

Gauss point $(\widehat{x}_I, \widehat{y}_J)$	Gauss Weights w_I	Gauss Weights w_J
$\left(-(3/5)^{1/2} \quad -(3/5)^{1/2}\right)$	0.555555555	0.555555555
$\left(0 \quad -(3/5)^{1/2}\right)$	0.888888889	0.555555555
$\left((3/5)^{1/2} \quad -(3/5)^{1/2}\right)$	0.555555555	0.555555555
$\left(-(3/5)^{1/2} \quad 0\right)$	0.555555555	0.888888889
$\left(0 \quad 0\right)$	0.888888889	0.888888889
$\left((3/5)^{1/2} \quad 0\right)$	0.555555555	0.888888889
$\left(-(3/5)^{1/2} \quad (3/5)^{1/2}\right)$	0.555555555	0.555555555
$\left(0 \quad (3/5)^{1/2}\right)$	0.888888889	0.555555555
$\left((3/5)^{1/2} \quad (3/5)^{1/2}\right)$	0.555555555	0.555555555

APPENDIX C

FINITE ELEMENT FORMULATION OF ENERGY EQUATION

The solution of Reynolds equation gives pressure distribution throughout the fluid film. This pressure distribution is used in evaluating the velocity profile in the fluid film. The solution of energy equation requires the velocity profile. The problem domain for energy equation with different boundaries is shown in Figure C.1 as seen from the figure, the boundary is comprised of three different regions. The first region is the region over which temperature is prescribed Γ_T, the second region is the part of the boundary over which heat flux is prescribed Γ_f, and the third region is the one over which convection is prescribed Γ_h.
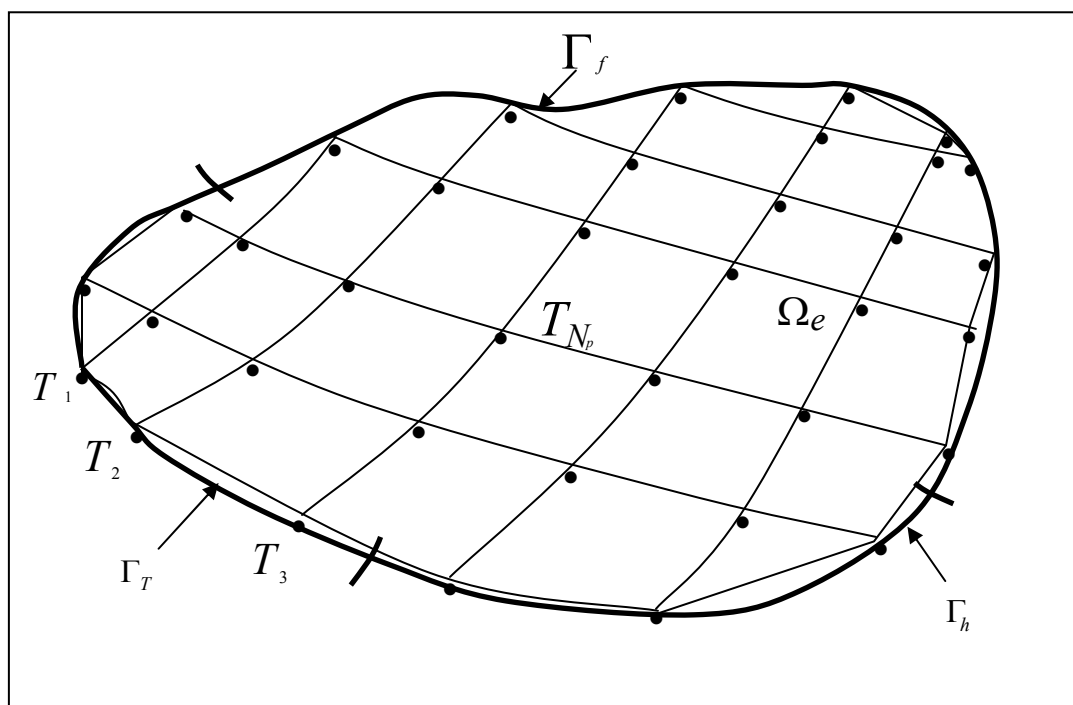

Fig. C.1 FEM Mesh Covering Lubricant Domain Ω

The governing equation is given by;

$$\rho c_p \left(\frac{\partial T}{\partial t} + u \bullet \nabla T \right) = k \nabla \bullet \nabla T + \Phi \qquad \text{(C.1)}$$

Subject to the following boundary conditions;

$$
\begin{aligned}
T &= T^* & \text{on } \Gamma_T \\
q &= q^* & \text{on } \Gamma_f \\
q &= -h(T - T_\infty) & \text{on } \Gamma_T
\end{aligned}
\qquad \text{(C.2)}
$$

Galerkin method is used to find the weighted residual equation for the solution of energy equation. On applying, the weighted residual to the governing equation gives

$$\int_\Omega \left(\rho c_p \left(\frac{\partial T}{\partial t} + u \bullet \nabla T \right) - Q - k \nabla \bullet \nabla T \right) W d\Omega = 0 \qquad \text{(C.3)}$$

Where W is the weight function. Applying Gauss theorem and applying the boundary condition, Eq (C.1) becomes;

$$
\begin{aligned}
&\int_\Omega \rho c_p \frac{\partial T}{\partial t} W d\Omega + \int_\Omega \rho c_p u \bullet \nabla T W d\Omega - \int_\Omega Q W d\Omega + \int_\Omega k \nabla T \bullet \nabla W d\Omega \\
&- \int_{\Gamma_T} \left(kTW \right) \bullet n d\Gamma + \int_{\Gamma_f} \left(q^* W \right) \bullet n d\Gamma - \int_{\Gamma_h} hT_\infty W d\Gamma + \int_{\Gamma_h} hTW d\Gamma = 0
\end{aligned}
\qquad \text{(C.4)}
$$

The solution to the Eq (C.4) is interpolated over an element using the shape functions as follows

$$T = \bar{N} \bullet \bar{T} \qquad \text{(C.5)}$$

In the above equation the vector $\bar{N}$ contains the shape functions and the vector $\bar{T}$ contains the nodal values of temperatures on that particular element. Substituting the interpolated temperature into Eq (C.4), and factoring out T;

$$\left[\int_\Omega \rho c_p W N_j d\Omega\right]\{\dot{T}_j\} + \left[\int_\Omega \left(\rho c_p W u \cdot \nabla N_j + k\nabla W \cdot \nabla N_j\right)d\Omega + \int_{\Gamma_h} hWN_j d\Gamma\right]\{T_j\}$$
$$= \int_\Omega QWd\Omega + \int_{\Gamma_f}\left(qW\right)d\Gamma + \int_{\Gamma_T}(k\nabla T)\cdot nWd\Gamma + \int_{\Gamma_h} hT_\infty Wd\Gamma \tag{C.6}$$

The weight functions are selected such that their values on the boundary Γ_T vanish. Hence, from the above equation, the following integration on the temperature prescribed boundary vanishes;

$$\int_{\Gamma_T}(k\nabla T)\cdot nWd\Gamma = 0 \tag{C.7}$$

The system of equations can be represented as matrices and vectors in the following way;

$$[K_m] = \int_\Omega \rho c_p W_i N_j d\Omega$$
$$[K_v] = \int_\Omega \rho c_p W_i u \cdot \nabla N_j d\Omega$$
$$[K_c] = \int_\Omega k\nabla W_i \cdot \nabla N_j d\Omega$$
$$[K_h] = \int_{\Gamma_h} hW_i N_j d\Gamma d\Omega \tag{C.8}$$
$$\{F_Q\} = \int_\Omega QW_i d\Omega$$
$$\{F_h\} = \int_{\Gamma_h} hT_\infty W_i d\Gamma$$
$$\{F_f\} = \int_{\Gamma_f}\left(qW_i\right)d\Gamma$$

Discretization of the problem is done with 4 node isoparametric elements and quadratic Petrov-Galerkin technique for steady state problems and cubic Petrov-Galerkin technique for transient problems. On elemental basis each of the vectors and matrix are expressed as;

$$[K_m^e] = \int_{\Omega^e} \rho c_p W_i^e N_j^e d\Omega^e$$

$$[K_v^e] = \int_{\Omega^e} \rho c_p W_i^e u \cdot \nabla N_j^e d\Omega^e$$

$$[K_c^e] = \int_{\Omega} k \nabla W_i^e \cdot \nabla N_j^e d\Omega^e$$

$$[K_h^e] = \int_{\Gamma_h} h W_i^e N_j^e d\Gamma d\Omega^e \qquad (C.9)$$

$$\{F_Q^e\} = \int_{\Omega^e} Q W_i^e d\Omega^e$$

$$\{F_h^e\} = \int_{\Gamma_h^e} h T_\infty W_i^e d\Gamma^e$$

$$\{F_f^e\} = \int_{\Gamma_f^e} \left(q W_i^e \right) d\Gamma^e$$

Classical Galerkin sometimes called the Bubanov-Galerkin method employs the shape functions as the weight functions. But, it has been shown that when the magnitudes of the first order derivative terms increases, the solutions give numerical problems. To counter this problem, the weight functions have to be modified as explained in Chpater 4. If over an element, the nodal values and the nodal coordinates are interpolated using the same shape functions, it is called an isoparametric element. To perform integration on the isoparametric elements, the physical coordinate have to be mapped onto the natural coordinates. The shape functions of the isoparametric element are

$$N_1 = \frac{1}{4}(1-\eta)(1-\zeta)$$

$$N_2 = \frac{1}{4}(1+\eta)(1-\zeta)$$

$$N_3 = \frac{1}{4}(1+\eta)(1+\zeta) \qquad (C.10)$$

$$N_4 = \frac{1}{4}(1+\eta)(1-\zeta)$$

After the mapping, integration is performed on the natural coordinate domain using Gauss-Quadrature numerical integration method explained in Appendix B. The Gauss quadrature points and the corresponding weight factors is shown in Table C.1. The Gauss quadrature then can be applied on an elemental basis, and the elemental values of the matrices and vectors can be represented as;

$$[K_m^e] = \sum_{l=1}^{2} \sum_{k=1}^{2} \rho c_p W_i^e N_j^e J w_k w_l$$

$$[K_v^e] = \sum_{l=1}^{2} \sum_{k=1}^{2} \rho c_p W_i^e u \cdot \nabla N_j^e J w_k w_l$$

$$[K_c^e] = \sum_{l=1}^{2} \sum_{k=1}^{2} k \nabla W_i^e \cdot \nabla N_j^e J w_k w_l$$

$$[K_h^e] = \sum_{l=1}^{2} \sum_{k=1}^{2} h W_i^e N_j^e J w_k w_l \qquad \text{(C.11)}$$

$$\{F_Q^e\} = \sum_{l=1}^{2} \sum_{k=1}^{2} Q W_i^e J w_k w_l$$

$$\{F_h^e\} = \sum_{l=1}^{2} \sum_{k=1}^{2} h T_\infty W_i^e J w_k w_l$$

$$\{F_f^e\} = \sum_{l=1}^{2} \sum_{k=1}^{2} q W_i^e J w_k w_l$$

where J is the Jacobian matrix.

The shape functions and weight functions are evaluated at each Gauss point. These element matrices and vectors are now assembled together in a global form following the element and nodal connectivity. The global form of the set of equations is

$$[K_m]\{\dot{T}\} + [K_T]\{T\} = \{F_T\} \qquad \text{(C.12)}$$

Where

$$[K_m] = \sum_{e=1}^{n_{el}} [K_m^e] \qquad \text{(C.13)}$$

$$[K_T] = \sum_{e=1}^{n_{el}} \left\{ [K_v^e] + [K_c^e] + [K_h^e] \right\} \qquad (C.14)$$

$$[F_T] = \sum_{e=1}^{n_{el}} \left\{ \{F_Q^e\} + \{F_h^e\} + \{F_f^e\} \right\} \qquad (C.15)$$

The mass or distribution matrix $[K_m]$ is symmetric and banded but it should be noted that matrix $[K_T]$ is an asymmetric banded matrix.

Table C.1 Gauss Quadrature Points and Weight Factors

Gauss point $(\hat{x}_I, \hat{y}_J)$	Gauss Weights w_I	Gauss Weights w_J
$(-0.57735 \quad -0.57735)$	1.00000	1.00000
$(0.57735 \quad -0.57735)$	1.00000	1.00000
$(-0.57735 \quad 0.57735)$	1.00000	1.00000
$(0.57735 \quad 0.57735)$	1.00000	1.00000

APPENDIX D

DEFORMATION KERNEL

Substitution of $\phi_j = b_1^j(\bar{X}^2 + b_2^j\bar{X} + b_3^j)(\bar{Y}^2 + b_4^j\bar{Y} + b_5^j)$ into Eq. (4.47) gives

$$d_j^{(e)} = \int_{\bar{Y}_1}^{\bar{Y}_3}\int_{\bar{X}_1}^{\bar{X}_3} \frac{b_1^j(\bar{X}^2 + b_2^j\bar{X} + b_3^j)(\bar{Y}^2 + b_4^j\bar{Y} + b_5^j)}{\left[\bar{X}^2 + \bar{Y}_1^2\right]^{1/2}}d\bar{X}d\bar{Y}$$

$$= b_1^j\int_{\bar{Y}_1}^{\bar{Y}_3}\int_{\bar{X}_1}^{\bar{X}_3} \frac{\bar{X}^2(\bar{Y}^2 + b_4^j\bar{Y} + b_5^j)}{\left[\bar{X}^2 + \bar{Y}_1^2\right]^{1/2}}d\bar{X}d\bar{Y}$$

$$+ b_1^j b_2^j\int_{\bar{Y}_1}^{\bar{Y}_3}\int_{\bar{X}_1}^{\bar{X}_3} \frac{\bar{X}(\bar{Y}^2 + b_4^j\bar{Y} + b_5^j)}{\left[\bar{X}^2 + \bar{Y}_1^2\right]^{1/2}}d\bar{X}d\bar{Y}$$

$$+ b_1^j b_3^j\int_{\bar{Y}_1}^{\bar{Y}_3}\int_{\bar{X}_1}^{\bar{X}_3} \frac{(\bar{Y}^2 + b_4^j\bar{Y} + b_5^j)}{\left[\bar{X}^2 + \bar{Y}_1^2\right]^{1/2}}d\bar{X}d\bar{Y}$$

$$= b_1^j(d_1 + b_2^j d_2 + b_3^j d_3)$$

From Calculus,

$$\int \frac{q^2}{\sqrt{a^2 + q^2}}dq = \frac{q}{2}\sqrt{a^2 + q^2} - \frac{a^2}{2}\ln\left(q + \sqrt{a^2 + q^2}\right)$$

$$\int \frac{q}{\sqrt{a^2 + q^2}}dq = \sqrt{a^2 + q^2}$$

$$\int \frac{1}{\sqrt{a^2 + q^2}}dq = \ln\left(q + \sqrt{a^2 + q^2}\right)$$

d_i becomes

$$d_1 = \frac{\overline{X}}{2}\left(\int_{\overline{Y}_1}^{\overline{Y}_3} \overline{Y}^2 t d\overline{Y} + b_4^j \int_{\overline{Y}_1}^{\overline{Y}_3} \overline{Y} t d\overline{Y} + b_5^j \int_{\overline{Y}_1}^{\overline{Y}_3} t d\overline{Y} \right)$$

$$- \frac{1}{2}\left(\int_{\overline{Y}_1}^{\overline{Y}_3} \overline{Y}^4 \ln\left(\overline{X}+t\right) d\overline{Y} + b_4^j \int_{\overline{Y}_1}^{\overline{Y}_3} \overline{Y}^3 \ln\left(\overline{X}+t\right) d\overline{Y} + b_5^j \int_{\overline{Y}_1}^{\overline{Y}_3} \ln\left(\overline{X}+t\right) d\overline{Y} \right)$$

$$d_2 = \int_{\overline{Y}_1}^{\overline{Y}_3} \overline{Y}^2 t d\overline{Y} + b_4^j \int_{\overline{Y}_1}^{\overline{Y}_3} \overline{Y} t d\overline{Y} + b_5^j \int_{\overline{Y}_1}^{\overline{Y}_3} t d\overline{Y}$$

$$d_3 = \int_{\overline{Y}_1}^{\overline{Y}_3} \overline{Y}^2 \ln\left(\overline{X}+t\right) d\overline{Y} + b_4^j \int_{\overline{Y}_1}^{\overline{Y}_3} \overline{Y} \ln\left(\overline{X}+t\right) d\overline{Y} + b_5^j \int_{\overline{Y}_1}^{\overline{Y}_3} \ln\left(\overline{X}+t\right) d\overline{Y}$$

Since

$$\int t d\overline{Y} = \frac{1}{2}\overline{Y}t + \frac{1}{2}\overline{X}^2 \ln(\overline{Y}+t)$$

$$\int \overline{Y} t d\overline{Y} = \frac{1}{3}t^3$$

$$\int \overline{Y}^2 t d\overline{Y} = \frac{1}{4}\overline{Y}t^3 - \frac{1}{8}\overline{X}^2\overline{Y}t - \frac{1}{8}\overline{X}^4 \ln(\overline{Y}+t)$$

$$\int \ln(\overline{X}+t) d\overline{Y} = \overline{X}\ln(\overline{Y}+t) + \overline{Y}\ln(\overline{X}+t) - \overline{Y}$$

$$\int \overline{Y}\ln(\overline{X}+t) d\overline{Y} = \frac{1}{2}\left(\overline{X}+t\right)^2 \ln\left(\overline{X}+t\right) + \frac{\overline{X}^2}{2} + \frac{\overline{X}t}{2} - \frac{\overline{Y}^2}{4} - \overline{X}^2 \ln\left(\overline{X}+t\right) - \overline{X}t\ln\left(\overline{X}+t\right)$$

$$\int \overline{Y}^2 \ln(\overline{X}+t) d\overline{Y} = \frac{\overline{Y}^3}{3}\ln\left(\overline{X}+t\right) + \frac{1}{6}\overline{X}\overline{Y}t - \frac{1}{6}\overline{X}^3 \ln\left(\overline{Y}+t\right) - \frac{1}{9}\overline{Y}^3$$

$$\int \overline{Y}^3 \ln(\overline{X}+t) d\overline{Y} = \frac{\overline{Y}^4}{4}\ln\left(\overline{X}+t\right) + \frac{\overline{X}}{4}\left(\frac{1}{3}\overline{Y}^2 - \frac{2}{3}\overline{X}^2\right)t - \frac{1}{16}\overline{Y}^4$$

$$\int \overline{Y}^4 \ln(\overline{X}+t) d\overline{Y} = \frac{\overline{Y}^5}{5}\ln\left(\overline{X}+t\right) + \frac{\overline{X}\overline{Y}^2 t}{20} - \frac{3}{40}\overline{X}^3\overline{Y}t + \frac{3}{40}\overline{X}^5 \ln(\overline{Y}+t) - \frac{1}{25}\overline{Y}^5$$

Thus

$$d_1 = \frac{\bar{X}}{8}\left[\bar{Y}t^3 - \frac{1}{2}\bar{X}^2\bar{Y}t - \frac{1}{2}\bar{X}^4\ln(\bar{Y}+t)\right] + b_4^j\frac{1}{6}\bar{X}t^3 + b_5^j\frac{\bar{X}}{4}\left[\bar{Y}t + \bar{X}^2\ln(\bar{Y}+t)\right]$$

$$-\frac{1}{10}\left[\bar{Y}^5\ln(\bar{X}+t) + \frac{\bar{X}\bar{Y}^2t}{4} - \frac{3}{8}\bar{X}^3\bar{Y}t + \frac{3}{8}\bar{X}^5\ln(\bar{Y}+t) - \frac{1}{5}\bar{Y}^5\right]$$

$$-b_4^j\frac{1}{8}\left[\bar{Y}^4\ln(\bar{X}+t) + \bar{X}\left(\frac{1}{3}\bar{Y}^2 - \frac{2}{3}\bar{X}^2\right)t - \frac{1}{4}\bar{Y}^4\right]$$

$$-b_5^j\frac{1}{6}\left[\bar{Y}^3\ln(\bar{X}+t) + \frac{1}{2}\bar{X}\bar{Y}t - \frac{1}{2}\bar{X}^3\ln(\bar{Y}+t) - \frac{1}{3}\bar{Y}^3\right]$$

$$d_2 = \frac{1}{4}\left[\bar{Y}t^3 - \frac{1}{2}\bar{X}^2\bar{Y}t - \frac{1}{2}\bar{X}^4\ln(\bar{Y}+t)\right] + b_4^j\frac{1}{3}t^3 + b_5^j\left[\bar{Y}t + \bar{X}^2\ln(\bar{Y}+t)\right]$$

$$d_3 = \frac{1}{3}\left[\bar{Y}^3\ln(\bar{X}+t) + \frac{1}{2}\bar{X}\bar{Y}t - \frac{1}{2}\bar{X}^3\ln(\bar{Y}+t) - \frac{1}{3}\bar{Y}^3\right]$$

$$+b_4^j\left[\frac{1}{2}(\bar{X}+t)^2\ln(\bar{X}+t) + \frac{\bar{X}^2}{2} + \frac{\bar{X}t}{2} - \frac{\bar{Y}^2}{4} - \bar{X}^2\ln(\bar{X}+t) - \bar{X}t\ln(\bar{X}+t)\right]$$

$$+b_5^j\left[\bar{X}\ln(\bar{Y}+t) + \bar{Y}\ln(\bar{X}+t) - \bar{Y}\right]$$

Now

$$d_j^{(e)}(u,v) = b_1^j\left[d_1(\bar{X}_3,\bar{Y}_3) + d_1(\bar{X}_1,\bar{Y}_1) - d_1(\bar{X}_1,\bar{Y}_3) - d_1(\bar{X}_3,\bar{Y}_1)\right]$$

$$+b_1^jb_2^j\left[d_2(\bar{X}_3,\bar{Y}_3) + d_2(\bar{X}_1,\bar{Y}_1) - d_2(\bar{X}_1,\bar{Y}_3) - d_2(\bar{X}_3,\bar{Y}_1)\right]$$

$$+b_1^jb_3^j\left[d_3(\bar{X}_3,\bar{Y}_3) + d_3(\bar{X}_1,\bar{Y}_1) - d_3(\bar{X}_1,\bar{Y}_3) - d_3(\bar{X}_3,\bar{Y}_1)\right]$$

Define

$$g_1(\bar{X},\bar{Y}) = d_1 + b_2^j d_2 + b_3^j d_3$$

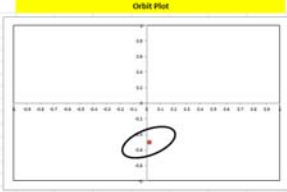After manipulation, $g_1(\bar{X},\bar{Y})$ finally becomes Eq. (4.46).

APPENDIX E

USER INTERFACES

E. 1 The Journal Temperature Calculation

➤ User Interfaces: Input

The following figure shows the input parameters that used in the developed codes.

a. Bearing Geometry

Bearing Geometry	
Length (m)	0.07
Diameter (m)	0.1
Bearing Radial Clearance (m)	5.00E-05
Pad Thickness (m)	0.02
Pad Arc Length (deg)	75
Number of Pads	4
Offset	0.5
Preload	0.68

b. Journal Properties

| Journal Properties	
Mass density (kg/m3)	7850
Specific heat capacity (J/kgK)	453.6
Thermal conductivity (W/mK)	50
Steady state temperature (C)	55

c. Lubricant Properties

Lubricant Properties	
Viscosity (Pa s)	0.0277
Viscosity exponent (1/K)	0.034
Inlet temperature ($^{\circ}C$)	40
Supply Pressure (Mpa)	0.1
Mass density (kg/m3)	860
Specific heat capacity (J/kgK)	2000
Thermal conductivity (W/mK)	0.13

d. Orbit

Orbit			
Static Eccentricity	0.5	Phase (deg)	-88.3564
Amplitude of X direction probe	0.2	Phase (deg)	0
Amplitude of Y direction probe	0.2	Phase (deg)	30
Spin speed (rpm)	4000		
Type (LBP:0, LOP:1)	0	RUN	

Orbit Plot
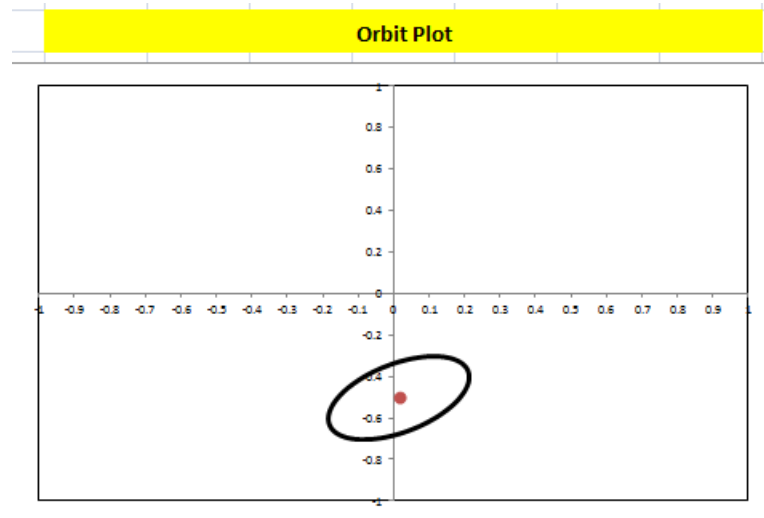
e. Static Eccentricity

< Static Eccentricity Information>			
Journal Position X (m)	8.53E-07	#1 Pad tilt angle(deg)	0.080214091
Journal Position Y (m)	-2.99E-05	#2 Pad tilt angle(deg)	0.034377468
Attitude Angle (deg)	-88.3564	#3 Pad tilt angle(deg)	0.034377468
		#4 Pad tilt angle(deg)	0.080214091
		#5 Pad tilt angle(deg)	NAN
		#6 Pad tilt angle(deg)	NAN

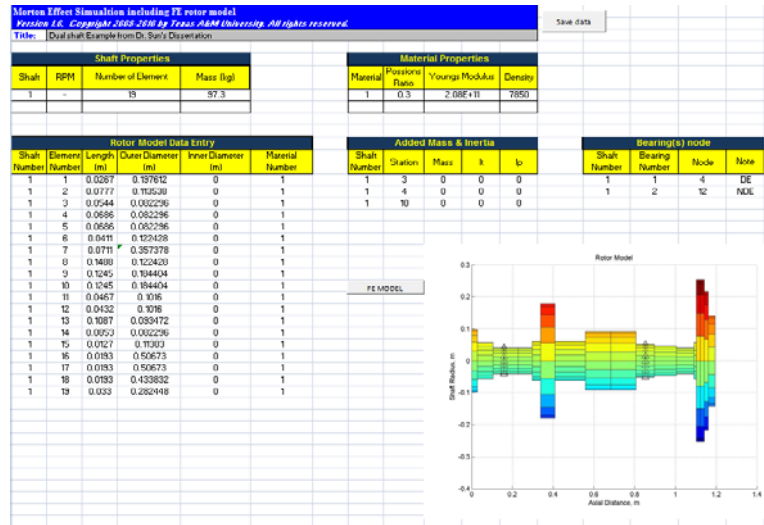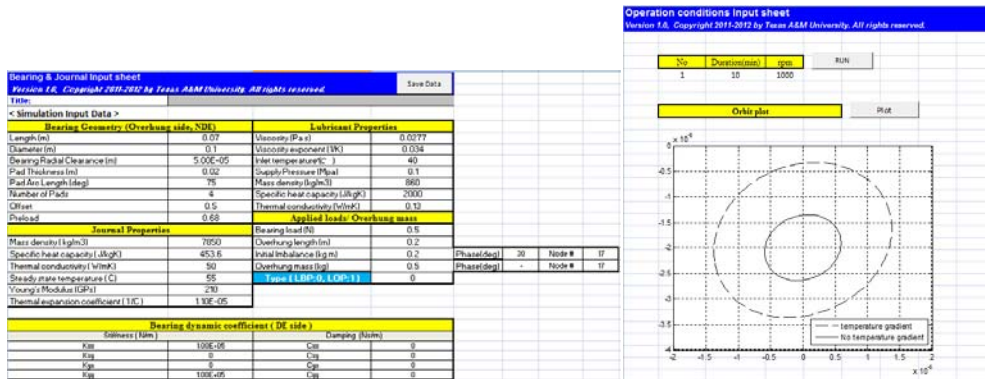➢ User Interfaces: Output
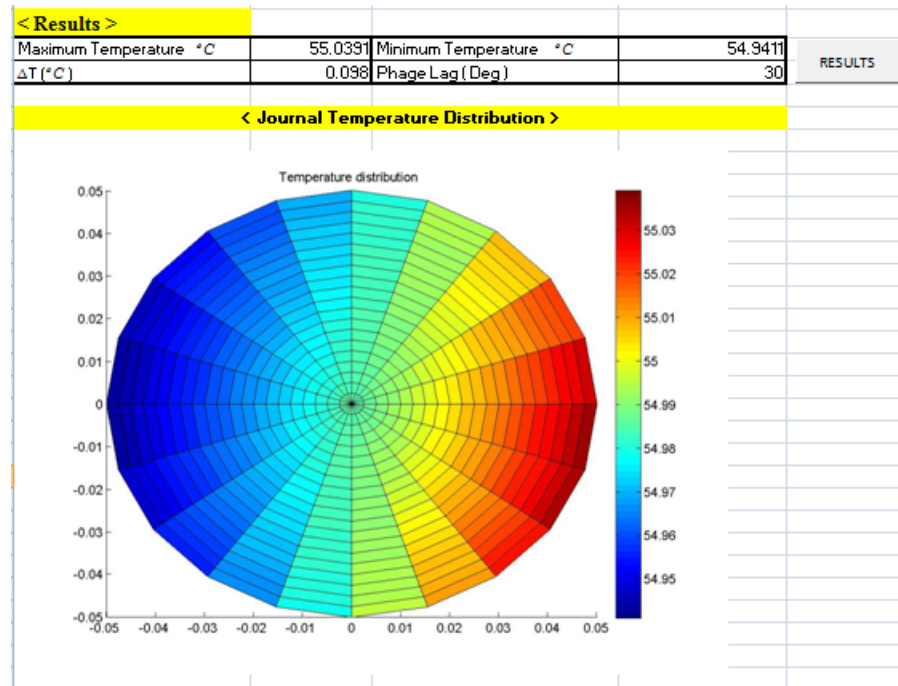
E.2 The Morton Effect

> User Interfaces : Input Parameters

The following figures show the input parameters that used in the codes.

a. FE rotor model

b. Bearing model   c. Operation condition & Results

a. FE rotor model

- Shaft Properties

Shaft Properties			
Shaft	RPM	Number of Element	Mass (kg)
1	-	19	97.3

Material Properties			
Material	Possions Ratio	Youngs Modulus	Density
1	0.3	2.08E+11	7850

- FE rotor data

Rotor Model Data Entry					
Shaft Number	Element Number	Length (m)	Outer Diameter (m)	Inner Diameter (m)	Material Number
1	1	0.0267	0.197612	0	1
1	2	0.0777	0.113538	0	1
1	3	0.0544	0.082296	0	1
1	4	0.0686	0.082296	0	1
1	5	0.0686	0.082296	0	1

Added Mass & Inertia				
Shaft Number	Station	Mass	It	Ip
1	3	0	0	0
1	4	0	0	0
1	10	0	0	0

- Bearing Nodes

Bearing(s) node			
Shaft Number	Bearing Number	Node	Note
1	1	4	DE
1	2	12	NDE

b. Bearing model

- Bearing properties for NDE side

Bearing Geometry (Overhung side, NDE)		Lubricant Properties					
Length (m)	0.07	Viscosity (Pa s)	0.0277				
Diameter (m)	0.1	Viscosity exponent (1/K)	0.034				
Bearing Radial Clearance (m)	5.00E-05	Inlet temperature (C)	40				
Pad Thickness (m)	0.02	Supply Pressure (Mpa)	0.1				
Pad Arc Length (deg)	75	Mass density (kg/m3)	860				
Number of Pads	4	Specific heat capacity (J/kgK)	2000				
Offset	0.5	Thermal conductivity (W/mK)	0.13				
Preload	0.68	Applied loads/ Overhung mass					
Journal Properties		Bearing load (N)	0.5				
Mass density (kg/m3)	7850	Overhung length (m)	0.2				
Specific heat capacity (J/kgK)	453.6	Initial Imbalance (kg m)	0.2	Phase(deg)	30	Node #	17
Thermal conductivity (W/mK)	50	Overhung mass (kg)	0.5	Phase(deg)	-	Node #	17
Steady state temperature (C)	55	Type (LBP:0, LOP:1)	0				
Young's Modulus (GPs)	210						
Thermal expansion coefficient (1/C)	1.10E-05						

- Bearing dynamic properties for DE side

Bearing dynamic coefficient (DE side)			
Stiffness (N/m)		Damping (Ns/m)	
Kxx	1.00E+05	Cxx	0
Kxy	0	Cxy	0
Kyx	0	Cyx	0
Kyy	1.00E+05	Cyy	0

c. Operation condition

No	Duration(min)	rpm
1	10	1000

➢ User Interfaces: Output

The orbit plot is provided as the results of Morton effect simulation as following.
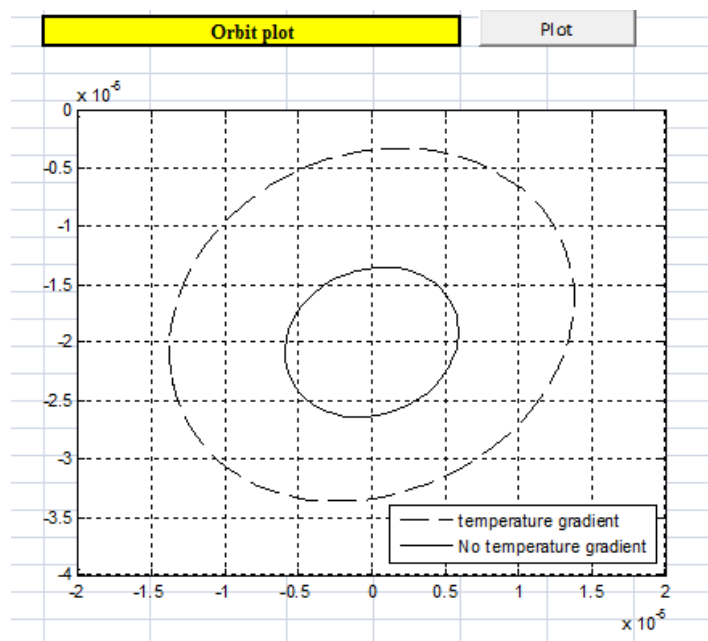
VITA

Jung Gu Lee was born in Keyryong, South Korea. He grew up in Keyryoung until his high school year. He received his Bachelor of Science degree and Master of Science degree in mechanical engineering from Soongsil University in February 2002, 2004, respectively. After obtaining the degrees, he had worked for the OXUS research center, South Korea for 4 years. He attended the Department of Mechanical Engineering at the Texas A&M University in August 2008. Mr. Lee worked with Dr.Palazzolo in the Vibration Control and Electromechanics Lab since January 2009 until successfully completing his qualifying exams and required course work. During most of this period, he focused on Rotordynamics, Tribology problems with specific emphasis on from rolling element bearing to fluid film bearing, which were sponsored by Turbomachinery Research Consortium.

He can be reached at the following address:

Vibration Control and Electromechanics Laboratory

Department of Mechanical Engineering, MS 3123

Texas A&M University

College Station, Texas, 77843-3123